DELTA
Annual Report
2021

Dortmund
30. November 2021

Dear readers, dear colleagues,

this DELTA annual report is now the second that is published without a user's meeting in the time of the COVID-19 pandemic, the impact of which has still substantially influenced the operation of the DELTA machine and the conducted user experiments. Despite all those problems, many successful experiments have been realized, and the storage ring could be kept in operation in 2021, to deliver 17 out of 20 planned weeks of synchrotron radiation and additional machine dedicated experimental time.

The 7 T superconducting wiggler installed in 2020 was regularly operated with a magnetic field of 5 T in 2021, and the scientific results obtained at beamlines 8, 9 and 10 show that the experiments significantly benefit from both, the improved beam stability and the increased flux of this new insertion device. In addition, the bending magnet station BL2 is now routinely available for small angle X-ray scattering experiments. In December 2020, a proposal for replacing some of the over 20-year-old components at the photoemission end-station of BL11 was approved. According to the specs, the set-up will allow experiments at ~ 20K with an energy resolution of approximately 15 meV. The new components' commissioning is scheduled in the second half of 2022. Machine-related activities included research on ultrashort UV-light pulses by coherent and echo-enabled harmonic generation. The research on terahertz radiation and the DELTA radiofrequency system were continued in 2021. New machine-learning projects covered the chromaticity control and an improved automated injection system.

A total of 9 reports on accelerator physics scientific projects and of 27 reports related to research with soft X-ray spectroscopy, hard X-ray scattering and hard X-ray spectroscopy provide a thorough compilation of the different activities carried out in 2021 at DELTA synchrotron radiation source. Again, the broad spectrum of studies from various scientific disciplines with both, fundamental and applied character, reflects the versatile usability of DELTA and its visibility in the research community.

Professor Dr. Metin Tolan has started with a new position as president of the University of Göttingen on April 1st, 2021. He has joint TU Dortmund in 2001 and since then he accompanied and strongly supported the development of DELTA to a user facility. We would like to take the opportunity to thank him for 20 years of continuous and highly engaged work for and at DELTA.

The success of DELTA is strongly and directly linked to the commitment and the enthusiasm of the scientists, the technicians, and the students involved in its operation. We would therefore thank the DELTA staff, all universities, research institutions and their contributing members for their efforts in difficult times, and we also highly acknowledge the support from TU Dortmund, the funding agencies and the local government. Stay safe and healthy, in the hope to meet you all soon in physical presence again in 2022.

Christian Sternemann, Ralph Wagner & Dirk Lützenkirchen-Hecht

Contents:

iii

Instrumentation

New Machine Learning Projects at DELTA

D. Schirmer, A. Althaus, S. Hüser, S. Khan, T. Schüngel

Zentrum für Synchrotronstrahlung (DELTA), Technische Universität Dortmund

In recent years, different machine learning (ML) projects have been investigated to support automated monitoring and operation of the DELTA electron storage ring facility. This includes self-regulating global and local orbit correction of the stored beam [1] and a betatron tune feedback [2]. Currently, the implementation of an ML-based chromaticity control and an electron transfer rate (injection) optimization is in preparation [3].

Chromaticity control

So far, the storage ring chromaticity values have been adjusted empirically based on experience. New settings can only be found by time-consuming trial and error. For this reason, an ML-based algorithm for automated chromaticity adjustment is currently being prepared, very similar to the already implemented ML-based betatron tunes control [2]. Classical, non-deep, feed-forward neural networks (NNs) are also used for supervised learning in this case. The method was successfully simulated (see Figs. 1 and 2) and is currently being transferred to real storage ring operation.
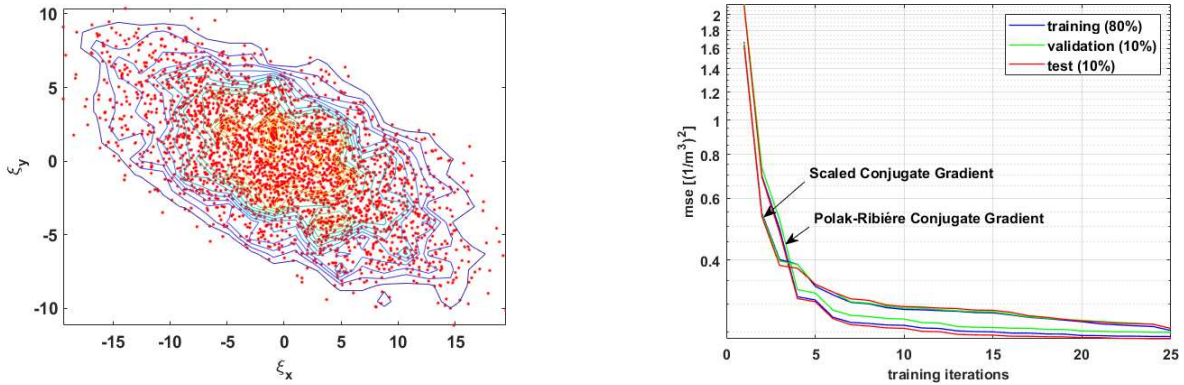
Figure 1: Left: Distribution of 3000 chromaticity shifts invoked by uniformly randomized strength variations of seven independent sextupole families. The data are obtained by optics calculations based on a DELTA storage ring model and are used for supervised training of NNs. Right: Comparison of network training performance functions ('fitness': mean squared NN output error as a function of training iterations) with simulated data applying two different conjugate gradient back-propagation methods [4]. With 80% of the data, the network is trained (blue curve) and 20% of the data are used for validation (10%) and test (10%) with "unseen" data sets (green and red curve). The continuously falling curves indicate significant fitness improvements without overfitting effects.
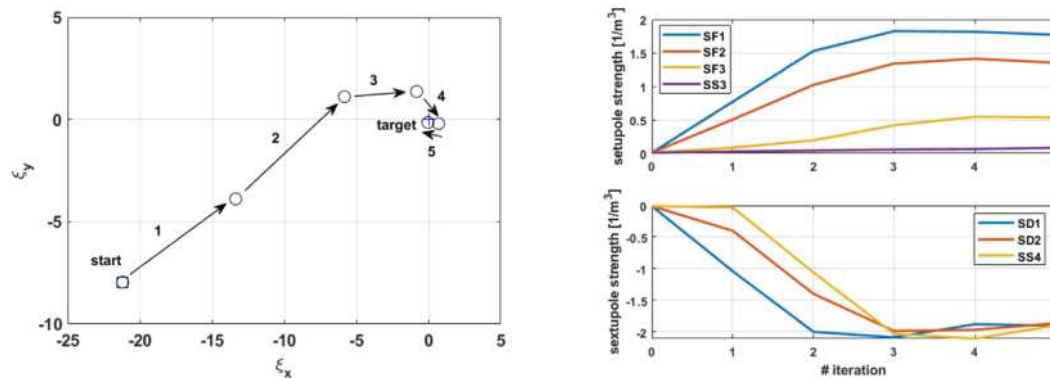
Figure 2: Left: Example for verification of NNs trained by simulated data (see Fig. 1, right) and applied to the DELTA storage ring model. The desired target values for compensated chromaticity (target values: $\xi_x = \xi_y = 0$) were reached in iterative steps starting at the setting for natural chromaticity ($\xi_x = -21$ and $\xi_y = -8$ with sextupoles switched off). Right: Strength settings for the horizontally (top) and vertically (bottom) focusing sextupole families during ML-based iterative matching to the target chromaticity values.

Automated injection efficiency optimization

Already in 2005, first attempts were made to optimize the electron transfer rate (injection efficiency) from the booster synchrotron to the storage ring by a combination of genetic algorithms and neural networks. Currently, this idea is being resumed but now with an expanded number of parameters and with a significantly enlarged database for ML-based training. In addition to the strength settings of the transfer line magnets, the injection elements of the storage ring (e.g., kicker magnets, magnets of a static injection bump) as well as the trigger timings of all pulsed transfer line and injection elements are now taken into account. To train surrogate injection models, NNs, decision trees as well as Gaussian process regression (GPR) methods are explored. First training results are depicted in Fig. 3 (left: GPR-based, right: NN-based). They show trained model predictions of the injection efficiencies as a function of approx. 750 measured transfer efficiencies.
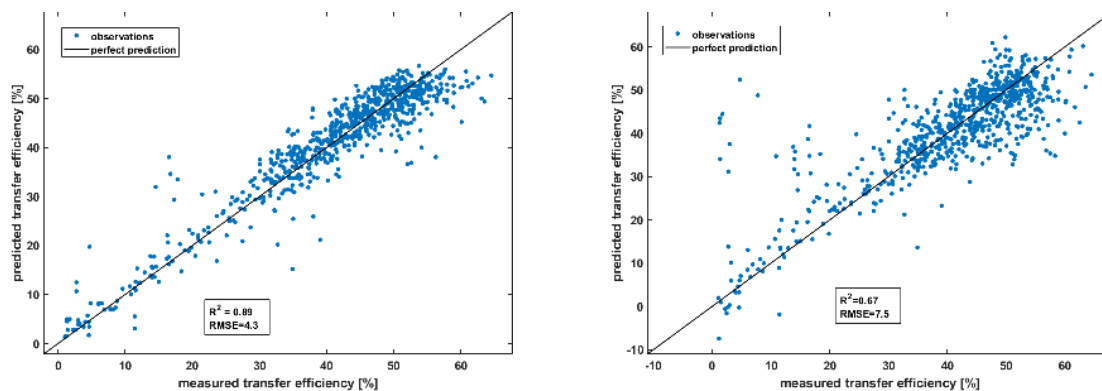
Figure 3: Left: Injection efficiencies predicted by a Gaussian process regression (GPR) model versus measured efficiencies. The machine learning was performed with approx. 750 measured data sets. The GPR applied the non-isotropic exponential kernel function for model adaption. The fit results in a correlation coefficient of $R^2 = 0.89$ and a root mean squared value (RMSE) of 4.3. Right: Injection efficiencies predicted by a surrogate model based on a narrow NN versus measured efficiencies. Machine learning was performed with the same 750 data sets as used for GPR-based modelling. The NN is composed of three fully connected ReLU-layers (28/10/1). The fit results in a correlation coefficient of $R^2 = 0.67$ and an RMSE of 7.5.

Both ML methods find clear correlations, whereby the GPR-trained model results in a significantly larger correlation coefficient R and thus seems to be more suitable for transfer rate modeling. The next step is to apply these surrogate models to keep the injection efficiency at a high level in an automated way using dedicated optimization algorithms without the need for operator intervention. These studies are currently being continued. Furthermore, it is planned to migrate all ML-based programs to a dedicated GPU-based ML server which provides a powerful hardware platform. To provide a user-friendly software framework for the future with more sophisticated ML applications, a Docker-container-based [5] ML workflow is foreseen.

[1] D. Schirmer, *Machine learning applied to automated orbit control at the 1.5 GeV electron storage ring DELTA*, Phys. Rev. Accel. Beams, submitted 12. Sep. 2021, under review.

[2] D. Schirmer, *Machine learning applied to automated tunes control at the 1.5 GeV synchrotron light source DELTA*, Proc. of IPAC 2021, Campinas, Brazil, 3379.

[3] D. Schirmer, A. Althaus, S. Hüser, S. Khan, T. Schüngel, *Machine Learning Projects at the 1.5 GeV Synchrotron Light Source DELTA*, Proc. of ICALEPCS 2021, Shanghai, China, WEPV007.

[4] M. F. Moller, *A scaled conjugate gradient algorithm for fast supervised learning*, Neural Networks, Vol. 6, 1993, 525–533.

[5] https://www.docker.com

Spectral Study of Radiation Background from the 7-T Superconducting Wiggler

S. Khan, B. Büsing, J. Friedl, C. Mai, and G. Schmidt

Zentrum für Synchrotronstrahlung (DELTA), Technische Universität Dortmund

In 2020, a 7-T superconducting wiggler (SCW) was installed and commissioned at DELTA [1], and new vacuum components to match the radiation intensity and angular distribution at 7 T are underway. The present vacuum chamber restricts the maximum magnetic field to 5 T at the nominal beam current of 130 mA. A higher field results in heating of the chamber and an increased radiation level in the DELTA hall. Using a recently commissioned high-purity germanium detector (ORTEC GEM-M5060-ICS-E) [2], photon spectra were recorded in the DELTA hall south of the radiation shielding wall (Fig. 1, left) at different settings of the SCW magnetic field, while the beam current was limited to 10 mA. Background at 0 mA (Fig. 1, magenta) was subtracted after the spectra were smoothed (Fig. 1, right).
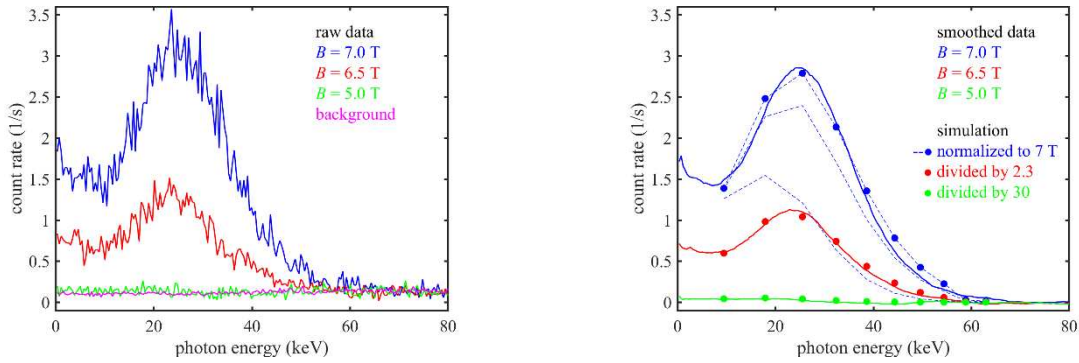
Figure 1: Photon spectra measured in the DELTA hall with SCW magnetic field 7.0 T (blue), 6.5 T (red), and 5.0 T (green) at a beam current of 10 mA as well as background without beam (magenta). Left: Raw data. Right: Smoothed data with background subtracted (solid lines) and calculated rates (dashed lines and bullets).

The spectral flux emitted by the SCW was calculated from 10 to 100 keV using the code SPECTRA [3]. To reproduce the measured spectra, Compton scattering near the inner surface of the vacuum chamber, energy-dependent absorption in the chamber wall, and Compton scattering in air was considered. To reach the detector outside the radiation shielding wall, the first scattering process was assumed to point upward ($\varphi \approx 90°$) and the second one downward ($\varphi \approx 180°$), shifting the photon energy twice by $E' = E / \left(1 + \{1 - \cos\varphi\} \cdot E / m_e c^2\right)$ with the electron rest mass m_e, see e.g. [4]. While the considered energy range represents the falling slope of the emission spectra, absorption in the chamber material strongly suppresses their low-energy part. The photon energy of the resulting maximum increases with the magnetic field (dashed lines in Fig. 1, right). Given the simplicity of the model, the good agreement with the measured spectral shape is certainly coincidental. However, it is significant that the calculated spectra normalized to the spectrum at 7.0 T have to be divided by 2.3 for 6.5 T and by 30 for 5.0 T to match the measured rates, indicating an onset of strong scattering around 6 T. The root-mean-square width of the radiation fan is $\sigma_\theta \approx K / \gamma \approx B[\text{T}] \cdot 3.9$ mrad, where

$K = 93.4 \cdot B[\text{T}] \cdot \lambda_\text{W}[\text{m}]$, B is the magnetic field, $\lambda_\text{W} = 0.125$ m is the wiggler period, and $\gamma \approx 3000$ is the Lorentz factor. Consistent with expectations, a width of $\sigma_\theta \approx 23$ mrad exceeds the aperture of the present vacuum chamber.

[1] G. Schmidt et al., *Installation and Conditioning of the 7-T Superconducting Wiggler at DELTA*, 16th DELTA User Meeting and Annual Report 2020, 15.

[2] M. Kebekus, *Installation und Inbetriebnahme eines Gammadetektors für die Compton-Rückstreuung am Elektronenspeicherring DELTA*, Bachelor thesis, TU Dortmund (2021).

[3] T. Tanaka, *Major upgrade of the synchrotron radiation calculation code SPECTRA*, J. Synchrotron Radiation 28, 1267 (2021).

[4] D. Griffiths, *Introduction to Elementary Particles* (Wiley-VCH 2008).

DELTA Radiofrequency Systems

P. Hartmann, V. Kniss, A. Leinweber and the DELTA team

Zentrum für Synchrotronstrahlung (DELTA), Technische Universität Dortmund

Linac RF System: The klystron tube of the linear accelerator was replaced with a new tube as part of the normal maintenance cycle. An old klystron tube, which previously served as a hot spare, was sent to the manufacturer who will check whether it can be refurbished and re-used.

Booster RF System: After a power failure in February 2021, a faulty module of the booster solid-state amplifier was discovered. Due to the redundant design of the amplifier, the replacement of the module could be postponed to a maintenance week in March.

Storage ring RF System: To generate the necessary cavity voltage in the EU-type cavity of the storage ring installed in 2018, less high-frequency power is required than previously anticipated. The relationship between forward power P_{fwd} and cavity voltage U_C is determined by the so-called shunt impedance of the cavity $R_S = U_C^2 / (2P_{\text{fwd}})$. This value is given in the literature as 3.4 MΩ [1] and 3.8 MΩ [2]. Own measurements of the shunt impedance by measuring the forward power and the cavity voltage with power meters resulted in a value of $R_S = 3.95 \pm 0.034$ MΩ. Since this value is significantly higher than the quoted values, two further beam-based measurements were carried out to confirm it.

For this purpose, two conditions were exploited that must be satisfied when matching the beam-loaded cavity impedance at beam current I_{DC} to the transmission line impedance. Matching is achieved when the forward power is fully accepted by the cavity and no power is reflected back to the amplifier. The beam-loaded cavity impedance

$$Z = \frac{\beta Z_0}{1 + 2I_{DC}R_S\cos(\varphi_S)/U_C + i\left(Q_0\xi - 2I_{DC}R_S\sin(\varphi_S)/U_C\right)}$$

is then equal to the transmission line impedance Z_0 [3]. This is the case, if

$$1 + 2I_{DC}R_S\cos(\varphi_S)/U_C = \beta \quad \text{and at the same time} \quad Q_0\xi - 2I_{DC}R_S\sin(\varphi_S)/U_C = 0.$$

Here, β is the coupling factor, Q_0 is the unloaded quality factor, φ_S is the synchronous phase, and $\xi \approx 2\,\Delta\omega/\omega_r$ describes the cavity detuning away from the resonance frequency ω_r. Figure 1 shows the reflected power from the cavity versus beam current measured at the EU-type cavity with U_{DC} = 387 kV and the other cavity detuned. The minimum is found at $I_{DC} = (60.3 \pm 0.1)$ mA. Together with the other parameters measured at the installation time of the cavity [3], this results in a shunt impedance of R_S = (3.90 ± 0.096) MΩ.

Another method to determine the shunt impedance uses the second matching condition. A relation between the detuned cavity phase Φ_C and a small deviation $\Delta\omega$ from resonance frequency is give by

$$Q_0\xi \approx 2(\Delta\omega/\omega_r)(1+\beta)Q_L = -(1+\beta)\tan\Phi_C,$$

where $Q_L = Q_0/(1+\beta)$ is the loaded quality factor.
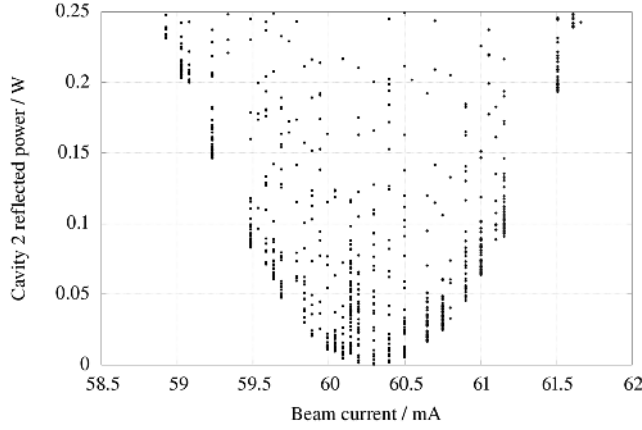
Figure 1: Reflected power of the EU-type resonator (cavity 2) vs. beam current. The vertical lines stem from the movement of the plunger.

For small deviations from ω_r, the RF frequency and the cavity phase have a fixed linear relationship via the quality factor. The cavity phase is, again for small frequency deviations, proportional to the the number of motor steps of the plunger stepper motor. Thus, the cavity phase can be calibrated by detuning the RF frequency and measured by counting the motor steps. This method can be used only if the cavity temperature is extremely stable. Once the calibration is done, the frequency is set to its nominal value and beam is injected into the storage ring. The beam loading leads to an inductive detuning of the cavity which is compensated by a movement of the plunger. A linear relation between the beam current and the cavity phase is obtained, represented by the motor steps from which the cavity shunt impedance can be derived using

$$\tan\left(\Phi_C\right) = -\frac{2R_s \sin\left(\varphi_s\right)}{\left(1+\beta\right)U_C} I_{DC} .$$

Figure 2 shows a typical procedure to measure the cavity shunt impedance by dynamic cavity detuning resulting in a shunt impedance of $R_S = (3.976 \pm 0.002)$ MΩ (see Fig. 3).
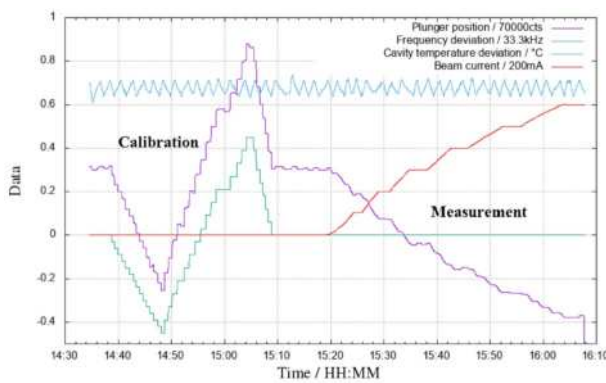
Figure 1: Measurement of the cavity shunt impedance R_S via dynamic cavity detuning.
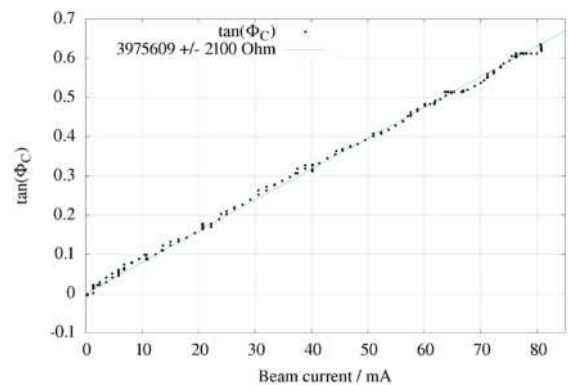
Figure 2: Shunt impedance R_S resulting from a fit to measurement data.

[1] E. Weihreter, *Status of the European HOM Damped Normal Conducting Cavity*, Proc. EPAC'08, Genoa, Italy, 2932.
[2] C. Christou, *Status of the Light Source RF*, 22nd ESLS-RF Meeting 2018, Paris, France.
[3] P. Hartmann, *Experience with RF Systems at DELTA*, 25th virtual ESLS-RF Workshop 2021.

Steady-state Solution of the Vlasov-Fokker-Planck Equation with a Split Beam in Synchrotrons

M.A. Jebramcik, S. Khan & W. Helml

Zentrum für Synchrotronstrahlung (DELTA), Technische Universität Dortmund

Recently, novel operation methods for synchrotron light sources have been explored: A promising idea is to operate the storage ring with transversely split beams. Additional stable fixed points are produced in the horizontal plane by operating the synchrotron on a resonance that is driven by the nonlinear sextupole or octupole magnets [1]. In the longitudinal phase space, a similar split can be produced by introducing an oscillation via a radiofrequency phase modulation. Such methods are applicable for hadron as well as electron storage rings. However, strong radiation damping in electron rings may change the dynamics of the system since the damping mechanism has to be overcome by the excitation before the additional fixed points can become populated by particles. Another important effect of radiation damping could be diffusion between the *islands* in phase space, in which case the question arises what kind of equilibrium state exists in the asymptotic temporal limit. We solve the Vlasov-Fokker-Planck equation using a finite-differences approximation in rotating action–angle coordinates to study these equilibrium states for the longitudinal as well as the transverse case. The number of solution vectors and the magnitude of the corresponding singular values of the design matrix of the underlying finite-differences equation are used as abstract indicators to define the required parameter set that provides stable additional beamlets, i.e., the beamlets have a diffusion lifetime that is close to that of the main beam.
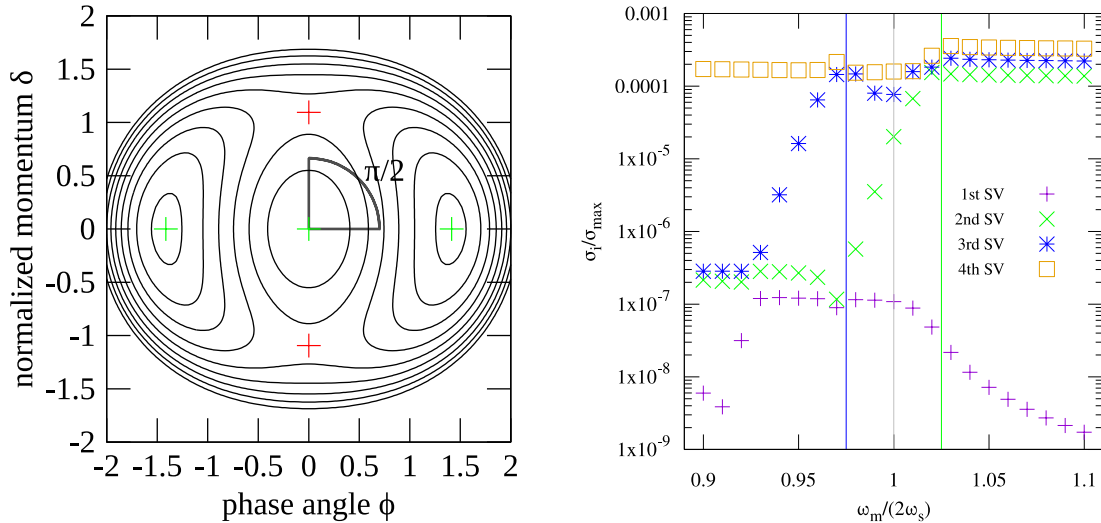
Figure 1: Left: Three-islands regime at the second integer resonance $m = 2$ with $1 - \omega_m/(2\omega_s) = 0.1$ and $A_m \tan\varphi_s = 0.1$. The three green markers indicate stable fixed points (FPs), while the red markers indicate unstable FPs. Right: Ratio between the four smallest singular values σ_i and the largest singular value σ_{max} versus the modulation frequency. At the upper bifurcation frequency (green line), the second smallest singular value (green crosses) starts to decrease since the lateral islands start to drift away from the centre and the two islands become disjoint at $\omega_m/(2\omega_s) \approx 0.97$. At the lower bifurcation frequency (blue line), the third singular value (blue stars) starts to decrease until the islands in the three-island regime become disjoint at $\omega_m/(2\omega_s) \approx 0.93$. All three states show roughly the same magnitude in terms of singular value compared to the fourth singular value (yellow boxes).

[1] P. Goslawski et al., *Two Orbit Operation at BESSY II During a User Test Week*, Proc. of IPAC 2019, Melbourne, Australia, 3419; doi: 10.18429/JACoW-IPAC2019-THYYPLM2

Ultrafast X-ray Sources and Angle-Resolved Electron Spectroscopy

L. Funke, S. Savio, N. Wieland, L. Wülfing, A. Held & W. Helml

Zentrum für Synchrotronstrahlung (DELTA), Technische Universität Dortmund

Over the past years, our group developed a novel and extremely powerful approach for the characterization of the temporal and spectral X-ray pulse structure at free-electron lasers (FELs) via the application of the "*attoclock*" technique [1, 2]. The experimental results provide direct information about the full time-energy distribution of the stochastic X-ray pulses with attosecond resolution on a single-shot basis, including X-ray pulse duration, intensity substructure and chirp. In the frame of the BMBF-Verbundprojekt 'Spectrometer with Angular Resolution for ultrafast experiments at X-ray FELs' (*SpeAR_XFEL*, grant number 05K19PE1) starting in July 2019, we are building on this experience for the construction of a new detector at the European XFEL with even better angular and temporal resolution. It consists of 20 electron time-of-flight detectors arranged in a ring-like structure perpendicular to the beam of the European XFEL. Together with a circularly polarized optical laser and suitable online analysis techniques based on novel machine learning methods, this setup allows to implement angular streaking. The temporal intensity distribution of the XFEL pulse is mapped to the streaked electron spectra, and their angle-dependent detection opens the door to pulse characterization with attosecond resolution. This spectrometer provides more flexibility for the scope of electron energies that can be detected simultaneously and is designed to be operated at high-repetition rate machines in the 100 kHz to MHz range.
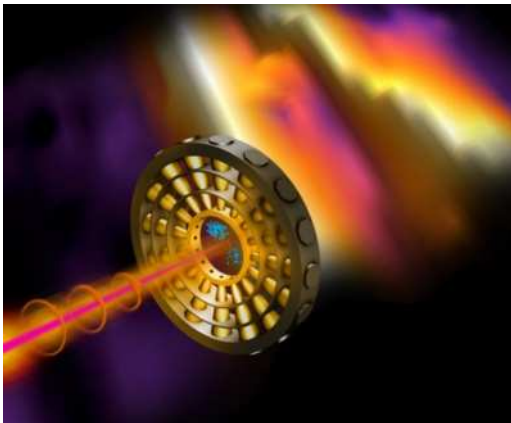
Figure 1: Ultrashort X-ray pulses (pink) at the Linac Coherent Light Source ionize neon gas at the center of a ring of detectors. An infrared laser (orange) sweeps the outgoing electrons (blue) across the detectors with circularly polarized light. (© Terry Anderson / SLAC National Accelerator Laboratory)

At the TU Dortmund and at the European XFEL, we have started to work on the details concerning simulation of electron trajectories in the time-of-flight tubes and connected technical design issues. These findings can assist the development of envisioned attosecond X-ray pulse shaping and integrated online diagnostic tools for high-repetition rate X-ray laser facilities. Our group at the TU Dortmund together with its collaboration partners at University Kassel and at DESY is actively driving and shaping this direction of research with the goal of ultrashort-pulse X-ray laser pump/probe experiments for time-resolved X-ray spectroscopy [3].

[1] N. Hartmann et al., *Attosecond Time–Energy Structure of X-ray Free-Electron Laser Pulses*, Nature Photonics 12, 215 (2018).

[2] R. Heider et al., *Megahertz-compatible angular streaking with few-femtosecond resolution at x-ray free-electron lasers*, Phys. Rev. A 100, 053420 (2019).

[3] K. Dingel et al., *Toward AI-enhanced online-characterization and shaping of ultrashort X-ray free-electron laser pulses*, ArXive: http://arxiv.org/abs/2108.13979.

Spectrotemporal Properties of CHG Radiation

A. Held, H. Kaiser, S. Khan, A. Radha Krishnan, V. Vijayan

Zentrum für Synchrotronstrahlung (DELTA), Technische Universität Dortmund

At the 1.5-GeV synchrotron light source DELTA, coherent harmonic generation (CHG) is employed to produce ultrashort radiation pulses in the vacuum ultraviolet (VUV) spectrum. This is achieved via a laser-induced electron energy modulation which is then converted to density modulation by a dispersive chicane. Since the resulting radiation depends directly on the seed laser pulse, the spectrotemporal properties of the CHG pulses can be manipulated by the chirp of the seed laser pulses and the strength of the dispersive chicane R_{56} [1].

CHG spectra around wavelengths of 400 nm, 266 nm, and 200 nm were recorded under variation of the chicane strength and the chirp of the 800-nm seed laser pulses. The spectral phase of the laser pulses was controlled by adjusting the compressor of the laser amplifier and was observed using frequency resolved optical gating (FROG) [2]. An iCCD camera was employed to record single-shot spectra while the chicane currents were varied from 0 to 700 A as shown in Fig. 1.
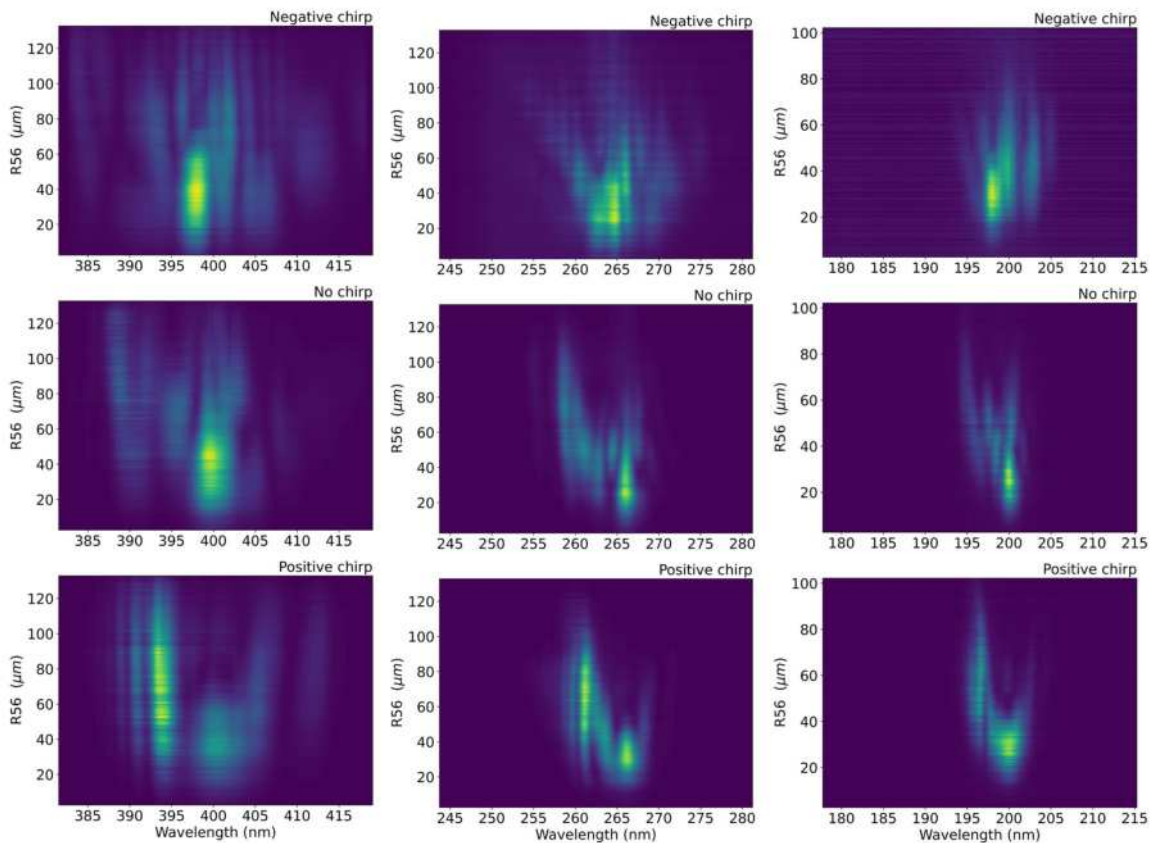
When the chicane strength is increased beyond the optimum value, electrons which have interacted with the head and tail of the laser pulse produced microbunches while those with the maximum energy modulation get overbunched causing an interference between two coherently emitted pulses. An unchirped laser pulse results in spectra with interference fringes from two pulses of the same frequency. For a strongly chirped seed pulse, the spectra show two peaks at the frequencies corresponding to head and tail of the pulse. In Fig. 1, however, prominent interference fringes can be seen for seed pulses with a negative chirp because extra chirp is introduced by the lenses and vacuum window in the beam path. For positive chirps, the plots show two prominent peaks as expected. A previous study showed similar results [3]. However, the spectra exhibit many extra features which are not easily explained. This suggests a strong non-linear chirp which calls for further investigation.

[1] S. Khan et. al., *Spectral Studies of Ultrashort and Coherent Radiation Pulses at the DELTA Storage Ring*, Proc. of IPAC 2016, Busan, Korea, 2851 (2016).

[2] R. Trebino, *Frequency-Resolved Optical Gating*, Kluwer (2000).

[3] S. Khan et. al., *Seeding of Electron Bunches in Storage Rings*, Proc. of FEL 2017, Santa Fe, NM, USA, 94 (2017).

Progress Towards the EEHG Upgrade of the Short-Pulse Source

B. Büsing, H. Kaiser, S. Khan, A. Radha Krishnan

Zentrum für Synchrotronstrahlung (DELTA), Technische Universität Dortmund

Overview: Since 2011, a short-pulse source is operated at the DELTA storage ring [1]. The coherent harmonic generation scheme (CHG) [2] allows to generate ultrashort pulses by an interaction of laser pulses with electron bunches in an undulator (modulator). In a dispersive chicane, the laser-induced energy modulation is transformed into a density modulation. This so-called microbunching leads to coherent emission of radiation at harmonics of the laser wavelength in a subsequent undulator (radiator). This scheme is limited to low harmonic numbers n since the bunching factor scales proportional to e^{-n}. Higher harmonics can be achieved through a different seeding technique named echo-enabled harmonic generation (EEHG) [3] which requires another laser-electron interaction and a strong chicane prior to the magnetic setup used for CHG, see Fig. 1. Here, the final density profile consists of microbunches with a high-frequency substructure enabling coherent emission at much higher harmonics since the bunching factor scales proportional to $n^{-1/3}$. To implement this scheme at DELTA, it is necessary to modify 1/4 of the storage ring to accommodate the 2 undulators and chicanes in one long straight section.
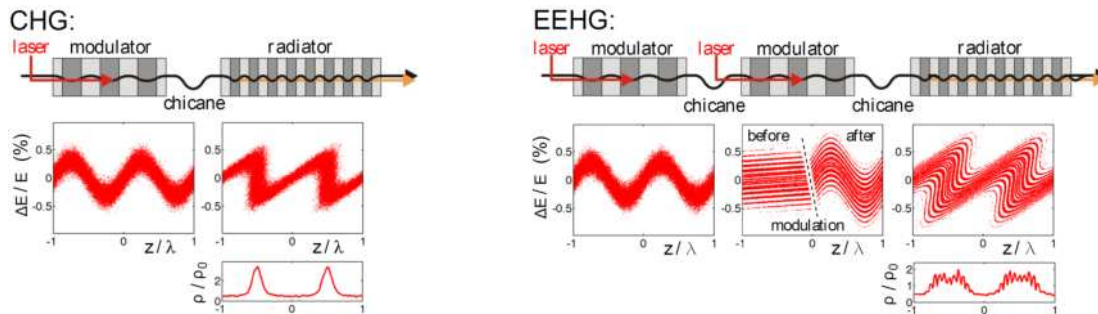
Figure 1: Left: CHG principle with laser-induced energy modulation in one undulator (modulator) converted into microbunching by a magnetic chicane and coherent emission at high laser harmonics in a second undulator (radiator). Right: EEHG principle with twofold laser-induced energy modulation.

Magnet Positions and Vacuum Concept: The future magnet positions were found by simulating the beam optics with the simulation code ELEGANT [4], matching the boundary conditions for the beta functions, the dispersion function and the length of the straight section. To create a long straight section, the 3° and 7° dipoles are replaced by 10° dipoles. The present and the future magnet configuration is shown in Fig. 2. The vacuum chambers for the 10° dipoles, where the laser pulses are coupled in and synchrotron radiation is coupled out, are designed and a call for tender is in preparation. A large fraction of the existing vacuum chambers is planned to be reused.
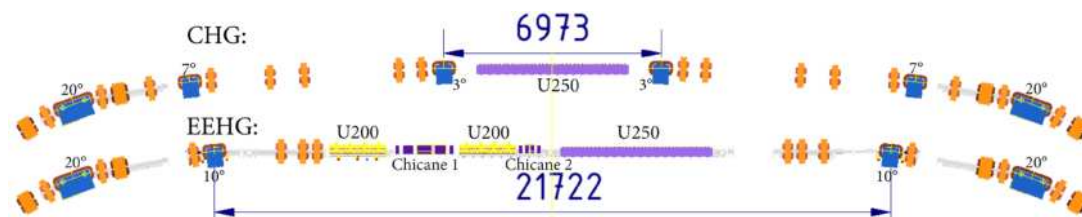
Figure 2: Top: Present CHG configuration. Bottom: Planed EEHG configuration in the northern part of the DELTA storage ring.

Undulators: The electromagnetic undulator U250 which is currently used as modulator, chicane and radiator will be reused as the radiator in the EEHG setup. The two energy modulations will take place in two new electromagnetic undulators U200. These undulators are in house and characterized [5]. The main parameters are given in the following table:

Parameter	U200	U250
Total length (m)	1.85	4.85
Period length (cm)	20	25
Number of periods	7	17
max. B field (T)	0.62	0.76

Chicane Magnets: A preliminary design for the chicane magnets was prepared and electromagnetic simulations were carried out using CST Studio [6]. While the second chicane consists of 4 identical magnets, the first chicane employs an unconventional 5-magnet design to keep the maximum horizontal displacement of the electrons sufficiently small so that the present vacuum chamber can be reused. The requirements regarding maximum longitudinal dispersion R_{56} and a tolerable transfer matrix element R_{51} were also explored. The dimensions of the chicanes are shown in Fig. 3.
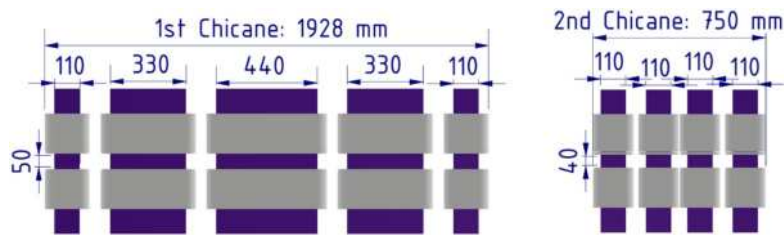
Figure 3: Dimensions of the first and second magnetic chicane for the EEHG scheme.

[1] S. Khan et al., *Generation of Ultrashort and Coherent Synchrotron Radiation Pulses at DELTA*, Sync. Rad. News 26:3, 25 (2013).

[2] R. Coisson and F. De Martini, *Free-electron coherent relativistic scatterer for UV-generation*, Quantum Electronics, vol.9, p. 939, 1982.

[3] G. Stupakov, *Using the Beam-Echo Effect for Generation of Short-Wavelength Radiation*, Phys. Rev. Lett. 102, 074801 (2009).

[4] M. Borland, *elegant: A Flexible SDDS-Compliant Code for Accelerator Simulation*, Advanced Photon Source LS-287, September 2000.

[5] D. Zimmermann, *Aufbau eines Magnetmessstandes zur Feldvermessung von Undulatoren bei DELTA*, master thesis, TU Dortmund (2016).

[6] CST STUDIO SUITE ®, https://www.cst.com/products/csts2

A New Setup for the Spectroscopy of Compton-Backscattered Laser Photons at DELTA

C. Mai, M. Hagemeier, S. Khan, M. Kebekus, B. Sawadski

Zentrum für Synchrotronstrahlung (DELTA), Technische Universität Dortmund

The planning of a setup to measure the electron energy at DELTA with high precision started in 2020. It is aimed to measure the electron energy and resolve the relative energy spread which is, according to calculations, about $6.8 \cdot 10^{-4}$ [1]. One of the most precise methods to measure the beam energy at an electron storage ring is the spectroscopy of Compton-backscattered laser photons [2]. At DELTA, a setup using a CO_2 laser is currently under commissioning. The laser (PL5, Edinburgh Instruments) emits light from a selectable single laser line between 9 μm and 11 μm in continuous wave (CW) mode. In a head-on scattering process of the laser photons and the electrons, the initial photon energy of 117 meV will be shifted to about 4 MeV. The spectrum of the backscattered photons will be measured by a high-purity germanium (HPGe) detector and the energy of the Compton edge will then allow to calculate the beam energy. Figure 1 shows an overview of the setup.
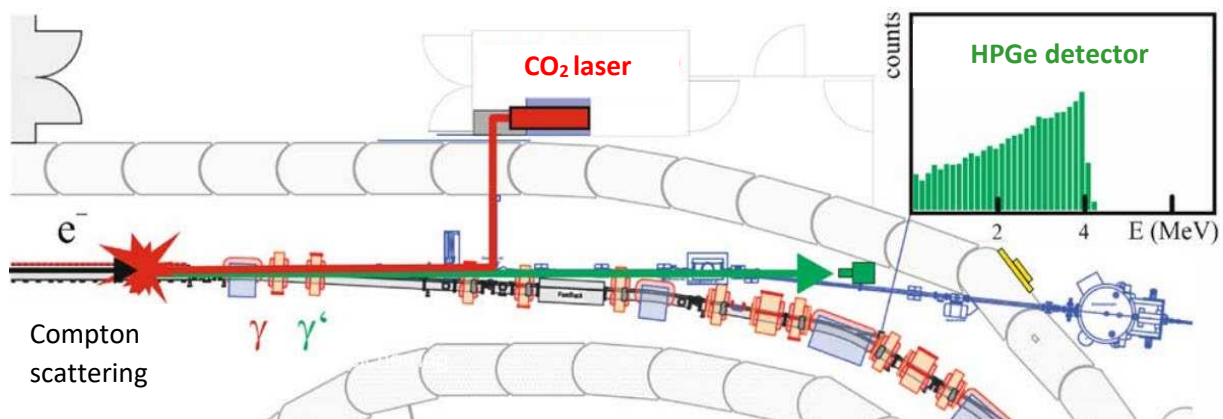
Figure 1: North-eastern section of DELTA and the Compton-backscattering experiment. The laser beam of the recently commissioned CO_2 laser (red box) will be coupled into the DELTA vacuum chamber through beamline 4. The scattering process will occur along the northern straight section and a HPGe detector (green) will measure the energy of the backscattered photons.

The commissioning of the experiment was divided into three main work packages:

1. Preparation of the beamline 4 laboratory for the CO_2 laser and its installation.
2. Design of a laser telescope to control the beam diameter and divergence along the interaction line.
3. Design of the mechanical support for the HPGe detector and test of an online detector calibration routine.

In 2020, the air-conditioned hutch at beamline 4 was extended to provide enough space for a new optical table holding the CO_2 laser. Unfortunately, the commissioning and first lasing was delayed until September 2021 due to COVID-19 travel restrictions. A maximum output power of 68 W was achieved after optimization which exceeded the specification of 50 W by far. Work packages 2 and 3 were carried out in the scope of two bachelor's theses. The laser telescope consisting of three ZnSe lenses will allow to adjust the waist of the laser beam

between 3.5 mm and 12 mm [3]. To avoid thermal damage of the vacuum chamber caused by the high laser power, the telescope is designed such that the laser beam can be coupled out of the chamber behind the interaction region.

The HPGe detector is read out by a multi-channel analyzer. A precise calibration is necessary to achieve a sufficient energy resolution. To account for drifts between the measurements, a procedure allowing to recalibrate the energy scale of the detector without external radioactive sources was tested [4]. Very small amounts of the radioactive isotopes [214]Bi, [228]Ac, [40]K and [208]Ti are present in the radiation protection wall of the accelerator providing six spectral lines of well-known energy [5] which can be used for the calibration. Figure 2 shows the respective calibration curve. A final relative resolution of $3\cdot10^{-5}$ is achieved.
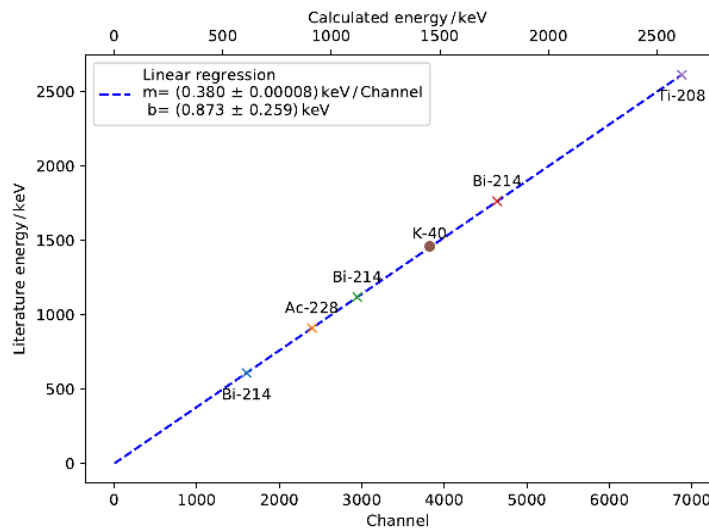
Figure 2: Calibration of the channel-to-energy relation of the HPGe detector output.

During the next months, the laser telescope will be set up as designed [3] and the detector will be permanently installed on a remotely controlled 2-dimensional stage at the storage ring. It is expected that first measurements will be conducted in late 2022.

[1] D. Schirmer, *Synchrotron radiation sources at DELTA*, Interner Bericht, Zentrum für Synchrotronstrahlung, TU Dortmund University (2009).
[2] A. Chao, *Handbook of Accelerator Physics*, World Scientific (1999).
[3] M. Hagemeier, *Optische Einkopplung eines CO2-Laserstrahls in den Elektronen-speicherring DELTA,* Bachelor's thesis, TU Dortmund (2021).
[4] M. Kebekus, *Installation und Inbetriebnahme eines Gammadetektors für die Compton-Rückstreuung am Elektronenspeicherring DELTA,* Bachelor's thesis,TU Dortmund (2021).
[5] R.B. Firestone et al., *Table of Isotopes*, Wiley-Interscience (1999).

Long-Term Observation of Coherently Emitted THz Pulses

C. Mai, B. Büsing, A. Held, S. Khan

Zentrum für Synchrotronstrahlung (DELTA), Technische Universität Dortmund

At the short-pulse source of DELTA, the interaction of an ultrashort laser pulse is used to modulate the electron energy inside the electromagnetic undulator U250. Due to the dispersive properties of the storage ring, the off-energy electrons move ahead or fall behind leaving a sub-picosecond dip in the longitudinal electron density. This gives rise to the coherent emission of synchrotron radiation in the (sub-)THz range which is analyzed at a dedicated beamline (BL5a) at DELTA. During the subsequent turns in the storage ring, the density dip persists (see Fig. 1) but gets wider which leads to a shift of the emission frequency from several THz to the sub-THz regime [1].
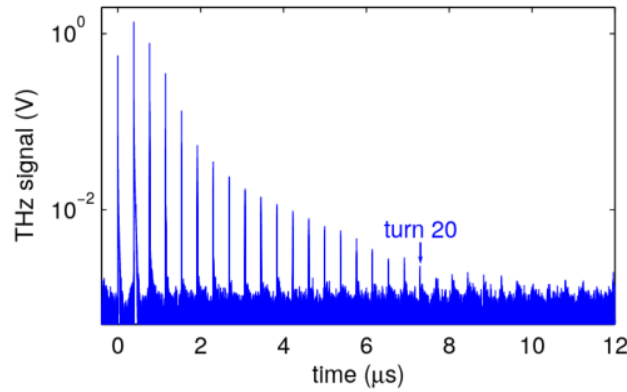
Figure 1: Measurement of coherently emitted THz pulses during 20 turns after the electron bunch was energy-modulated by a short laser pulse.

In 2015, a reoccurrence of a weak THz signal after half a synchrotron period (about 75 turns) was observed for the first time [2]. The synchrotron motion causes an oscillation between off-energy and off-phase states of each electron. After half an oscillation period, the energy modulation distribution has rotated by 180º in the longitudinal phase space which means that the former density structure reoccurs.
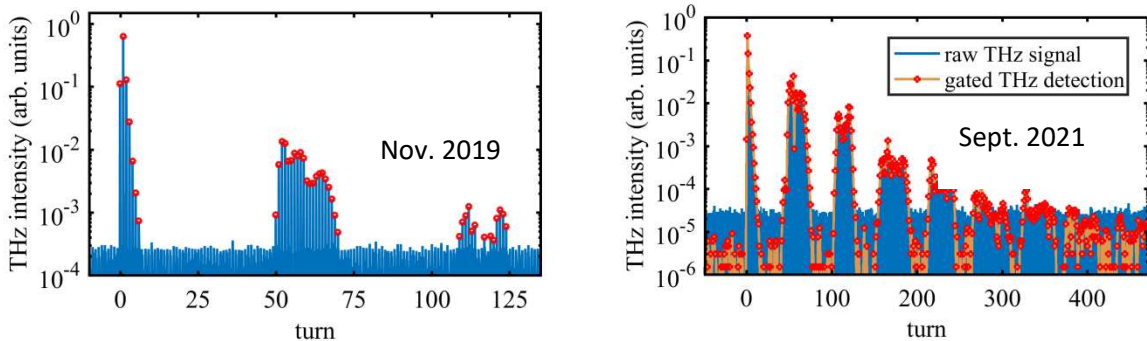
Figure 2: In 2019, the installation of the second RF cavity led to an increase of the synchrotron oscillation frequency which allowed to detect THz signals after a full synchrotron oscillation period (left). In 2021, the measurement was repeated taking more data to reduce the noise floor by averaging. The THz signal can be observed for about 350 turns (right). To detect signals with an amplitude comparable to the noise floor, a gate was used in the analysis to mark the correct data (orange curve).

After the installation of the additional radiofrequency (RF) system in 2019 [3], the synchrotron frequency was increased from about 16 kHz to 22 kHz. The shorter oscillation period allowed to observe coherently emitted signals even after a full synchrotron period which amounts to about 120 revolutions (see Fig. 2, left).

Recently, the experiment was repeated averaging over more data which led to an improvement of the noise level by one order of magnitude (Fig. 2, right). This allowed to observe coherently emitted signals for at least 350 revolutions. Besides the generally lower noise floor, the dynamic range was increased by combining datasets with different signal amplification. Since the arrival time of the THz pulse is precisely known, a software gate was used to visualize THz amplitudes even below the noise floor. The orange curve in Fig. 2 is given by the maximum value in a window of 250 ps width which is symmetric about the expected arrival time. Comparing the gated detection before the laser-electron interaction (turn < 0) and at the end of the acquisition (turn 450) leads to the assumption that weak remainders of the energy modulation are present for an even longer time.

Given that the time between two laser pulses used for the energy modulation is 1 ms, it is astonishing that coherent THz emission is observed over 15% of that period. The structure of the THz emission gives new insight into the longitudinal dynamics and promises to allow the derivation of further storage ring parameters such as higher orders of the synchrotron frequency.

[1] C. Mai et al., *Time-resolved spectral observation of Coherent THz Pulses at DELTA*, Proc. of IPAC 2016, Busan, Korea, 105.

[2] C. Mai et al., *Observation of Coherent Pulses in the Sub-THz Range at DELTA*, Proc. of IPAC 2015, Richmond, VA, USA, 823.

[3] P. Hartmann et al., *DELTA radiofrequency systems*, DELTA Annual Report 2019, 3.

First GISAXS experiments at Beamline BL2

Lisa Randolph[1], Kai Schlage[2], Mehdi Ramin Moayed[2], Motoaki Nakatsutsumi[3], Christian Gutt[1], Michael Paulus[4]

[1]Department Physik, Universität Siegen, Walter-Flex-Str. 3, 57072 Siegen, Germany
[2]Deutsches Elektronen-Synchrotron DESY, Notkestrasse 85, 22607 Hamburg, Germany
[3] European XFEL, Holzkoppel 4, 22869 Schenefeld, Germany
[4]Fakultät Physik/DELTA, TU Dortmund 44221 Dortmund, Germany

During the last years an experimental setup for small-angle X-ray scattering (SAXS) has been installed at beamline BL2, mainly to study biological samples in an aqueous environment. The setup consists of a multilayer monochromator with a bandwidth of 1.5%, a sample environment for pressure and temperature control, a 1300 mm long flightpath and a MAR345 image plate detector. Alternatively, to the MAR345 a PILATUS100k detector can be used. The beam cross section is defined by two slit systems. Here, we demonstrate the first grazing-incidence small angle x-ray scattering (GISAXS) measurements at BL2 by making use of the good parallelism of the X-ray beam. This method provides access to the surface and subsurface density distribution.

Figure 1: GISAXS pattern of the two Pt nanorod samples.

The experiment was performed with a photon energy of 12 keV at a grazing incidence angle of 0.5°. The scattered X-ray photons around the specular reflection ($\alpha_i = \alpha_f$) were recorded by the MAR345 image plate detector with an exposure time per image of 20 s. The strong specular peak was blocked by a beam stop because it is orders of magnitude more intense. We investigated Platinum (Pt) nanorods with 20 nm length, 10 nm thickness and a mutual distance of 20 nm deposited on a silicon wafer with a tilt angle of 80° with respect to the sample surface. Due to the non-isotropic orientation of the nanorods, we investigated the sample in both directions, with tilt in beam direction and tilt perpendicular to the beam direction.

Fig. 1 shows the raw data of the two measurements. On the left side one can clearly see an asymmetry in the scattering pattern caused by the tilt of the nanorods perpendicular to the beam direction. On the right hand side of Fig. 1, the scattering pattern is symmetrical due to the tilt in beam direction. In addition to the scattering signal of the sample, another scattering contribution can be seen which has been illustrated by a black rectangle in Fig. 1 on the

Figure 2:Scattering signal as a function of wave vector transfers Q_y and Q_z (parallel and perpendicular to the sample surface) and a cut along Q_y.

right. This signal is caused by scattering from the air in front of the sample and should be eliminated in a further extension of the setup by a slit system. Fig. 2a) shows the scattering signal as a function of wave vector transfers Q_y and Q_z (parallel and perpendicular to the sample surface) and Fig. 2b) illustrates a cut along Q_y. The correlation peak at 0.35 nm^{-1} as shown in the green box indicates a distance of about 20 nm between the nanorods.

In summary, we have clearly shown that GISAXS experiments are possible at the beamline BL2. By further suppressing the scattering background, it may also be possible to investigate weaker scattering samples.

Prospects and limits for X-ray emission spectroscopy at DELTA

Nicola Thiering, Christian Albers, Eric Schneider, Michael Paulus, Christian Sternemann

Fakultät Physik/DELTA, Technische Universität Dortmund, 44227 Dortmund

Aim of this experiment was to evaluate the capabilities for X-ray emission spectroscopy at DELTA for studies of the electronic and structural properties of matter via detection of K_β and valence-to-core spectra of transition metals, here iron and vanadium. We used a von Hamos spectrometer set-up at beamline BL9 in combination with a Pilatus 100K detector (see Fig. 1). Although not shown for clarity, a helium filled bag between von Hamos spectrometer, sample, and detector was used together with extensive shielding of both sample environment and detector in order to prevent scattering and absorption in air resulting in a highly improved signal to background ratio. The incident radiation was monochromatized by a Si(311) monochromator to 10800 eV and a beam size of 1.0 x 0.2 mm^2 (v x h)

was used. The von Hamos spectrometer was equipped with four cylindrically bent Si(110) and four Ge(211) analyzers with bending radius of 500 mm to study iron containing coordination polymer and vanadium enriched industrial coatings, respectively.

The capabilities of this setup to probe temperature induced spin state changes were constrained using the coordination polymer $[Fe(pz)_{0.5}(NH-pz)_{0.5}Pt(CN)_4]$. This polymer undergoes a spin crossover transition from a high-spin (HS) to a low-spin (LS) state in a temperature range between 150 K and 250 K [1] and serves as reference system for K_β spectroscopy. The temperature of the sample which
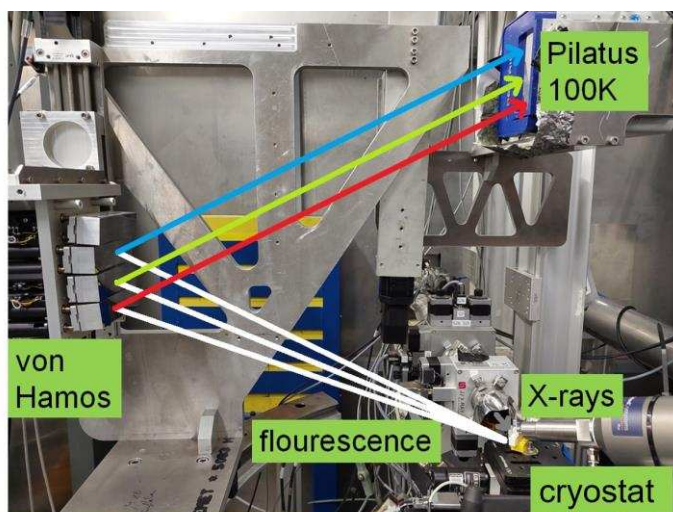
Fig. 1: The von Hamos spectrometer setup at beamline BL9 with a Pilatus 100K detector and cryostat to probe temperature induced spin state changes.

was contained in a quartz-glass capillary was varied using an Oxford Cryostream system. The energy calibration of the setup was performed by measurements of the quasi-elastic lines in the energy range between 10500 eV and 10680 eV. Subsequently, the iron K_β emission was measured between room temperature and 176.7 K in several steps. For each spectrum data were acquired between 2.5 and 6.0 hours. In Fig. 2 two typical spectra are presented, one for iron being in the HS state at 253.2 K and the other for LS iron at 176.7 K. The spin transition is clearly indicated by a significant decrease of the so-called $K_{\beta'}$ satellite intensity as well as the shift in emission energy of the $K_{\beta 1,3}$ emission line. We determined the spin transition to occur at about 203 ± 5 K. The incident flux was not sufficient to detect the valence-to-core signal with sufficient statistical accuracy.

In order to test application for lower emission energies we probed the $K_{\beta 1,3}$ and valence-to-core emission of vanadium at 5427 eV and 5463 eV, respectively. For this experiment the von Hamos

spectrometer was equipped with 4 cylindrically bent Ge(211) analyzers and the samples were two coatings of different vanadium content. While the $K_{\beta1,3}$ could be detected with similar quality than that of iron, it was not possible to measure the vanadium valence-to-core emission which is necessary to study the electronic and structural properties of vanadium in these coatings. Hence, for valence-to-core emission studies the incident flux at BL9 is not sufficient owing to the small bandpass of the Si(311) monochromator.

As monochromatic excitation is in most cases not required for X-ray emission studies, this von Hamos setup will be tested at beamline BL2 of DELTA using filtered white beam or pink beam excitation in order to increase the incident flux significantly to make valence-to-core spectroscopy available at DELTA.

Fig. 2: Temperature induced HS to LS transition in [Fe(pz)$_{0.5}$(NH-pz)$_{0.5}$Pt(CN)$_4$] detected via K$\beta_{1,3}$ emission spectroscopy.

References

[1] J.A. Real et al., Coordination Chemistry Review, 2003, **236**, 121-141

Acknowledgments

Opportunities for time-resolved X-ray absorption spectroscopy at DELTA beamline 10

D. Lützenkirchen-Hecht[a], A. Šarić[b], F. Eckelt[a], M. Vrankić[b], S. Paripsa[a], R. Wagner[a]

a) Bergische Universität Wuppertal – Fakultät für Mathematik und Naturwissenschaften, Gauß-Str. 20, 42097 Wuppertal, Germany.

b) Division of Materials Physics, Centre of Excellence for Advanced Materials and Sensing Devices, Ruđer Bošković Institute, Bijenička 54, 10000 Zagreb, Croatia.

X-ray Absorption Spectroscopy (XAS) is a standard technique for structure determination of solid or liquid, crystalline and non-crystalline samples (see, e.g. [1,2]), and it consists in the precise determination of the X-ray absorption coefficient around an absorption edge of a selected element. XAS contains element-specific information about the local geometric structure such as bond distances and coordination numbers, as well as electronic information about the chemical valence and the density of unoccupied states [1,2]. Usually, the XAS spectra, typically covering a photon energy range of about 1 keV, are measured on a step-by-step basis with an integration time of about several seconds for each data point in the spectrum, so that the acquisition of an entire spectrum takes 10-30 minutes or even more. Due to the advances of synchrotron light sources in the past years, the photon flux provided by current insertion devices allows a substantial reduction of the integration time, resulting in acquisition times of a few seconds for individual spectra, and by employing dedicated monochromator setups and detector equipment, XAS spectra can be measured within some few milliseconds only [3-5], allowing e.g., time-resolved studies of chemical reactions, thin film growth processes, etc. At DELTA, recently a new wiggler has been implemented as the source for beamlines 8, 9 and 10 [6]. In conjunction with the stable channel-cut monochromator installed at beamline 10 [7], ideal prerequisites for time-resolved XAS are thus available at DELTA. Here we will thus present some preliminary results of time-resolved XAS experiments at BL10.

For the present results, a Si(111) channel-cut monochromator was employed, and N_2- and Ar-filled ionization chambers were used to measure the incident and the transmitted intensities, respectively. As an exemplary sample, ZnO nanoparticles prepared by hydrolysis of zinc acetylacetonate monohydrate ($Zn(acac)_2 \cdot H_2O$) as described in detail in ref. [8] were used. The dried powder samples were mixed with suited amounts of boron nitride and dispersed on self-adhesive paper, several stacks of which were measured in transmission mode in the vicinity of the Zn K-edge (9659 eV). In particular, we have placed the samples in a bath cryostat filled with liquid nitrogen, and the measurements were performed after equilibration at 77 K.

Scans ranging from 9600 eV to 10700 eV with different integration times per data point are compared in Figure 1; both normalized absorption data as well as the extracted, k^3-weighted EXAFS fine structure oscillations $k^3 * \chi(k)$ are presented. As can be seen, almost noise-free absorption data can be collected up to ca. 120 eV above the Zn K-edge for all the spectra, suggesting that fast time-resolved X-ray absorption Near Edge Edge Spectroscopy (XANES) data are feasible with a time resolution of a few seconds only. The $k^3 * \chi(k)$ - data calculated from the presented spectra are almost identical up to a photoelectron wave-number of ca. 12.5 Å^{-1}, indicating that meaningful structural information may be extracted from the data accordingly [9].
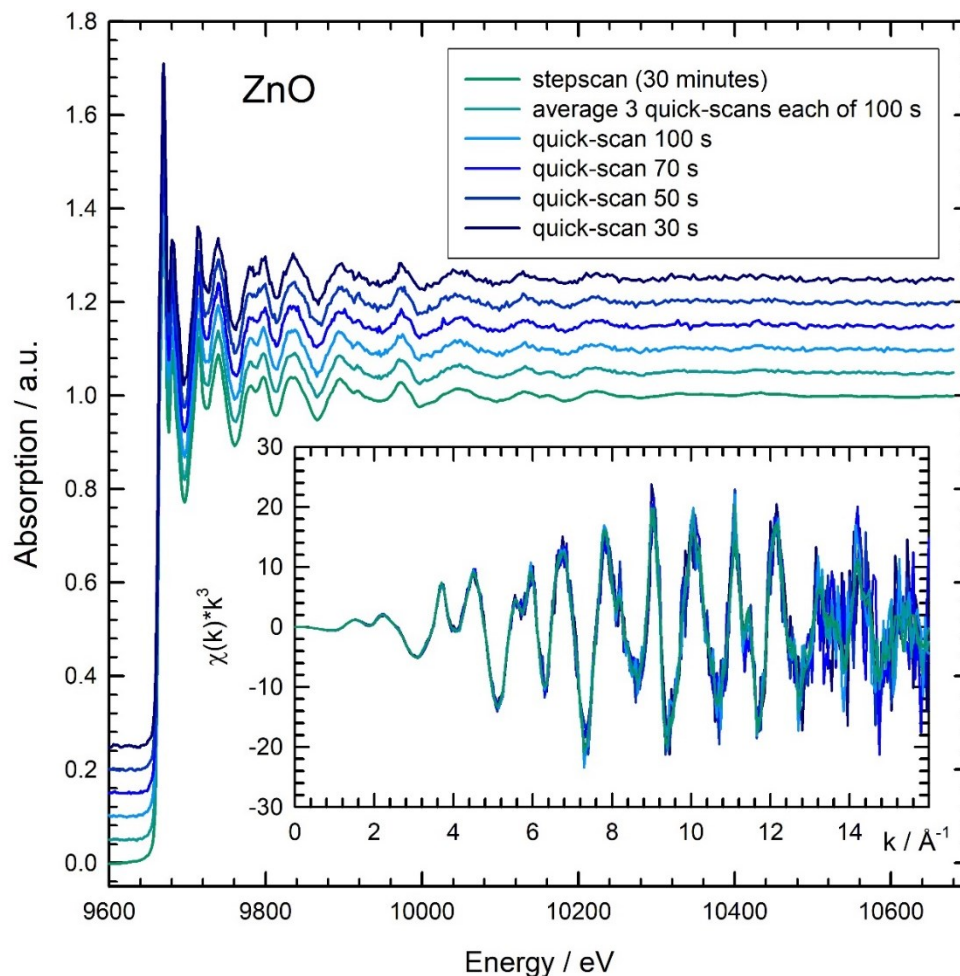
Fig. 1: Comparison of Zn K-edge X-ray absorption data of a nanosized ZnO material measured at 77 K employing different scan speeds and integration times per data point. In the insert, the k^3-weighted EXAFS fine structures $\chi(k)*k^3$ are shown.

A more detailed data evaluation including fits of the spectra and a determination of bond distances (see [10]) and error estimates is currently under-way. Future applications of this time-resolved technique for real time-resolved studies of chemical reactions are planned for 2022.

Acknowledgements:

References:

[1] D.C. Koningsberger, R. Prins (Eds.): X-Ray Absorption, Principles, Applications, Techniques of EXAFS, SEXAFS and XANES, John Wiley & Sons, New York (1988).
[2] J.J. Rehr and A.L. Ankudinov, J. Synchrotron Rad. 8 (2001) 61.
[3] J. Stötzel, D. Lützenkirchen-Hecht and R. Frahm, Rev. Sci. Instrum. 81 (2010) 073109.
[4] O. Müller, D. Lützenkirchen-Hecht and R. Frahm, Rev. Sci. Instrum. 86 (2015) 035105.
[5] B. Bornmann, J. Kläs, O. Müller, et al., AIP Conf. Proc. 2054 (2019) 040008.
[6] G. Schmidt, A. Althaus, B. Büsing, et al., DELTA annual report (2020) 15.
[7] D. Lützenkirchen-Hecht, R. Wagner, S. Szillat, et al., J. Synchrotron Rad. 21 (2014) 819.
[8] S. Musić, A. Šarić, Ceram. Int. 38 (2012) 6047.
[9] E. Stern, Phys. Rev. B 48 (1993) 9825.
[10] A. Šarić, F. Eckelt, M. Vrankić, et al., DELTA annual report (2020) 105.

Soft X-ray Spectroscopy

Investigation of sub-monolayer Sn phases on Au(111) by means of XPS and LEED

J. A. Hochhaus[1,2,*], **L. Kesper**[1,2], **U. Berges**[1,2], and **C. Westphal**[1,2]

[1] Experimentelle Physik I - Technische Universität Dortmund, Otto-Hahn-Str. 4a, D-44227 Dortmund
[2] DELTA - Technische Universität Dortmund, Maria-Goeppert-Mayer-Str. 2, D-44227 Dortmund
* corresponding author: julian.hochhaus@tu-dortmund.de

The discovery of graphene in 2004 with its remarkable mechanical and electronic properties paved the way for the investigation of other 2D materials from the carbon group, the so-called Xenes. Analogous to graphene, these two-dimensional materials are arranged in a honeycomb structure, while their electronic properties differ significantly from their three-dimensional counterparts. Stanene, as well as the other two-dimensional materials of the carbon group are also known as Dirac-materials. The charge carriers in the material can be described by the relativistic Dirac equation, since a characteristic Dirac cone with linear dispersion relation in their band structure can be observed [1].

While graphene is sp^2 hybridized, the interatomic bond length for the heavier 4th main group elements becomes progressively larger, which reduces the probability of forming strong π-bonds and instead leads to a mixture of sp^2/sp^3 hybridization [2]. Stepping down the carbon group, the materials show increasingly larger buckling, in contrast to the nearly atomically flat graphene. In addition, the spin-orbit coupling also becomes larger with increasing Z, which leads to the *high Z*-materials in the carbon group showing properties of topological insulators.

Such topological properties are predicted to open up numerous applications in spintronics [3, 4], for example, quantum spin hall effect transistors could be realized [5]. For the heavier elements in the carbon group, the described topological effects are predicted to be more significant, therefore the higher Z elements offer even more applications [6].

The first synthesis of stanene on Bi_2Te_3 in 2015 [7] laid the foundation for the synthesis of
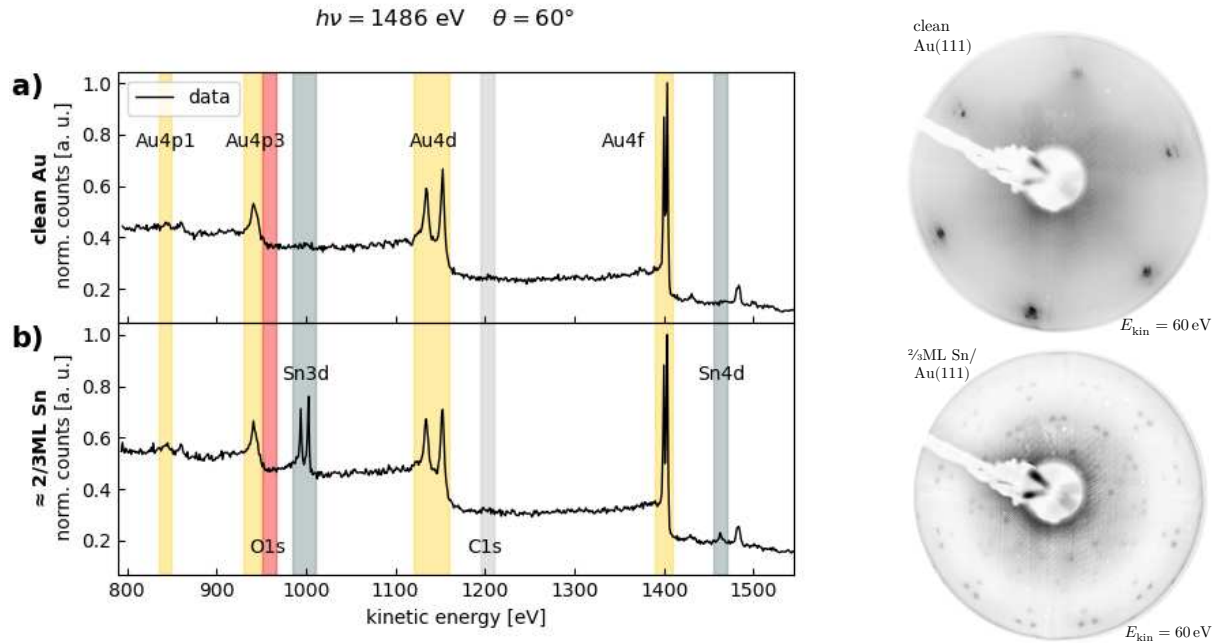
Figure 1: The XPS survey in **a)** as well as the sharp LEED pattern of the herringbone reconstruction indicate a clean surface. The XPS-survey in **b)** shows additional Sn signals after deposition of $\approx$ 2/3-ML Sn, leading to the sharp LEED pattern of the so-called x-phase as shown.

stanene on different substrates, such as Sb(111), InSb(111), PbTe(111), and Ag(111) [8–11].

Despite extraordinary electronic properties which were found, such as an exceptionally high Fermi velocity for Sn on Au(111) which is even an order of magnitude higher than predicted for free-standing stanene [12], no evidence for topological properties was found. However, in 2018 the preparation of ultraflat stanene on Cu(111) with a topological bandgap of $\Delta E = 0.3\,\text{eV}$ succeeded [13], which is seen as a milestone in the research of 2D topological devices.

As already evident from the examples above, the surface and interface structure of low-dimensional materials often influences their electronic properties. We therefore focus on the structural and chemical analysis of the Sn/Au(111) interface. Here, we report a structural and chemical investigation of 2/3-ML Sn on Au(111) at room temperature by means of low-energy electron diffration (LEED) and photoelectron spectroscopy (XPS).

Firstly, the Au(111)-substrate is prepared by cycles of Argon-sputtering at $E_{\text{Ar+}} = 1000\,\text{eV}$ and annealing to $T \approx 950\,\text{K}$. The preparation of the sample as well as all measurements are conducted at the UHV-endstation at beamline 11 at DELTA with a base pressure of $p \leq 6 \times 10^{-11}\,\text{mbar}$.

To check the cleanness and reconstruction of the surface LEED and XPS measurements are performed. The sharp LEED-spots of the so-called herringbone reconstruction of Au(111), shown in figure 1, indicate the successful preparation of the surface. Additionally, the XPS measurements as shown in figure 1a) do not reveal any contamination with chemical residues on the surface. Thereafter, the two-dimensional Sn-films were prepared by physical vapor deposition (PVD) on the Au(111) surface using an electron beam evaporator. The deposited film thickness was estimated to be about 2/3 ML using a quartz crystal microbalance. No further annealing was performed for the structural reconstruction investigated here. The XPS survey measurement in figure 1b) shows additional signals caused by the adsorbed Sn, but still does not show further contamination by residuals. The LEED-pattern shown in figure 1b) shows sharp spots, arranged in a $\begin{pmatrix} 2,1 & -4,2 \\ 3,8 & 0 \end{pmatrix}$-superstructure, also known as the x-phase [12, 14].

In addition, high-resolution XPS measurements were performed, as shown in figure 2. The best
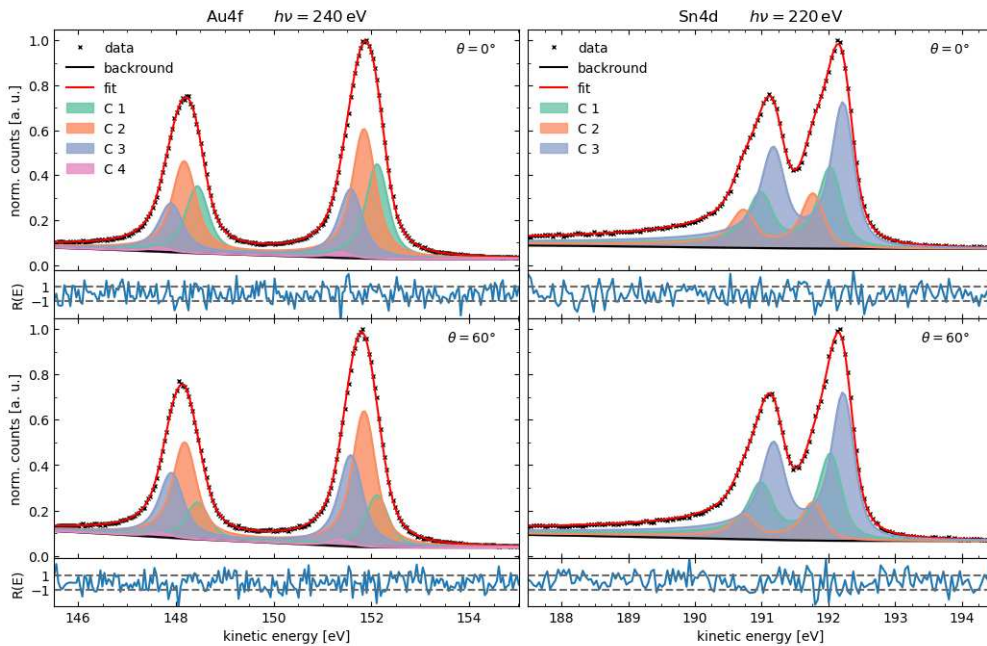
Figure 2: The displayed XP spectra were used to determine the different chemical environments of the Sn atoms arranged in the x-phase.

fit of the Au $4f$ orbital was achieved with four components. Thereby, $C1$ is identified as the Au bulk signal and the small $C4$ component is associated with an AuSn alloy, while the $C2$ and $C3$ components are associated with a chain- and honeycomb-like arrangement of Sn atoms on the surface, in agreement with the literature [14]. For the Sn $4d$-signal, component $C2$ is assigned to the AuSn alloy, and components $C1$ and $C3$ are associated with a chain and honeycomb arrangement of the Sn atoms at the surface, in agreement with the literature [14].

For further insights, a large number of different sub-monolayer thicknesses have already been investigated by XPS. In order to gain a detailed understanding of the structure formation of Sn on Au(111), these data are currently being analyzed. Further, small-step variations of the layer thickness will eventually provide an understanding of the structural evolution of sub-monolayer Sn on Au(111) both at room temperature and at elevated substrate temperatures.

References

[1] T. Wehling, A. Black-Schaffer, and A. Balatsky, Adv. Phys. **63**, 1 (2014), arXiv:1405.5774 .

[2] A. Molle, J. Goldberger, M. Houssa, Y. Xu, S.-C. C. Zhang, and D. Akinwande, Nat. Mater. **16**, 163 (2017).

[3] C.-C. Liu, H. Jiang, and Y. Yao, Phys. Rev. B **84**, 195430 (2011), arXiv:1108.2933 .

[4] M. Ezawa, in *2015 IEEE 15th Int. Conf. Nanotechnol.*, 4 (IEEE, 2015) pp. 604–608.

[5] T. Jungwirth, J. Wunderlich, and K. Olejník, Nat. Mater. **11**, 382 (2012).

[6] I. Gablech, J. Pekárek, J. Klempa, V. Svatoš, A. Sajedi-Moghaddam, P. Neužil, and M. Pumera, Trends Anal. Chem. **105**, 251 (2018).

[7] F. Zhu, W.-j. Chen, Y. Xu, C.-l. Gao, D.-d. Guan, C. Liu, D. Qian, S.-C. Zhang, and J.-f. Jia, Nat. Mater. **14**, 1020 (2015), arXiv:1506.01601 .

[8] J. Gou, L. Kong, H. Li, Q. Zhong, W. Li, P. Cheng, L. Chen, and K. Wu, Phys. Rev. Mater. **1**, 054004 (2017).

[9] C.-Z. Xu, Y.-H. Chan, P. Chen, X. Wang, D. Flötotto, J. A. Hlevyack, G. Bian, S.-K. Mo, M.-Y. Chou, and T.-C. Chiang, Phys. Rev. B **97**, 035122 (2017), arXiv:1711.08523 .

[10] Y. Zang, T. Jiang, Y. Gong, Z. Guan, C. Liu, M. Liao, K. Zhu, Z. Li, L. Wang, W. Li, C. Song, D. Zhang, Y. Xu, K. He, X. Ma, S. Zhang, and Q. Xue, Adv. Funct. Mater. **28**, 1802723 (2018).

[11] J. Yuhara, Y. Fujii, K. Nishino, N. Isobe, M. Nakatake, L. Xian, A. Rubio, and G. Le Lay, 2D Mater. **5**, 025002 (2018).

[12] M. Maniraj, B. Stadtmüller, D. Jungkenn, M. Düvel, S. Emmerich, W. Shi, J. Stöckl, L. Lyu, J. Kollamana, Z. Wei, A. Jurenkow, S. Jakobs, B. Yan, S. Steil, M. Cinchetti, S. Mathias, and M. Aeschlimann, Commun. Phys. **2**, 12 (2019).

[13] J. Deng, B. Xia, X. Ma, H. Chen, H. Shan, X. Zhai, B. Li, A. Zhao, Y. Xu, W. Duan, S.-C. Zhang, B. Wang, and J. G. Hou, Nat. Mater. **17**, 1081 (2018).

[14] W. Pang, K. Nishino, T. Ogikubo, M. Araidai, M. Nakatake, G. Le Lay, and J. Yuhara, Appl. Surf. Sci. **517**, 146224 (2020).

Structural determination of germanium formations on silver at low coverages by means of XPS and XPD

L. Kesper[1,2,*]**, M. Schmitz**[1,2]**, J. A. Hochhaus**[1,2]**, M. G. H. Schulte**[1,2]**, U. Berges**[1,2]**, and C. Westphal**[1,2]

[1] Experimentelle Physik I - Technische Universität Dortmund, Otto-Hahn-Str. 4a, D-44227 Dortmund
[2] DELTA - Technische Universität Dortmund, Maria-Goeppert-Mayer-Str. 2, D-44227 Dortmund
* corresponding author: lukas.kesper@tu-dortmund.de

The discovery of graphene in 2004 as the first experimental synthesis of a 2D-material was a major breakthrough in solid state physics. A handful of further elemental 2D-materials, so-called Xenes, were discovered in the following years [1–3]. Especially group IV elements show outstanding electronic properties in their two-dimensional structure, like Dirac-characteristic band structures, and large thermal and electrical conductivity due to the electrons' ultra-high Fermi velocity [4, 5]. Additionally, germanene belongs to the *high Z*-materials, which commonly show a strong spin-orbit interaction, that might be utilized for spintronic devices [6]. In the case of germanene, it turned out that the electronic structure is directly influenced by the structural properties of the material, like the buckling, which strongly depends on the carrier substrates [4, 7]. Its massive potential for the development of new technological devices can even be expanded by the possibility of the systematic tuning of certain material properties, such as the bandgap. For this purpose it is crucial to consolidate and extend the understanding of the structural formation of 2D-materials.

In this report, we present an abstract of our investigations on the structural evolution of low-dimensional germanium formations on silver. Therefore, two phases at low coverages of
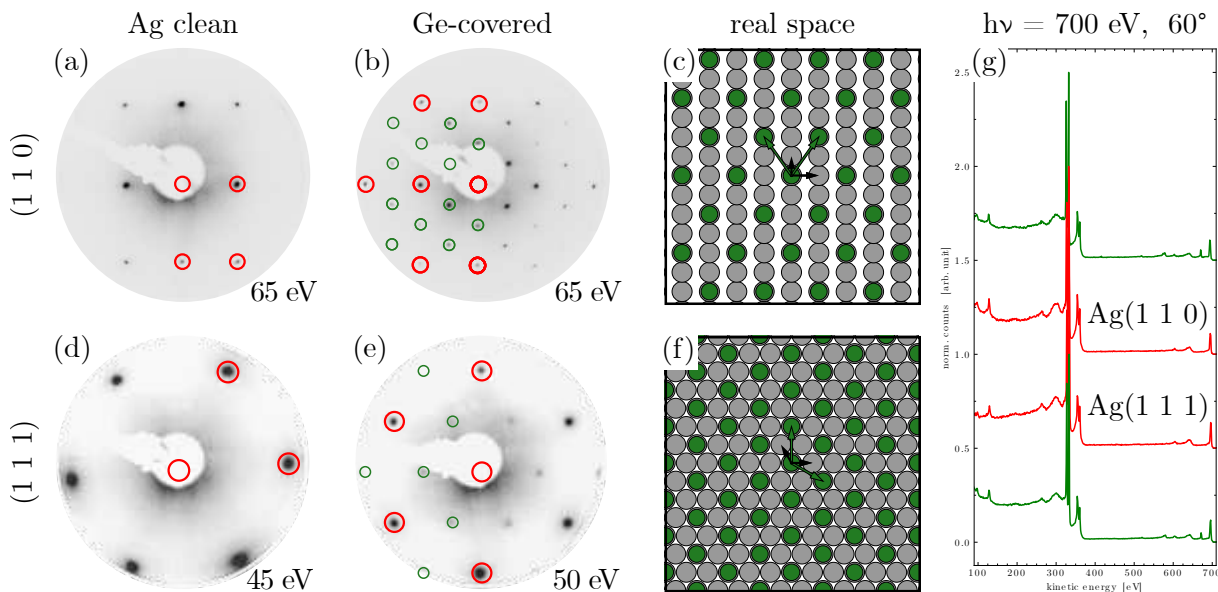
Figure 1: LEED-patterns of (a) clean Ag(1 1 0) and (d) Ag(1 1 1), as well as of the corresponding germanium covered surfaces (b) and (e), respectively. The real space illustrations (c) and (f) are concluded from the LEED spot positions in the experimental patterns. Subfigure (g) displays XPS survey spectra of the Ge/Ag-systems (green) and of the corresponding substrate (red).

germanium on Ag(1 1 0) and Ag(1 1 1) will be analysed by using low-energy electron diffraction (LEED), photoelectron spectroscopy (XPS), and photoelectron diffraction (XPD) measurements, performed at beamline 11 (BL11) at DELTA. Previous studies of these systems have reported the formation of germanium nanoribbons on Ag(1 1 0) and two-dimensional germanene

on Ag(1 1 1) [8, 9]. Here we will discuss the initial crystalline phases of each structural evolution.

Figure 1(a) and figure 1(d) show LEED-patterns of the clean Ag(1 1 0) and Ag(1 1 1) surfaces, after several preparation cycles of sputtering and annealing. The patterns were obtained with primary electron energies of $E_{kin} = 65\,eV$ and $E_{kin} = 45\,eV$ revealing the first brillouin zone of the sample, as marked by the red circles. Besides the long-range order of the crystal, also the cleanliness was checked by XPS survey spectra, as displayed in figure 1(g). Both red data curves represent the chemical composition of the clean Ag(1 1 0) (top) and Ag(1 1 1) (bottom) sample. After the deposition of 0.5 ML Ge on Ag(1 1 0) by means of physical vapor deposition the LEED-pattern in figure 1(a) turns into (b), which shows sharp spots of a $c(4 \times 2)$ reconstruction. The additional reflection spots of the adsorbate are highlighted with green circles, supporting observations from similar studies [8, 10]. A corresponding real space illustration, given in figure 1(c) was made by using *LEEDpat* [11]. The same procedure was applied to the system of 0.25 ML Ge on Ag(1 1 1) forming a $p(\sqrt{3} \times \sqrt{3})\mathrm{R}30°$, as identified from figure 1(e) and (f).
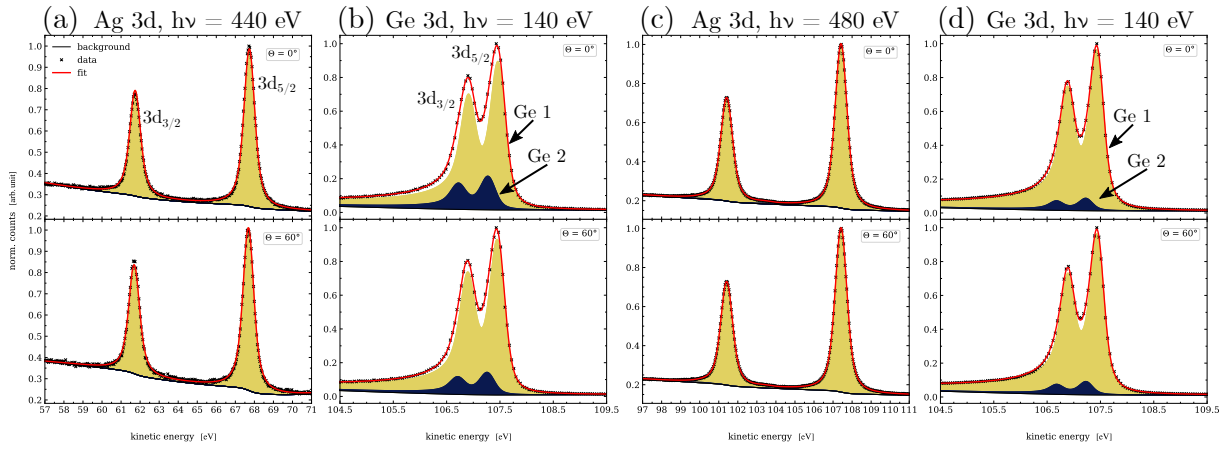
Figure 2: High resolution spectra of the Ag 3d and Ge 3d core-levels of (a)-(b) 0.5 ML Ge on Ag(1 1 0) and (c)-(d) 0.25 ML Ge on Ag(1 1 1).

High energy resolution XPS spectra of the Ag 3d and the Ge 3d core-level were taken for both sample systems using soft x-ray radiation from the undulator U55 at BL11. Figure 2(a) und (b) show the respective core-level spectra of the Ge/Ag(1 1 0) system. All XPS spectra were fitted using the *UNIFIT 2022* software [12], which applies a Shirley and Tougaard background subtraction as well as Voigt profiles and convoluted profiles of Doniach Sunjic und Gaussian to the peaks. Since only one single component can be identified in the 3d-signal of the Ag-substrate, we assume that the germanium layer is only weakly bonded to the substrate by Van-der-Waals forces. The second component that was found in the corresponding Ge 3d signal can be attributed to a group of atoms in a slightly different chemical environment. Due to a decrease of component Ge 2 for higher emission angles, these atoms might be located closer to the interface than the emitter atoms of component Ge 1. The core-level spectra of the Ge/Ag(1 1 1) system, presented in figure 2(c) and (d) reveal the same behaviour as no strong interaction between substrate and adsorbate can be supposed. The Ge 3d signal in figure 2(d) also shows a minor second component, which is more likely to be assigned to increasingly growing parts of a next phase at higher coverages.

For the discussion of a structural model for both systems, XPD measurements have been performed. For this purpose, 7200 single XPS spectra were recorded over the upper hemisphere of a sample. The integrated spectra lead to the experimental intensity plots in figure 3(a) and (c). To determine the structure of the investigated sample system simulated XPD-patterns of test structures were generated using the multiple scattering package *EDAC* [13]. The agreement between experiment and simulation is evaluated by the R-factor, which is expected to be zero for a perfect match. Structure models for each sample system could be found that fulfilled
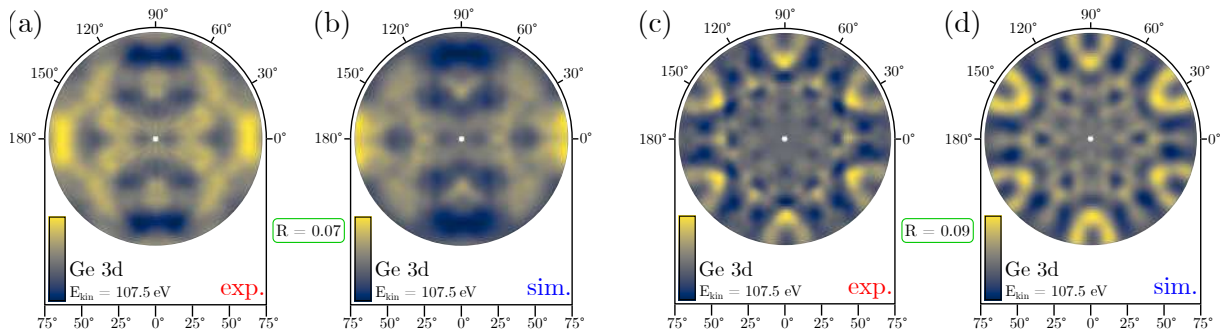
Figure 3: Experimental and simulated XPD patterns of the Ge 3d core-level, obtained with a photon energy of $h\nu = 140\,\text{eV}$, (a)-(b) for the Ge/Ag(1 1 0) and the (c)-(d) Ge/Ag(1 1 1) system.

the periodicity obtained by LEED in figure 1 and showed poor interaction with the substrate as concluded from our XPS results in figure 2. Additionally, both structural models are in very good agreement with those proposed in literature [8, 10, 14, 15], while the corresponding simulations show a high consistency with the experiment, as indicated by R-factors of R = 0.07 for Ge/Ag(1 1 0) and R = 0.09 for Ge/Ag(1 1 1). A more detailed discussion for the Ge/Ag(1 1 0) system will be available, soon [16].

References

[1] P. Vogt, P. De Padova, C. Quaresima, J. Avila, E. Frantzeskakis, M. C. Asensio, A. Resta, B. Ealet, and G. Le Lay, Physical Review Letters **108**, 155501 (2012).

[2] M. E. Dávila, L. Xian, S. Cahangirov, A. Rubio, and G. L. Lay, New Journal of Physics **16**, 095002 (2014).

[3] J. Yuhara and G. L. Lay, Japanese Journal of Applied Physics **59**, SN0801 (2020).

[4] A. Molle, J. Goldberger, M. Houssa, Y. Xu, S.-C. Zhang, and D. Akinwande, Nature Materials **16**, 163 (2017).

[5] S. Balendhran, S. Walia, H. Nili, S. Sriram, and M. Bhaskaran, Small **11**, 640 (2015).

[6] Y. Wang, J. Zheng, Z. Ni, R. Fei, Q. Liu, R. Quhe, C. Xu, J. Zhou, Z. Gao, and J. Lu, Nano **7**, 1250037 (2012).

[7] N. Gao, H. Liu, S. Zhou, Y. Bai, and J. Zhao, The Journal of Physical Chemistry C **121**, 5123 (2017).

[8] J. Yuhara, H. Shimazu, M. Kobayashi, A. Ohta, S. Miyazaki, S. i. Takakura, M. Nakatake, and G. Le Lay, Applied Surface Science **550**, 149236 (2021).

[9] C.-H. Lin, A. Huang, W. W. Pai, W.-C. Chen, T.-Y. Chen, T.-R. Chang, R. Yukawa, C.-M. Cheng, C.-Y. Mou, I. Matsuda, T.-C. Chiang, H.-T. Jeng, and S.-J. Tang, Physical Review Materials **2**, 024003 (2018).

[10] C. Léandri, H. Oughaddou, J. Gay, B. Aufray, G. Le Lay, J. Bibérian, A. Ranguis, O. Bunk, and R. Johnson, Surface Science **573**, L369 (2004).

[11] K. E. Hermann and M. A. Van Hove, *LEEDpat, Version 4.2*, Fritz-Haber-Institut / Hong Kong Baptist University, Berlin / Hong Kong (2014).

[12] R. Hesse and R. Denecke, Surface and Interface Analysis **43**, 1514 (2011).

[13] F. J. García de Abajo, M. A. Van Hove, and C. S. Fadley, Physical Review B **63**, 075404 (2001).

[14] E. Golias, E. Xenogiannopoulou, D. Tsoutsou, P. Tsipas, S. A. Giamini, and A. Dimoulas, Physical Review B **88**, 075403 (2013).

[15] Y. Liu, J. Zhuang, C. Liu, J. Wang, X. Xu, Z. Li, J. Zhong, and Y. Du, The Journal of Physical Chemistry C **121**, 16754 (2017).

[16] L. Kesper, M. Schmitz, M. G. H. Schulte, U. Berges, and C. Westphal, Applied Nanoscience, *submitted*.

X-ray photoelectron spectroscopy analysis of the chemical states in erbium- and gadolinium-containing amorphous carbon films

Wolfgang Tillmann[1], Nelson Filipe Lopes Dias[1,*], Dominic Stangier[1], Jasper Berndt[2], Stephan Klemme[2], Lukas Kesper[3,4], Ulf Berges[3,4], Carsten Westphal[3,4], Carl Arne Thomann[5], Jörg Debus[5]

[1] Institute of Materials Engineering, TU Dortmund University, Leonhard-Euler-Str. 2, D-44227 Dortmund
[2] Institut für Mineralogie, Westfälische Wilhelms-Universität Münster, Corrensstrasse 24, D-48149 Münster
[3] Experimental Physics 1, TU Dortmund University, Otto-Hahn-Str. 4a, D-44227 Dortmund
[4] DELTA, TU Dortmund University, Maria-Goeppert-Mayer-Str. 2, D-44221 Dortmund
[5] Experimental Physics 2, TU Dortmund University, Otto-Hahn-Str. 4a, D-44227 Dortmund

*corresponding author: filipe.dias@tu-dortmund.de

Amorphous carbon (a-C) films consist of a metastable disordered network of C bonds in sp²- and sp³-coordinated configuration [1]. By adding a further element to a-C, the film properties can be further tailored [2]. In this regard, the rare-earth elements Er and Gd are promising modification elements due to their unique physicochemical properties. Er-containing a-C (a-C:Er) is capable of showing photoluminescence from Er^{3+} ions at an emission wavelength of $\lambda = 1.54\ \mu m$ [3,4]. Gd-containing a-C (a-C:Gd) exhibits a large negative magnetoresistance at low temperatures and high magnetic fields due to the half-filled f-electron shell [5–7]. Previous studies on a-C:Er and a-C:Gd films were related to the physicochemical properties, whereas the structural and mechanical properties were barely addressed. In a magnetron sputtering process, a-C:Er and a-C:Gd films were grown with Er and Gd concentrations up to 5 at.-% and 4.8 at.-%, respectively. X-ray photoelectron spectroscopy (XPS) analysis provides a fundamental understanding of the influences of Er or Gd addition on the chemical state of the elements present in the films. Insights on the bonding composition of a-C:Er and a-C:Gd are crucial to derive their effects on the mechanical properties of the films.
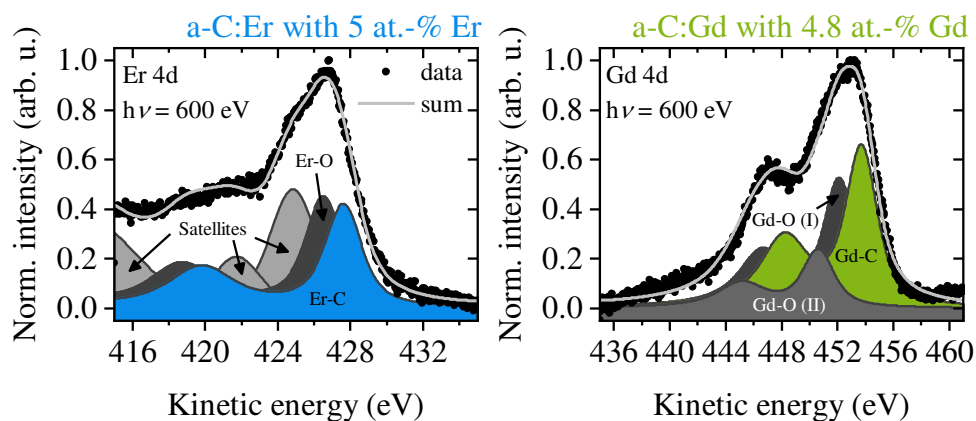
Figure 1: High-resolution XPS of the Er 4d and Gd 4d orbitals of the a-C:Er and a-C:Gd films with the highest contents of Er and Gd [8].

Figure 1 shows the high-resolution XPS spectra of the Er 4d and Gd 4d of a-C:Er and a-C:Gd with the highest amount of the respective rare-earth element. The decomposition into their single components is also displayed. A spin-orbit separation into $4d_{5/2}$ and $4d_{3/2}$ peaks with energy separation of $E_{SOC} = 7.8$ eV for the Er 4d and $E_{SOC} = 5.5$ eV for the Gd 4d is identified. The Er 4d core-level is composed of Er-C and Er-O components (due to the high chemical affinity of Er to O) as well as of three satellite peaks. The Gd 4d signal consists of Gd-C as well as of two oxide components Gd-O (I) and Gd-O (II) (due to the high chemical affinity of Gd to O).
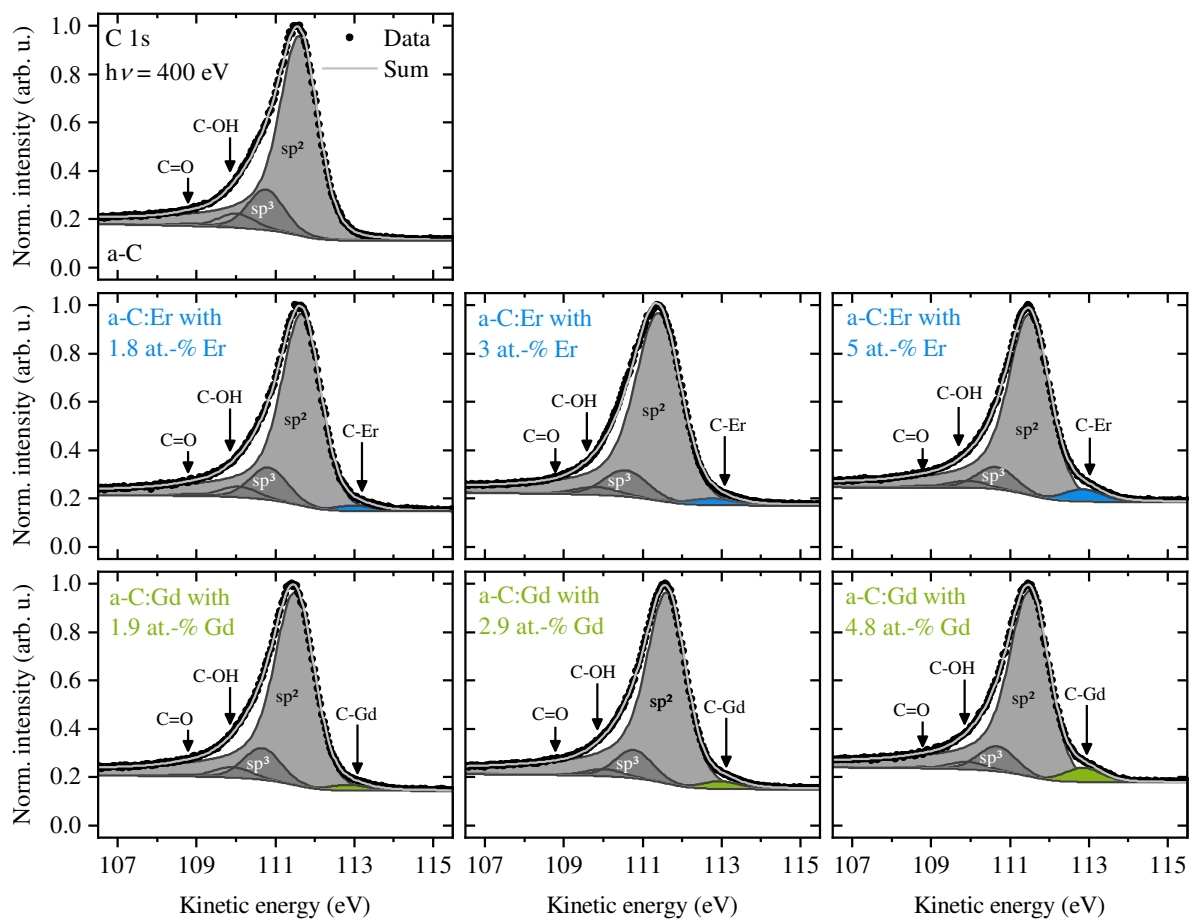
Figure 2: High-resolution XPS of the C 1s orbital of the a-C:Er and a-C:Gd films [8].

In addition, the effects of the Er and Gd addition on the chemical state of C were derived from the high-resolution XPS of the C 1s, see Figure 2. The C 1s spectrum of the non-modified a-C film is composed of the two main components sp²-coordinated C=C and sp³-coordinated C-C as well as of the minor oxide contributions C-OH and C=O. For the a-C:Er and a-C:Gd films, it is noted that a new chemical state arises in the C 1s signal with a chemical shift to higher kinetic energies, indicating the formation of either C-Er or C-Gd components. With increasing Er and Gd concentration, the amount of C-Er and C-Gd contributions raise from 1.8% to 4.3% for a-C:Er and from 1.8% to 4.6% for a-C:Gd (calculated from the peak area). By contrast, the

fraction of sp³-configured C-C components is reduced from 12.4% (non-modified a-C) to 7.9% for a-C:Er and to 8.1% for a-C:Gd with the highest Er and Gd concentrations.

With the obtained findings from the XPS analyses, the influence of the changes of the chemical states on the structural characteristics of the amorphous network and mechanical properties were further analyzed. Complementary investigations by Raman spectroscopy identified an increase in number and size of sp² clusters in the disordered network. As a consequence of these structural changes, the hardness linearly decreased from (21.7 ± 1.6) GPa (non-modified a-C) to (16.7 ± 0.9) GPa for a-C:Er and (14.8 ± 0.9) GPa for a-C:Gd with increasing Er and Gd concentration. A similar tendency was also noted for the elastic modulus. This is due to the linear dependence between the sp³ content and the mechanical properties [1]. A more detailed analysis of the effects of Er and Gd on the structural evolution and mechanical properties of a-C:Er and a-C:Gd will be available soon [8].

Presentation to a scientific audience: The study entitled "*Rare-earth modified amorphous carbon: effects of erbium and gadolinium on the structural evolution and mechanical properties*" was presented at the *31ˢᵗ International Conference on Diamond and Carbon Materials*, which took place virtually on 6-9 September 2021. The speaker Mr. Lopes Dias has been awarded with the Young Scholar Silver Award 2021 by the conference committee for his oral talk and poster presentation.

References

[1]   B. Schultrich, Tetrahedrally Bonded Amorphous Carbon Films I: Basics, Structure and Preparation, Springer Berlin Heidelberg, Berlin, Heidelberg, 2018.

[2]   J.C. Sánchez-López, A. Fernández, Doping and Alloying Effects on DLC Coatings, in: C. Donnet, A. Erdemir (Eds.), Tribology of Diamond-like Carbon Films: Fundamentals and Applications, Springer Science + Business Media LLC, Boston, MA, 2008, pp. 311–338.

[3]   A.M. Baranov, V.V. Sleptsov, A.A. Nefedov, A.E. Varfolomeev, S.S. Fanchenko, L. Calliari, G. Speranza, M. Ferrari, A. Chiasera, Erbium Photoluminescence in Hydrogenated Amorphous Carbon, Physica Status Solidi B **234** (2002) R1-R3. https://doi.org/10.1002/1521-3951(200211)234:2<R1:AID-PSSB99991>3.0.CO;2-6.

[4]   G. Speranza, L. Calliari, M. Ferrari, A. Chiasera, K. Tran Ngoc, A.M. Baranov, V.V. Sleptsov, A.A. Nefedov, A.E. Varfolomeev, S.S. Fanchenko, Erbium-doped thin amorphous carbon films prepared by mixed CVD sputtering, Applied Surface Science **238** (2004) 117–120. https://doi.org/10.1016/j.apsusc.2004.05.191.

[5]   L. Zeng, E. Helgren, H. Zutz, C. Ronning, F. Hellman, Magnetic Rare Earth (Gd) Implanted Tetrahedral Amorphous Carbon (ta- C), MRS Proceedings **941** (2006) 822. https://doi.org/10.1557/PROC-0941-Q08-22.

[6]   L. Zeng, E. Helgren, F. Hellman, R. Islam, D.J. Smith, J.W. Ager, Microstructure, magnetotransport, and magnetic properties of Gd-doped amorphous carbon, Physical Review B **75** (2007) 27401. https://doi.org/10.1103/PhysRevB.75.235450.

[7]   L. Zeng, H. Zutz, F. Hellman, E. Helgren, J.W. Ager, C. Ronning, Magnetoelectronic properties of Gd-implanted tetrahedral amorphous carbon, Physical Review B **84** (2011) 134419. https://doi.org/10.1103/PhysRevB.84.134419.

[8]   W. Tillmann, N.F. Lopes Dias, D. Stangier, J. Berndt, S. Klemme, L. Kesper, U. Berges, C. Westphal, C.A. Thomann, J. Debus, Rare-earth modified amorphous carbon films: effects of erbium and gadolinium on the structural evolution and mechanical properties, submitted on 25.10.2021.

Chemical investigation a of graphene/cobalt/platinum multilayer system on silicon carbide

P. Weinert[1,2,*], L. Kesper[1,2], J. Hochhaus[1,2], U. Berges[1,2], C. Westphal[1,2]

[1] Experimentelle Physik I - Technische Universität Dortmund, Otto-Hahn-Str. 4a, D-44227 Dortmund

[2] DELTA - Technische Universität Dortmund, Maria-Goeppert-Mayer-Str. 2, D-44227 Dortmund

* corresponding author: philipp.weinert@tu-dortmund.de

In this research the chemical bindings in a graphene/cobalt/platinum system on a silicon carbide (SiC) substrate are investigated by means of XPS. Prior to this study, the system has been investigated by means of LEED and PEEM to determine the preparation parameters. After the XPS measurements, its magnetic properties were determined during a beam-time at BESSY II by X-PEEM in combination with XMCD. Due to the magnetic exchange interaction at the interfaces, perpendicular magnetic anisotropy (PMA) exists in the Co-film of both the G/Co- and the Co/Pt-system [1, 2], as well as in the combined G/Co/Pt-system on a MgO(111) substrate PMA [3]. This makes the system highly interesting for future spintronic devices. Unfortunately, metal and metal oxide substrates often lead to multiple graphene domains, which impair its electronic and magnetic properties and magnetic structure formation [4]. Since SiC as a substrate allows the preparation of graphene with just one domain over microscopically large surfaces [5], it is a promising prospect to improve the magnetic properties of the system. However, in a G/Co system on SiC no PMA was found [6], most probably due to the formation of cobalt silicides. The added Pt-layer between Co and SiC serves to prevent this formation.

Sample preparation can be divided into three steps. After each step the sample was investigated by XPS.

First, the $(6\sqrt{3} \times 6\sqrt{3})$R30° surface reconstruction of SiC (buffer layer) has been grown homogeneously on SiC over large areas [5]. This surface serves as a precursor for monolayer graphene formation upon intercalation. Figure 1a shows the corresponding XPS spectra of the C1 s signal. The preparation method causes small strips of monolayer graphene on top of the buffer layer at the step edges of the SiC. The corresponding component (G) is located between the buffer layer components (S1 and S2) and the substrate component (SiC) [7].

By intercalating Pt the bonds between the buffer layer to SiC are released. This way the buffer layer becomes quasi free standing graphene [8]. As a result, and as shown in Figure 1b, the signals of the buffer layer components vanished in the XPS-spectrum, while the graphene signal increases. Noteworthy, the corresponding Pt 4f signal, as shown in figure 2 consists of four components. Three of them belong to Pt-Si compounds, which might indicate that Pt saturates the free silicon bonds.

The third step of the preparation consists of the deposition and intercalation of Co. The XPS spectra before and after the interaction only change in intensity, but not in shape. This finding proves that the Pt-layer prevents the formation of Co silicides. ARXPS has been used in order to prove the intercalation of Co. A change in signal intensity indicates the change in order of the graphene and the Co-layer.

In summary, the formation of platinum silicides has been investigated and three components were identified. Furthermore, the desired prevention of Co-Si components has been achieved. After the XPS measurements X-PEEM measurements were performed to investigate the magnetic structure of the G/Co/Pt-system. For the image shown in Figure 3 two

X-PEEM images were combined, one taken before and one after sample rotation by 90°. Such a combination reveals the in-plane magnetization of the sample surface. As a first surprising result, we observed a rather large domain, plotted in blue. Furthermore, in the lower left part of the image a spin vortex is marked by a black circle. Both of these features might be interesting for the application in devices. In a next step, the out of plane component will be analyzed, in order to reveal the full magnetic structure.
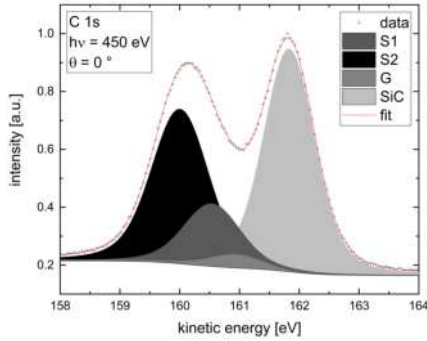
(a) XPS spectrum of the carbon 1s signal of buffer layer and small amounts of monolayer graphene grown on silicon carbide.
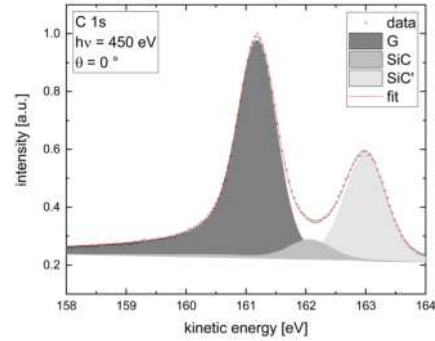
(b) XPS spectrum of the carbon 1s signal of monolayer graphene on silicon carbide after the intercalation of 3 Å Pt.
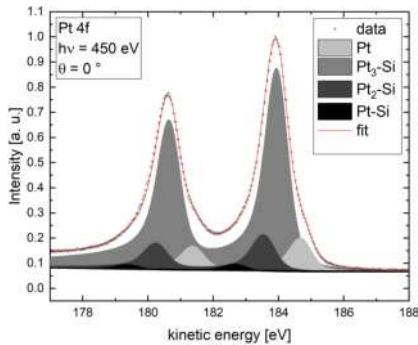
Figure 2: XPS spectrum of the platinum 4f signal of an Pt-layer intercalated between G and SiC. Three silicide components are present, what indicates that the Pt saturate the free silicon bonds.
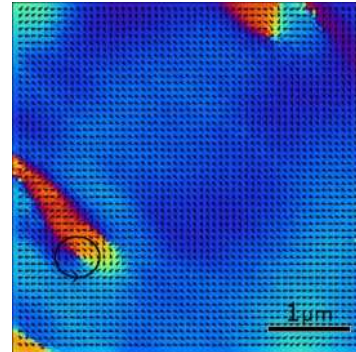
Figure 3: Combined X-PEEM image with magnetic contrast of the in plane component (small black arrows). The image shows one particularly large domain (blue area) and a spin vortex (black circle).

Acknowledgement

References

[1] G. S. Grebenyuka et al., Phys. Solid State **61**, 7 (2019).
[2] C. Xia et al., Carbon **79**, 1 (2014).
[3] F. Ajejas et al. Nano Lett. **18**, 9 (2018).
[4] O. V. Yazyev, S. G. Louie, Phys Rev. B **81**, 195420 (2010).
[5] W. A. de Heer et al., Proc. Natl. Acad. Sci. USA **108**, 16900 (2011).
[6] R. Hönig et al., Nanotechnology **30**, 2 (2019).
[7] C. Riedl et al., J. Phys. D: Appl. Phys. **43**, 37 (2010).
[8] S. Forti et al., Phys. Rev. B **84**, 125449 (2011).

X-ray Scattering

Structure formation in liquid linear monohydroxy-alcohols

A. Faulstich, J. Bolle, C. Albers, J. Latarius, K. Lehninger, R. Sakrowski, G. Surmeier, M. Paulus, M. Tolan, and C. Sternemann

Fakultät Physik/DELTA, Technische Universität Dortmund, Maria-Goeppert-Mayer-Str. 2, 44227 Dortmund, Germany

Linear monohydroxy-alcohols (MAs) exhibit a peculiar heterogeneity on a mesoscopic length scale due to the formation of transient supramolecular assemblies consisting of a charged core of hydrogen-bonded hydroxyl groups surrounded by their flexible alkyl tails [1]. It is the interplay between hydrogen-bonding and steric hindrance implied by the alkyl tails which controls the type of microstructure ranging from dominating contribution of small and tight clusters in case of small alkyl tails to larger linear and linear branched entities with increasing chain length [2]. This microstructure was found to be highly sensitive to changes in temperature [3] and pressure [4] as well as branching ratio in case of branched MAs [3].

In this study we investigated the temperature and pressure dependence of the structure formation in a series of linear MAs by systematic variation of the chain length from methanol to 1-undecanol. The measurements were performed at the setup for small-angle and wide-angle X-ray scattering at beamline BL2 of the DELTA synchrotron radiation source. We used an incident energy of 12 keV with a bandwidth of 10^{-3} and beam size of 1x1 mm². Diffraction data were collected by a MAR345 image plate detector. For temperature measurements, the samples were filled into borosilicate capillaries and closed with glue avoiding contact between glue and the alcohols. The temperature was varied by a liquid nitrogen cryostream cooler in the range between 230 K and 380 K depending on the melting and boiling points of the respective MAs. The high pressure experiments were conducted between 50 bar and 4000 bar at room temperature exploiting a dedicated high pressure cell [5]. Here, the samples were prepared within sample holders equipped with Kapton windows in order to ensure penetration of X-rays and hydrostatic pressure transfer.

Typical diffraction patterns of a temperature series for 1-nonanol are presented in figure 1 (left). The first sharp diffraction peak, indicative for the atom-atom (molecule-molecule) contact in liquids, can be observed at a wave vector transfer of about 14.2 nm⁻¹ and is due to correlations between methylene/methyl groups. The so-called pre-peak, indicative for supramolecular structure formation in polar liquids, appears at about 3.8 nm⁻¹ of 1-nonanol. Its variation in position and intensity with temperature or pressure provides insight into the change of transient cluster formation. The analysis of the relative change of the pre-peak position $q(T)$ with respect to its value determined at highest temperature $q(T_{max})$ is shown in figure 1 (right) and can be assigned to the average size of transient clusters, i.e. with increasing $q(T)$ the size of supramolecular entities becomes smaller either due to
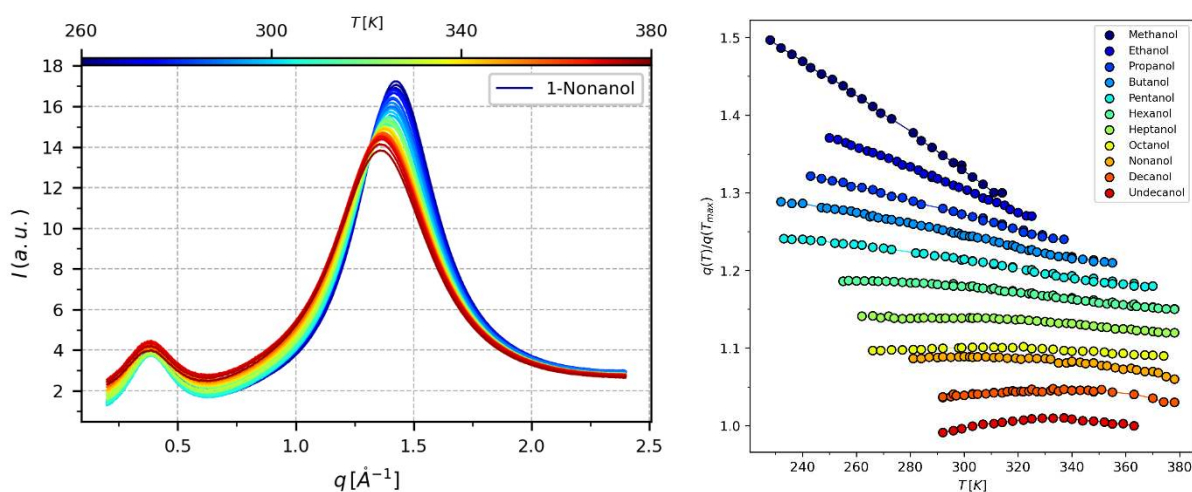
Figure 1: Diffraction patterns of 1-nonanol measured for different temperatures (left); relative change of pre-peak position with temperature (right).

compression and/or change in cluster architecture. Our results indicate a clear dependency on chain length and reveal a structural crossover at low temperatures for MAs with larger alkyl tails. While the change in pre-peak position of methanol to 1-propanol is in line with the increase in density pointing towards a compression of tight and small clusters, for 1-heptanol to 1-undecanol we observe an increase in size (decrease in q position) of supramolecular objects with decreasing temperature. Latter must be assigned to a significant change in cluster type indicating a formation of larger linear or linear branched clusters with increasing chain length.

Figure 2: Relative change of pre-peak position with pressure.

The change in pre-peak position with variation of pressure is shown in figure 2. The pre-peak vanishes with pressure for the short-chain MAs methanol to 1-propanol. For higher MAs crystallization is observed at pressures of 2250 bar, 2000 bar, and 750 bar for 1-octanol, 1-nonanol, and 1-decanol, respectively. All MAs exhibit a similar pressure dependence of the pre-peak position that is characterized by a saturation at higher pressures. This behavior can be interpreted as strong suppression of formation of larger supramolecular arrangements with pressure and predominant occurrence of monomers and small clusters accompanied by break-up of ring-like structures in agreement with observations via dielectric spectroscopy [6].

In a next step these results will be confronted with predictions of cluster formation extracted from molecular dynamics simulations.

References

[1] R. Böhmer, C. Gainaru, and R. Richert, Structure and dynamics of monohydroxy alcohols—milestones towards their microscopic understanding, 100 years after Debye, Physics Reports 545, 125 (2014); [2] M. Požar, J. Bolle, C. Sternemann, and A. Perera, On the X-ray scattering pre-peak of linear mono-ols and the related microstructure from computer simulations, Journal of Physical Chemistry B 124, 8358 (2020); [3] J. Bolle, S.P. Bierwirth, M. Požar, A. Perera, M. Paulus, P. Münzner, C. Albers, S. Dogan, M. Elbers, R. Sakrowski, G. Surmeier, R. Böhmer, M. Tolan, and C. Sternemann, Isomeric effects in structure formation and dielectric dynamics of different octanols, Physical Chemistry Chemical Physics 23, 24211 (2021); [4] A. Mariani, P. Ballirano, F. Angiolari, R. Caminiti, and L. Gontrani, Does High Pressure Induce Structural Reorganization in Linear Alcohols? A Computational Answer ChemPhysChem 17, 3023 (2016); [5] C. Krywka, C. Sternemann, M. Paulus, M. Tolan, C. Royer, R. Winter, Effect of Osmolytes on Pressure-Induced Unfolding of Proteins: A High-Pressure SAXS Study, ChemPhysChem 9, 2809 (2008). [6] S. Pawlus, M. Wikarek, C. Gainaru, M. Paluch, and R. Böhmer, How do high pressures change the Debye process of 4-methyl-3-heptanol, Journal of Chemical Physics 139, 064501 (2013).

Acknowledgments

The study of radiation damage to proteins by small angle X-ray scattering

Clara Meiling Hua[1], Susanne Dogan[2], Michael Paulus[2]

[1] Fakultät Bio- und Chemieingenieurwesen, TU Dortmund, 44221 Dortmund, Germany

[2] Fakultät Physik/DELTA, TU Dortmund, 44221 Dortmund, Germany

Proteins make up a very large proportion of the organic substances in the human body. They have a wide range of functions, including acting as hormones, antibodies or enzymes, and are also responsible for signal transmission and the exchange of substances between cells. Many proteins obtain their specific function from the way their polypeptide chain is folded. Thus, misfolding or aggregation of proteins can lead to loss of function or, in the worst case, trigger diseases. Due to their diverse tasks in the human body, the study of protein structure and the associated function represents an extremely important branch of research in biology and medicine.

Proteins have a size in the nm range, which makes them suitable for small-angle X-ray scattering experiments. SAXS data contain information about size, shape and polydispersity as well as about protein-protein interactions. A problem in the investigation of biological material by synchrotron radiation is the generation of radiation damage, which can alter the proteins structurally as well as the protein-protein interactions. Radiation damage to proteins can occur after a very short time at modern radiation sources. To get an overview of the sensitivity of individual proteins to irradiation, the four different proteins ribonuclease A (RNase), lysozyme, hemoglobin and bovine serum albumin (BSA) were investigated. RNase (Sigma-Aldrich), is a globular protein responsible for the processing and degradation of RNA. RNase is 124 amino acids long, has four disulfide bridges, and has a molecular weight of 13.7 kDa. The isoelectric point (pI) is pH 9.45. Lysozyme (Sigma-Aldrich) is a globular protein, has four disulfide bridges, and has a pI of pH 11. Lysozyme is 129 amino acids long and has a molecular weight of 14.4 kDa. Hemoglobin (GenWay) is a globular protein complex that binds oxygen to transport it through the bloodstream. The pI of Hb is pH 7.4, and the molecular weight of the tetramer is 64 kDa. The globular protein BSA is derived from bovine blood serum (Sigma-Aldrich). The protein regulates the colloidosmotic pressure in the organism. BSA is 583 amino acids long and has a molecular weight of 66 kDa. A cysteinyl residue and 17 disulfide bridges stabilize the protein. The pI is pH 4.7. The stability of proteins is often tested by varying thermodynamic parameters such as temperature or pressure. In terms of temperature, denaturation of RNase A occurs at a temperature of 71 °C, of lysozyme at 68 °C, and of BSA at 57 °C. Denaturation of hemoglobin occurs between 60 °C and 68 °C. Thus, RNase A and lysozyme thus appear to be more stable than BSA or hemoglobin. This is also shown by the pressure induced denaturation, because it is triggered for RNase A at 500 MPa, for lysozyme at 686 MPa for BSA at 400 MPa and for deoxyhemoglobin, the oxygen-deficient form of hemoglobin, at 203 MPa.

The SAXS measurements were performed at the beamline BL2. The photon energy was 12 keV and the distance between the sample and the MAR345 detector was 1400 mm. The measurement time per frame was 600 s. The proteins were exposed to synchrotron radiation for several hours. The proteins were each prepared at a concentration of 5 mg/ml in different buffer solutions (20 mM). Care was taken to ensure that the pH value did not correspond to the isoelectric point of the protein in order to prevent aggregation of the proteins due to a lack of Coulomb repulsion. To determine the scattering background, measurements were also performed on pure buffer solutions. A measurement of silver behenate was also carried out to calibrate the set-up.
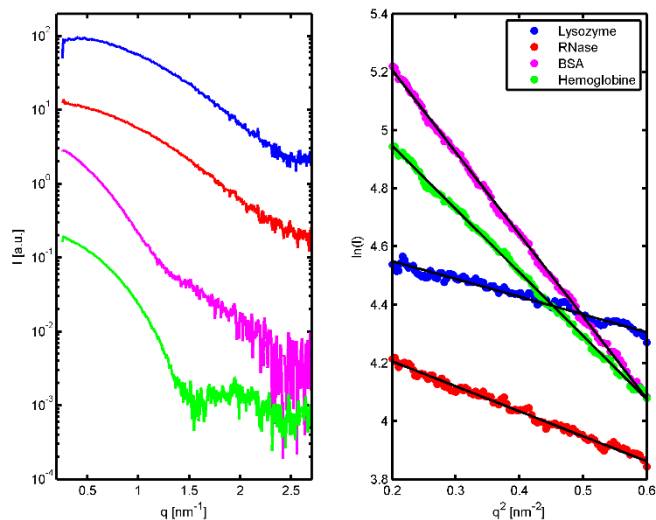
Figure 1: Left: SAXS data of different protein solutions with a concentration of 5 mg/ml. Right: Guinier representation of the SAXS data.

In a first step of the data analysis, the two-dimensional scattering data were azimuthally integrated with the program package fit2d after calibration of the setup so that the scattered intensity was available as a function of wave vector transfer q. In a second step, the background measurement was subtracted from the protein scattering data. The thus cleaned SAXS data were then analyzed in Guinier representation with respect to their gyration radius. Finally, the gyration radius was plotted as a function of the radiation dose, which was calculated taking into account the incident photon flux and the absorption in the sample for the corresponding irradiation time.

Figure 1, left shows the SAXS data of the four proteins after an irradiation time of 600 s (first frame) while Figure 1, right shows the relevant measurement range in the Guinier plot (ln(I) versus q^2) as well as the fits to the measurement data using a linear regression. The analysis of the data for the different proteins yields a Gryration radius R_g of (1.6± 0.03) nm for RNase, (1.44±0.01) nm for Lysozyme,
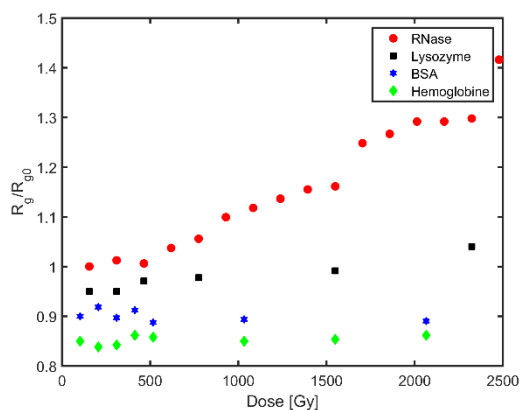
Figure 2: Evolution of the radii of gyration. The radii R_g were normalized to the radius obtained from the first frame R_{g0}. For a better overview, the data sets have been shifted vertically against each other.

(3.19±0.01) nm for BSA and (2.51±0.02) nm for hemoglobin, which is in agreement with the literature values within the error bars [1-4]. Figure 2 shows the temporal development of the gyration radii as a function of dose. The measured gyration radii were divided by the gyration radius of the first image. It is clear that the proteins behave very differently. While the gyration radii of RNase and lysozyme increase strongly from a dose of about 500 Gy, the radii of the other two proteins hardly seem to change. It should be noted that the measurements of RNase at high doses in the Guinier region already show a strong non-linear behavior, which indicates the aggregation of RNase. A similar behavior was also observed for lysozyme. In conclusion, the proteins BSA and hemoglobin, which show a more unstable behavior under the variation of temperature and pressure, show smaller changes in the gyration radii, which, however, could also be explained by a lower tendency to aggregation after damage by radiation.

[1] Zhou, J.-M.; Fan, Y.-X.; Kihara, H.; Kimura, K.; Amemiya, Y. (1998): The compactness of ribonuclease A and reduced ribonuclease A. FEBS letters 430 (3), S. 275–277.

[2] Chacón, P.; Morán, F.; Díaz, J. F.; Pantos, E.; Andreu, J. M. (1998): Low-Resolution Structures of Proteins in Solution Retrieved from X-Ray Scattering with a Genetic Algorithm. Biophysical Journal 74 (6), S. 2760–2775.

[3] Santos, S. F.; Zanette, D.; Fischer, H.; Itri, R. (2003): A systematic study of bovine serum albumin (BSA) and sodium dodecyl sulfate (SDS) interactions by surface tension and small angle X-ray scattering. Journal of colloid and interface science 262 (2), S. 400–408.

[4] Schelten, J.; Schlecht, P.; Schmatz, W.; Mayer, A. (1972): Neutron Small Angle Scattering of Hemoglobin. Journal of Biological Chemistry 247 (17), S. 5436–5441.

The effect of additives on the lamellar-to-cubic transition dynamics of monoolein at excess water conditions

Jaqueline Savelkouls*, Michelle Dargasz, Michael Paulus

Fakultät Physik/DELTA, TU Dortmund, 44221 Dortmund, Germany

*E-mail: jaqueline.savelkouls@tu-dortmund.de

Monoolein is an amphiphilic lipid, which is of particular interest in the pharmaceutical industry. Monoolein swells in excess water and forms several lyotropic liquid crystalline structures. The most pharmaceutically relevant structure is the highly ordered cubic Pn3m phase in the form of a physically stable viscous gel. In the cubic phase, monoolein can release a previously added drug by slow diffusion in the human body [1]. Measurements are now being made at beamline BL2 using the small angle X-ray scattering (SAXS) set-up to study the pressure-induced transition from the lamellar crystalline phase to the cubic Pn3m phase. All measurements are performed at a photon energy of $12\,\mathrm{keV}$ and a temperature of $26\,^\circ\mathrm{C}$. $20\,\mathrm{wt}\%$ monoolein in water is prepared and additives such as salts or drugs are mixed into the monoolein. After the sample preparation, the system is allowed to equilibrate for 12 hours. The sample is then positioned in a high pressure cell in the SAXS set-up. Initially, a scan is taken at a pressure of $100\,\mathrm{bar}$ to determine the lattice constant at equilibrium. Then the pressure is increased to $3000\,\mathrm{bar}$ and a scan is taken again. The pressure increase induces a transition from the cubic Pn3m phase to the metastable lamellar phase. A subsequent pressure decrease to $1500\,\mathrm{bar}$ brings the system into a stable lamellar phase. Figure 1(a) visualizes the integrated SAXS data of a scan from each phase region before the pressure jump. This is followed by a pressure jump to $100\,\mathrm{bar}$, which lasts $30\,\mathrm{s}$. After the pressure jump, scans are recorded every $3\,\mathrm{min}$ for several hours. Figure 1(b) illustrates the corresponding integrated SAXS patterns of monoolein at $100\,\mathrm{bar}$ at different time points after the pressure jump. It can be observed that the sample system falls back to the cubic Pn3m phase. The phases as well as the corresponding lattice constant a can be determined from the different diffraction patterns. The reflections occur at certain multiples of the reciprocal lattice constant which is characteristic of each phase. For the cubic phase the multiples are $\sqrt{2}, \sqrt{3}, \sqrt{4}...$ and for the lamellar phase $1, 2, 3...$ [2].

The results show that a much larger lattice constant of the Pn3m phase is formed after the pressure jump than before the pressure rise (see Figure 2(a)). Given some time, the system relaxes, causing the lattice constant to approach the equilibrium lattice constant. The rate of relaxation depends on the added additives. Figure 2(b) shows the evolution of the lattice constant's over time. It is obviously that the lattice constant of the Pn3m phase at equilibrium is higher than that of the pure monoolein when the drug AspirinComplex is added. In comparison, the equilibrium lattice constant with the addition of salts is lower than the equilibrium lattice constant for pure monoolein. Figure 2(b) also shows that the relaxation is faster while adding salts comed to the sample system with AspirinComplex.

In summary, the formation of the liquid crystalline phases of the amphiphilic lipids allows drugs to be released over a long period of time. The speed of diffusion can be optimized by the addition of salts.

1

(a) Before the pressure jump.

(b) After the pressure jump.
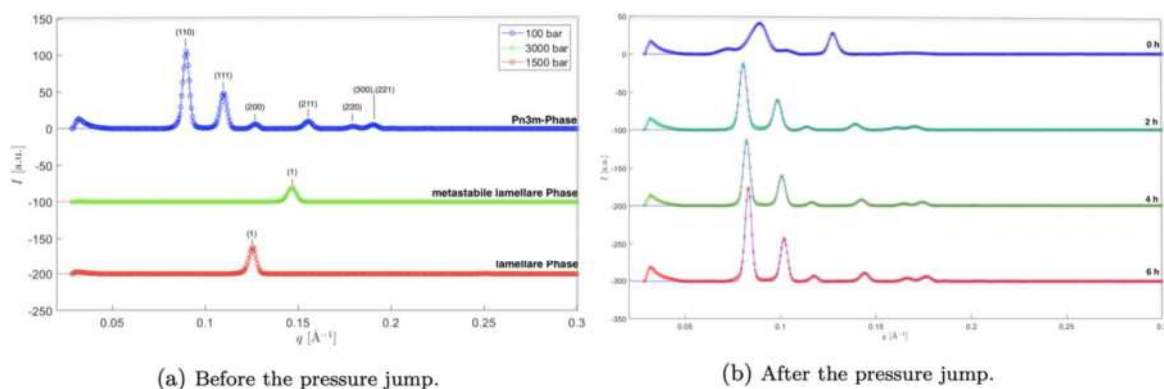
Figure 1: (a) Integrated SAXS data of one scan from each phase regime before the pressure jump. The lattice planes that correspond to the observed Bragg reflections are designated. (b) Integrated SAXS patterns of monoolein in the Pn3m phase at 100 bar at different times after the pressure jump. The curves are vertically shifted for clarity. In the diagrams, I is the intensity and $q = \frac{4\pi}{\lambda}\sin(\frac{\alpha}{2})$ is the wave vector transfer.

(a) Averaged lattice constants of the Pn3m phase.

(b) Relaxation of the Pn3m lattice constant a.
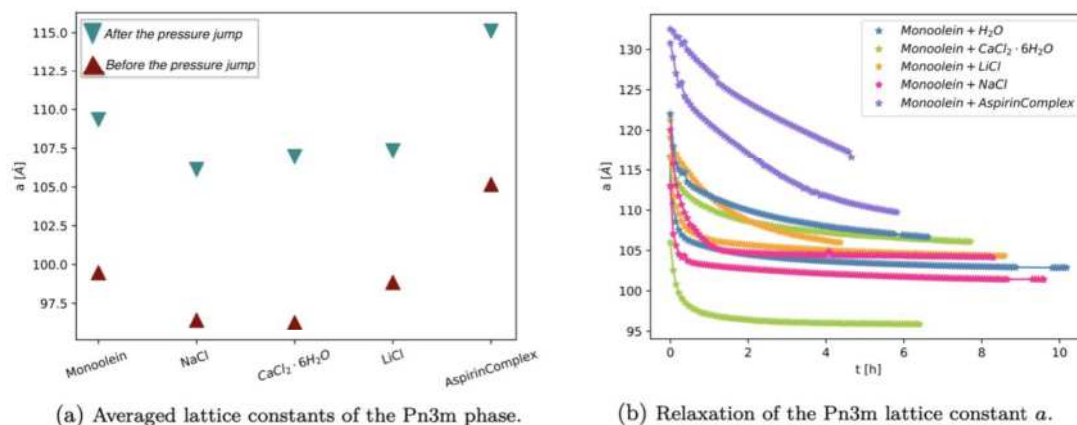
Figure 2: (a) Averaged lattice constants of the Pn3m phase at 100 bar before and directly after the pressure jump. (b) Relaxation of the Pn3m lattice constant a after a pressure jump from 1500 bar to 100 bar.

References

1. Adriana Ganem-Quintanar, David Quintanar-Guerrero and Pierre Buri; "Monoolein: A Review of the Pharmaceutical Applications" in *Drug Development and Industrial Pharmacy* (02.07.2010); p.813; (https://www.tandfonline.com/doi/pdf/10.1081/DDC-100101304?needAccess=true)

2. Chandrashekhar V. Kulkarni Wolfgang Wachter, Guillermo Iglesias-Salto, Sandra Engelskirchenb and Silvia Ahualliac; "Monoolein: a magic lipid?" in *Physical Chemistry Chemical Physics* (2011); p.3008; (https://pubs.rsc.org/en/content/articlelanding/2011/CP/C0CP01539C)

2

Structure formation in liquid primary aliphatic amines

M. Paulus, T. Janßen, J. Bolle, C. Albers, S. Dogan, E. Schneider, G. Surmeier, and C. Sternemann

Fakultät Physik/DELTA, Technische Universität Dortmund, Maria-Goeppert-Mayer-Str. 2, 44227 Dortmund, Germany

Despite a wealth of studies on liquid alcohols in order to understand their structure formation on a mesoscopic length scale and their dielectric response [1], studies on primary amines are still scarce although they are highly relevant for applications in chemical industry and pharmacology. However, they attracted interest in the recent years, both from a theoretical point of view [2] but also in comparison with experiment [3], as the amines differ from a structural point of view only in the amine group compared to the hydroxyl group in the alcohols while having the same alkyl tail. Hence, the structure formation in amines is likewise triggered by formation of hydrogen bonds, with the difference of weaker tendency for hydrogen-bonding while exhibiting two donor sites which might favor branching in cluster formation.

In this experiment we studied the temperature dependence of structure formation in a series of primary aliphatic amines by systematic variation of the chain length from propylamine to octylamine in order to compare these results with the corresponding linear monohydroxy-alcohols (MAs) [4,5]. The experiment was performed at beamline BL2 of the DELTA synchrotron radiation source using the wide-angle X-ray scattering setup with an incident energy of 12 keV, a bandwidth of 10^{-3}, and beam size of 1x1 mm^2. The diffraction data were collected by a MAR345 image plate detector and the temperature was varied with a liquid nitrogen cryostream cooler in the range between 152 K and 350 K depending on the amines' melting and boiling points.

The diffraction patterns of measured amines at room temperature are compared in figure 1. Within all the patterns the first sharp diffraction peak is observed at a wave-vector transfer q of about 14.2 nm^{-1} with only slight variation as function of chain length. This behavior confirms that it appears due to correlations between methylene/methyl groups like in the MAs. Although not as pronounced as in the MAs, all amines exhibit the pre-peak structure in the q-range 3 to 5 nm^{-1} as a manifestation of the mesoscopic heterogeneity of the liquids [3]. It indicates transient supramolecular associates with average size scaling with their alkyl chain length, i.e. with increasing chain length the pre-peak shifts to lower q. We find an intriguing temperature dependence of the pre-peak behavior with temperature both regarding its position and intensity. This is exemplified for the case of propylamine as presented in figure
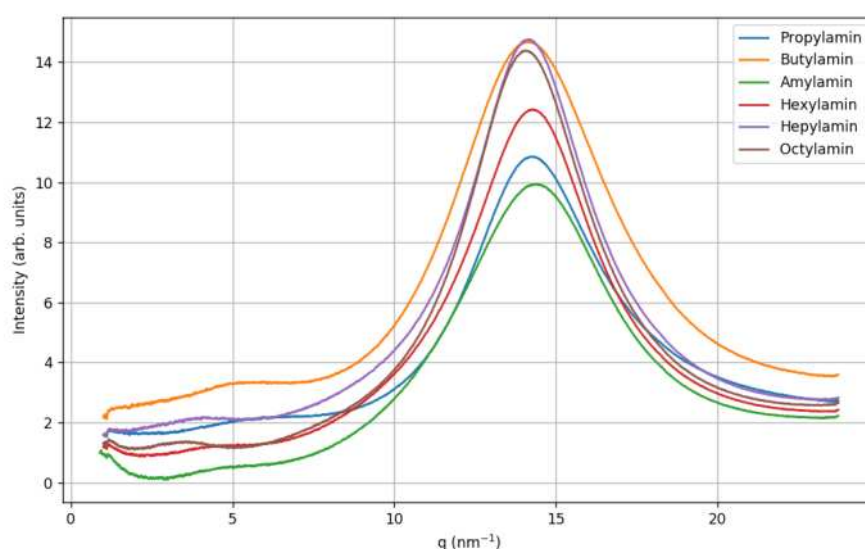

Figure 1: Diffraction patterns of primary aliphatic amines of different chain length measured at room temperature. All samples show besides the first sharp diffraction peak a pre-peak associated to transient supramolecular structure formation.
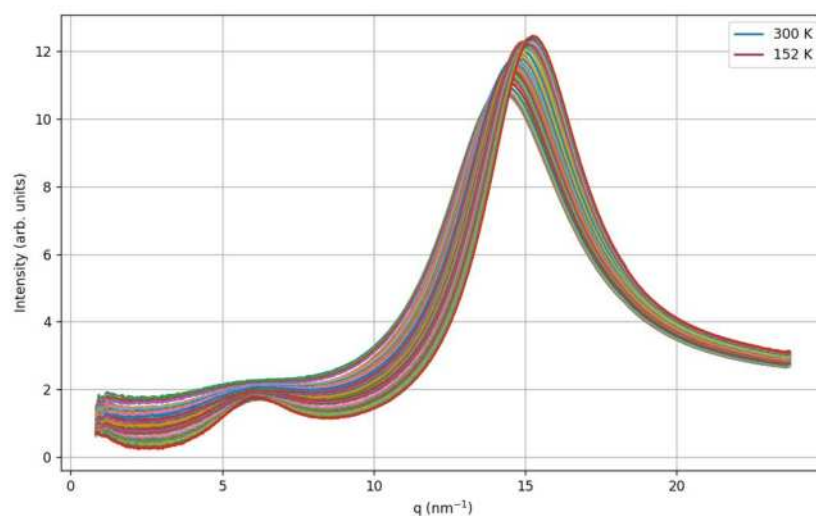
Figure 2: Diffraction patterns of propylamine measured at temperatures ranging from 152 K to 350 K. The pre-peak intensity increases significantly with decreasing temperature.

2. At low temperature the clusters composed of hydrogen-bonded nitrogen cores surrounded by the flexible alkyl tails reflect in a well-defined pre-peak. With increasing temperature the pre-peak is significantly suppressed for all amines and even vanishes in some cases. This behavior can be understood by formation of larger-branched clusters at low temperature while cluster formation is strongly disturbed at higher temperatures. Latter is in accordance to the weaker tendency of hydrogen-bonding in amines compared to the MAs and the tendency of branched clusters due to the existence of two donor sites in the amines. This picture is strongly supported by the temperature dependence of the pre-peak position which moves initially to larger wave-vector transfer q and then reverses its trend for lower temperatures, i.e. a signature of the formation of larger and larger branched linear structures during cooling [4,5]. This formation sets in at much higher temperatures compared to the respective alcohols which likewise can be attributed to weaker bonding properties of the amines. These results will be compared with predictions of cluster formation extracted from molecular dynamics simulations of liquid amines.

References

[1] R. Böhmer, C. Gainaru, and R. Richert, Structure and dynamics of monohydroxy alcohols— milestones towards their microscopic understanding, 100 years after Debye, Physics Reports 545, 125 (2014); [2] M. Požar and A. Perera, On the micro-heterogeneous structure of neat and aqueous propylamine mixtures: A computer simulation study On the X-ray scattering pre-peak of linear mono-ols and the related microstructure from computer simulations, Journal of Molecular Liquids 227, 210 (2017); [3] L. Almasy, A.I. Kuklin, M. Požar, A. Baptista, Microscopic origin of the scattering pre-peak in aqueous propylamine mixtures: X-ray and neutron experiments versus simulations, Physical Chemistry Chemical Physics 21, 9317 (2019); [4] M. Požar, J. Bolle, C. Sternemann, and A. Perera, On the X-ray scattering pre-peak of linear mono-ols and the related microstructure from computer simulations, Journal of Physical Chemistry B 124, 8358 (2020); [5] J. Bolle, S.P. Bierwirth, M. Požar, A. Perera, M. Paulus, P. Münzner, C. Albers, S. Dogan, M. Elbers, R. Sakrowski, G. Surmeier, R. Böhmer, M. Tolan, and C. Sternemann, Isomeric effects in structure formation and dielectric dynamics of different octanols, Physical Chemistry Chemical Physics 23, 24211 (2021).

Acknowledgments

The effect of D_2O on the pressure dependent protein-protein interaction in aqueous lysozyme solutions

Michelle Dargasz, Michael Paulus, Jaqueline Savelkouls

Fakultät Physik/DELTA, TU Dortmund, 44221 Dortmund, Germany

In some experimental techniques such as neutron scattering, infrared spectroscopy and NMR spectroscopy, the substitution of H_2O with D_2O is used to obtain a useful signal. It was assumed that the exchange of the solvent does not have a major influence on the protein structure and interactions [1]. However, previous research results show that lysozyme is more compact and less flexible in D_2O [2]. It was also found that lysozyme in D_2O has lower solubility and greater stability to thermally induced denaturation [3]. In addition, measurements with lysozyme in D_2O, in contrast to lysozyme in H_2O, revealed a larger attractive component of the protein-protein interaction potential [4]. This effect was studied mainly as a function of temperature. In this study, the pressure-dependent behavior of lysozyme in both solvents was investigated using SAXS. In previous studies of the pressure-dependent behavior of lysozyme in H_2O, a nonlinear relationship between the interaction potential and the exerted pressure was observed [5]. In the scattering curves of high concentrated lysozyme solutions, a shift of the correlation peak to higher q-values (q= $\left(\frac{4\pi}{\lambda}\right)\sin\left(\frac{\theta}{2}\right)$) occurs with increasing pressure up to about 2 kbar. However, the peak shifts back to smaller q-values with further increasing pressure. For such systems, an interaction potential with a long-range repulsion and short-range attraction can be assumed. If the attractive part of the interaction potential is considered as a function of pressure, the curve shows a minimum at the pressure value of 2 kbar. The final clarification of whether this effect occurs due to the influence of pressure on the solvent or is caused by the lysozyme itself has not yet been carried out. Therefore, it is also worthwhile to investigate this behavior with a modified solvent, using D2O instead of H2O.

For the measurements, lysozyme was dissolved at a concentration of 7 wt% in a 25 mM BisTris-H_2O and BisTris-D_2O buffer at pH 7. Small angle X-ray scattering experiments (SAXS) were performed at beamline BL2 of the DELTA synchrotron radiation source at a photon energy of 12 keV. During the SAXS experiments, the pressure was increased from 0 to 4 kbar in 250bar steps using a high pressure cell. Also, recordings were made in 1000 bar steps as the pressure was lowered. Since the sample cells did not seal completely when the pressure was increased, the protein concentration changed slightly during the measurement. Therefore, only the data recorded when the pressure was lowered were used in the evaluation. However, this problem was solved by the use of an additional sealing ring.

Following the measurements, the positions of the correlation peak were evaluated as a function of pressure. The shift of the peak with a maximum value for q_{cor} of 2 kbar in H_2O could be reproduced in the measurements. The shift is also visible for the lysozyme in D_2O. An exemplary scattering curve of lysozyme in H_2O illustrating the position change of the correlation peak can be seen in Figure 1 (a). By fitting the maximum of

1

the scattering curve with a gaussian curve, the q_{cor}-values with associated pressure could be determined and then plotted against each other. This was done for the measurements in H_2O and D_2O, as well as for measurements where the solvent consisted of 50 % D_2O and 50 % H_2O. The resulting plot can be seen in Figure 1 (b).

(a)   **(b)**
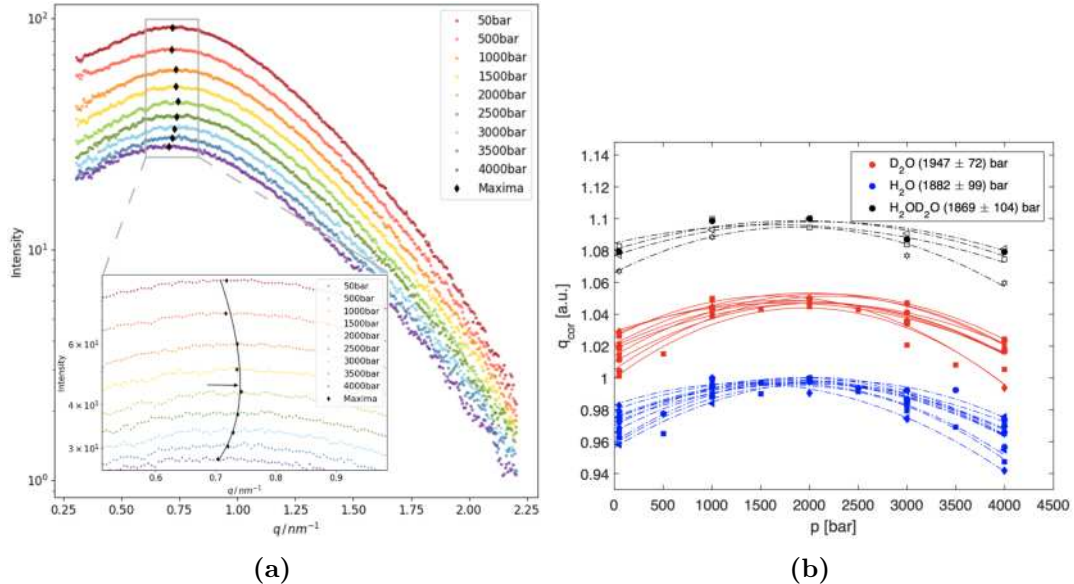
Figure 1: (a) Scatter curves of an exemplary measurement in H_2O with representation of the correlation peak shift. (b) Position of the correlation peak as a function of pressure in H_2O, D_2O and in the 50:50 D_2O:H_2O mixture.

It becomes clear that the averaged maxima of the curves differ only very slightly. The maximum for the correlation peak in H_2O is at (1882 ± 99) bar, in D_2O at (1947 ± 72) bar and in the 50:50 measurement at (1869 ± 104) bar. This could indicate that the water structure may play a rather minor role with respect to the occurring nonlinear correlation.

References:

[1] Michal K. Braun, Marcell Wolf, Olga Matsarskaia, Stefano Da Vela, Felix Roosen-Runge, Michael Sztucki, Roland Roth, Fajun Zhang and Frank Schreiber, *Journal of physical chemistry B* 212, 1731-1739 (2017)

[2] Y.M. Efimova, S. Haemers, B. Wierczinski, W. Norde, A. A. van Well, *Biopolymers* 85, 264-273 (2007)

[3] C. Gripon, L. Legrand, I. Roesnmann, O. Vidal, M.C. Robert, F. Boué, *Journal of Crystal Growth* 177, 238-247 (1997)

[4] C. Gripon, L. Legrand, I. Roesnmann, O. Vidal, M.C. Robert, F. Boué, *Journal of Crystal Growth* 178, 575-584 (1997)

[5] Martin A. Schroer, Jonas Markgraf, D.C. Florian Wieland, Christoph J. Sahle, Johannes Möller, Michael Paulus, Metin Tolan, and Roland Winter, *Phys. Rev. Lett.* 106, 178102 (2011)

2

A small- and wide angle x-ray scattering study on polyester thickened lubricating greases

Max Jopen[1], Michael Paulus[2], Christian Sternemann[2], Patrick Degen[3] and Ralf Weberskirch[1]

[1]Weberskirch Group, Faculty of Chemistry and Chemical Biology, Technical University of Dortmund, Otto-Hahn-Str. 6, 44227 Dortmund, Germany, [2]Fakultät Physik/DELTA, TU Dortmund, 44221 Dortmund, Germany, [3]Carl Bechem GmbH, Weststraße 120, 58089 Hagen, Germany

Lubricating greases are ubiquitous in industry and in everyday life. On the one hand, they prevent premature wear and, on the other hand, they save energy by reducing friction. For this reason, many different lubricating greases, some of them with very complex structures, have been developed in the past to cover a wide range of requirements, such as pressure and temperature stability. However, the enormous use and consumption of lubricants poses an environmental problem, as the main components are not biodegradable and often derived from petrochemicals. Thus, the development of environmentally friendly lubricating grease is an important task in current research.

Lubricating greases usually consist of a base oil (70 – 97%), a thickener (3 – 30%) and additives (0 – 10%). In this study a biodegradable polyester thickener was used in combination with three different base oils. The base oils used were Brightstock 150 (mineral oil), Spectrasyn 40 (synthetic polyalphaolefin oil) and castor oil (bio-based ester oil).

Small angle X-ray scattering (SAXS) and wide-angle X-ray scattering (WAXS) were performed at beamline BL2 (SAXS, photon energy: 12 keV) and at beamline BL9 (WAXS, photon energy: 27 keV). All measurements were recorded at a temperature of 25° C. A MAR345 image plate detector was used for data collection at both beamlines. Silverbehenate (SAXS) and silicon powder (WAXS) were measured to calibrate the set-up. The evaluation of the data was done with the software package FIT2d.
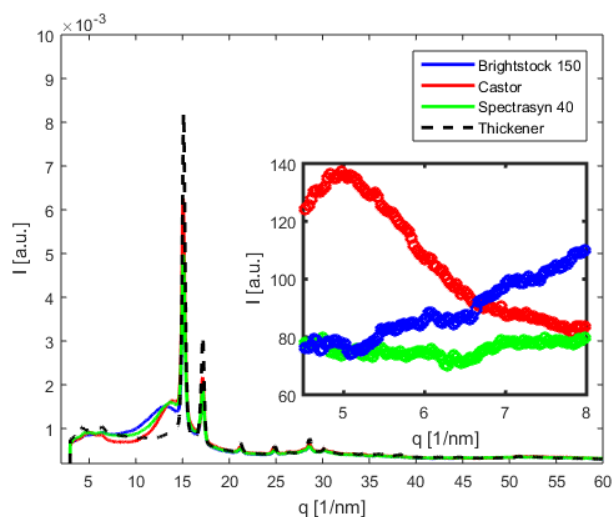
Figure 1: WAXS data of the greases studied. The inset shows an extract from the data in which the contribution of the crystalline phase was eliminated by subtraction.

The WAXS data of the investigated sample systems are shown in figure 1, while the SAXS data is presented in figure 2. The comparison between the WAXS data of the thickened oils and the extracted thickener reveals crystalline regions in the thickened oils whose structure is comparable to that of the thickener itself supporting crystallization of the thickener after addition to the oil. Furthermore, the WAXS data show a first sharp diffraction peak typical for liquids and disordered systems at wave vector transfers between 10 nm^{-1} and 20 nm^{-1} assigned to atom-atom correlations in the oils. Interestingly, the sample containing castor oil exhibits an additional intensity maximum at 5 nm^{-1} (see inset of figure 1) which is a signature for liquids interacting with each other via hydrogen bonds and thus forming (transient) supramolecular structures. This signature is not observed for the non-polar oils. The diffraction data of the crystalline fraction of the signal of the thickened oils indicate that portions of the sample crystallize in a triclinic crystal structure whose unit cell has significantly different lengths depending on orientation. While the (00l) reflections

Figure 2: SAXS data of the three investigated greases and the thickener.

are only visible in the SAXS data as broad correlation peaks, which also differ in their position and width depending on the oil used, the (hk0) reflections in the WAXS spectra show no clear variations depending on the oil used. An analysis of the peak positions yields a unit cell with a height of 15.5 nm, while the lattice vectors in the lateral direction have a length of only 0.37 nm and 0.42 nm, respectively, and enclose an angle of 83°. Based on the less pronounced intensity of the maxima of the sample containing castor oil in the SAXS data, it can be concluded that this sample has a slightly lower crystallinity compared to the others. In a next step, these structural data will be correlated with the results of other methods such as rheology and infrared spectroscopy to obtain a comprehensive picture of these systems.

Adsorption of supercritical hexafluoroethane on hydrophobic interfaces near the critical point - test of the new high pressure/high temperature sample cell.

Mike Moron, Susanne Dogan, Marc Moron, Nicola Thiering, Julia Nase, Michael Paulus, and Metin Tolan

Fakultät Physik/DELTA, TU Dortmund, 44227 Dortmund, Germany

We investigated the pressure-dependent adsorption of supercritical hexafluoroethane (C_2F_6) on hydrophobic surfaces. Silicon wafers were hydrophobized by coating them with a self-assembled octadecyltrichlorsilane (OTS) monolayer. OTS molecules bind covalently with their polar head group to the wafer surface. Thus, the nonpolar alkyl chains form a stable, hydrophobic surface. When the OTS wafer is placed in the sample cell and C_2F_6 is introduced to it, a thin adsorption layer forms on the wafer surface. Since the thickness of the adsorbed layer are on the atomic scale, we performed X-ray-reflectivity (XRR) experiments with a photon energy of 27 keV at the beamline BL9 at DELTA. With the XRR technique we obtain direct insight into the vertical electron density profile of the substrate and the adsorbed C_2F_6-layers.

C_2F_6 has its critical point at a pressure of p_{crit} = 30.48 bar and at a temperature of T_{crit} = 19.88 °C. The maximum gas pressure in the gas cylinder is approx. 31 bar. Therefore, is not possible to measure far above the critical pressure without heating the gas in the sample cell under isochoric conditions. With the new sample cell, it is possible to reach temperatures of up to 500 °C. It can withstand pressures up to 1000 bar.

Fig. 1 a) shows a sectional view of the sample cell along the sapphire window plane, which is parallel to the beam direction. The OTS- wafer is placed in the sample cell via the opening for the sealing plug in a custom-built holder. The X-ray beam passes through the sapphire window with a thickness of d = 7.5 mm and is
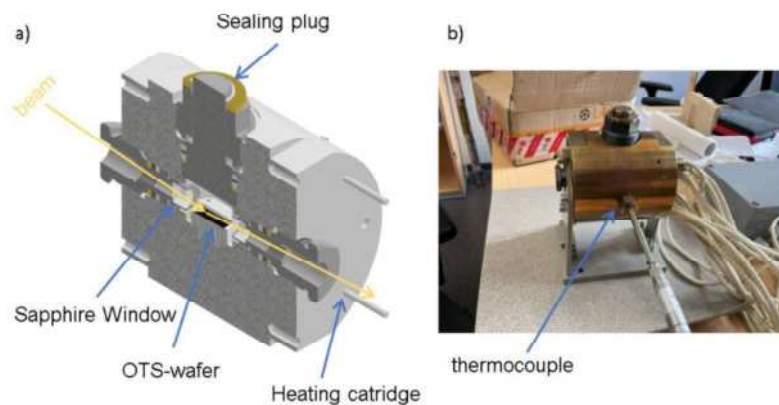

Fig. 1: a) Sectional view of sample cell. b) Image of sample cell in holder with attached thermocouple.

reflected by the sample. The reflected beam is recorded by a Pilatus 100k detector. Fig. 1 b) shows a photo of the sample cell with the thermocouple attached. The thermocouple measures the temperature directly in the sample cell. It is connected to a

1

temperature controller (Eurotherm 3508), which regulates the heating power of the heating cartridges depending on the current temperature and the set temperature.

We recorded reflectivity curves for three pressure/temperature series at pressures between 1 bar and 41 bar and temperatures between 24 °C and 200 °C. One of them will be discussed exemplarily. We first performed a reference measurement of the substrate with air in the sample cell. Then, the sample cell is flushed with C_2F_6 and a reflectivity is recorded at 1 bar gas pressure. After that, the gas pressure in the sample cell is increased up to the maximum pressure of the bottle and a measurement is taken.

The sample cell is shut off with a valve so that the gas lines can be depressurized and detached without dropping the pressure inside the sample cell. From here on, reflectivities are measured at different temperatures. The recorded reflectivity curves for C_2F_6 at different pressures are shown in Fig. 2. With increasing pressure, the first minimum of the reflectivity curves shifts to lower q_z indicating the adsorption of a C_2F_6-layer. The depth of the minimum decreases with increasing pressure, implying adsorption of a very thick and rough layer. In the reference measurement after the pressure/temperature series (1 bar down @ 24 °C), there are many minima with smaller spacing, indicating an ordered layer on the wafer surface. This could be due to the slow release of pressure leading to a

Fig. 2 Reflectivity curves of the pressure/temperature series with C_2F_6

temperature decrease and thus condensation of the gas on the wafer surface. Because the X-ray beam passes through a total of about 15 mm of sapphire and a very dense atmosphere at high pressures, the count rates at high reflection angles are already very close to the background signal. To obtain a strong signal at high reflection angles, a higher beam energy is necessary. The data is still under evaluation.
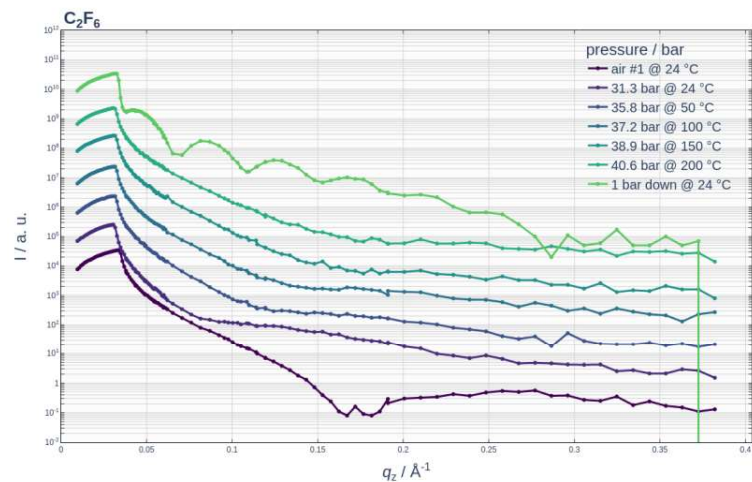
2

Characterization of cylindrically bent Si(111) analyzer crystals

Nicola Thiering[1], Christian Albers[1], Johannes Kaa[1,2], Christian Sternemann[1]

[1] Fakultät Physik/DELTA, Technische Universität Dortmund, 44227 Dortmund, Germany;
[2] European X-ray Free-Electron Laser Facility GmbH, 22869 Schenefeld, Germany

A set of four cylindrically bent Si(111) anaylzer crystals with 250 mm bending radius was tested using the von Hamos spectrometer at beamline BL9 of DELTA. These crystals will be used for forthcoming experiments with the von Hamos spectrometer located at the High Energy Density (HED) instrument of the European X-ray Free-Electron Laser (EuXFEL) which was implemented by TU Dortmund within the scope of the BMBF project 05K19PE2. In order to characterize these crystals the von Hamos spectrometer at beamline BL9 was modified to enable the use of crystals with 250 mm bending radius instead of the standard analyzers' design radius of 500 mm.

At first we probed the focusing capabilities of the crystals and measured the overall energy resolution of the setup using a nickel foil at an incident energy of 8260 eV at different heights of the incident beam ranging from 1.0 to 0.1 mm. The limitation of the energy resolution is dominated by the detector's pixel size of 172 µm, i.e. 1 eV per pixel, and the geometrical contributions from beam height and thickness of the sample while the contribution of the analyzer crystal (0.05 eV) is negligible. Fig. 1 shows the shape of the elastic line for different beam height as a sum of all analyzer signals. At 0.1 mm beam height the expected energy resolution (1.6 eV) was confirmed with 1.6±0.1 eV for each crystal. Exploiting much smaller beam with smaller detector pixel size as available at the HED instrument will provide sub-eV resolution. Subsequently we measured X-ray emission spectra of the Nickel K_β emission and the valance-to-core region with sufficient statistical accuracy within 7 hours of exposure (see Fig. 2). Such relatively long exposure times are due to the small band pass using a Si(311) monochromator at BL9 which strongly reduces the incoming flux for such applications. Overall the performance of the analyzers was validated so that they can be implemented at the von Hamos spectrometer of HED.
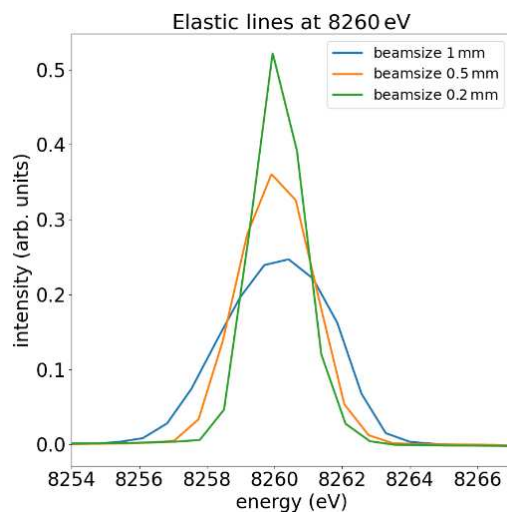

Fig. 1: quasi-elastic scattering of a nickel foil measured for different beam heights.
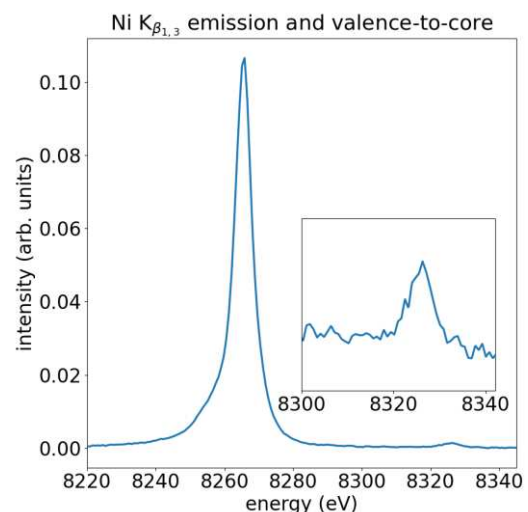

Fig. 2: K_β and valence-to-core spectra (inset) of a nickel foil.

Acknowledgments

Micro- and Nanostructure of PECVD Ti-Si-B-C-N Nanocomposite Coatings

Thewes, A.[1]; Paschke, H.[2]; Sternemann, C.[3]; Paulus, M.[3]

IOT TU Braunschweig, 44145 Dortmund, Germany

Fraunhofer Institute for Surface Engineering and Thin Films IST, Dortmund 44145, Germany

Fakultät Physik/DELTA, Technische Universität Dortmund, 44221 Dortmund, Germany

Introduction

Nanocomposite coatings received increasing attention in recent years due to outstanding mechanical and thermal properties primarily provided by their nanostructure [MOR20,PIL08,THA13]. The micro- and nanostructure of Ti-Si-B-C-N coatings are investigated in this study. The nanocomposite buildup, consisting of an amorphous (a-) matrix enveloping nanocrystalline (nc-) grains, shows a high hardness value of 24.9 GPa and a high oxidation resistance up to temperatures of approximately 900 °C.

Method

Ti-Si-B-C-N coatings were deposited on mirror finished (polished) DIN 1.2367 hot working steel and single-crystalline Si-wafers via Plasma Enhanced Chemical Vapor Deposition (PECVD). The chemical composition was determined via Electron Probe Microanalysis (EPMA). X-ray diffraction was carried out at room temperature. These measurements were performed at Beamline BL9 [KRY06] of the synchrotron light source DELTA (TU Dortmund, Dortmund, Germany). In order to determine the lattice orientation with respect to the samples surface a MAR345 image plate detector was used. The energy of the incident photon beam was E_0 = 27 keV and the beam size was set to 0.2 x 1.5 mm^2. The angle of incident was 1°. For grain size calculation using the Scherrer equation diffraction data was recorded by a PILATUS100k detector using a photon energy of 13 keV yielding a higher resolution compared to the MAR set-up. Focused Ion Beam (FIB) was applied to prepare a thin lamella for Scanning Transmission Electron Microscopy (STEM) measurements carried out at Fraunhofer Institute for Surface Engineering and Thin Films (IST).

Results

EPMA measurements yielded a chemical composition of 30.0 at.-% Ti, 9.6 at.-% Si, 15.5 at.-% B, 32.0 at.-% C, and 8.7 at.-% N with an additional 1.5 at.-% O and 2.7 at.-% Cl as residual elements from the deposition process. Figure 1 shows the two-dimensional diffraction images of a Ti-Si-B-C-N layer deposited on a silicon wafer. In addition to the Bragg reflections of the layer, there are reflections caused by thermal diffuse scattering from the silicon due to the penetration of the high energy X-ray beam into the substrate and Bragg reflections assigned to the enclosure of the sample by the heating cell. However, a distinct texture in the scattering intensity of the layer indicating an orientation of the (00l) planes of the cubic layer structure parallel to the substrate surface is observed. An analysis of the data taken with the PILATUS100k revealed a nc-Ti(C,N) grain size of 6.2 ± 0.6 nm.
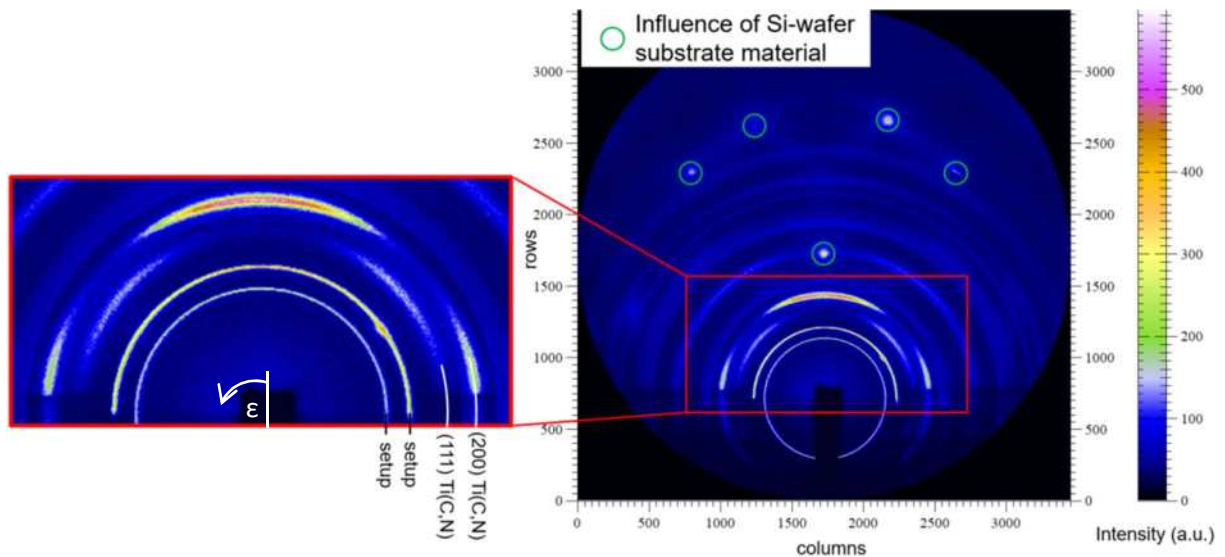
Figure 1: 2D X-ray diffraction pattern measured with a MAR345 image plate detector

An STEM picture of the coating is shown in Fig. 2. The coating deposition starts with a TiN adhesion layer that gradually changes to Ti-Si-B-C-N. The microstructure close to the coating/substrate interface appears to be dendritic with a TiN-rich composition. In contrast, the surface-near Ti-Si-B-C-N zone appears without long-range order (amorphous). Stripes from bottom to top result from different thicknesses of the lamella prepared by FIB method. Increased magnification confirms the grain sizes to be on a nanoscale, but the resolution is insufficient to measure the diameter of grains.
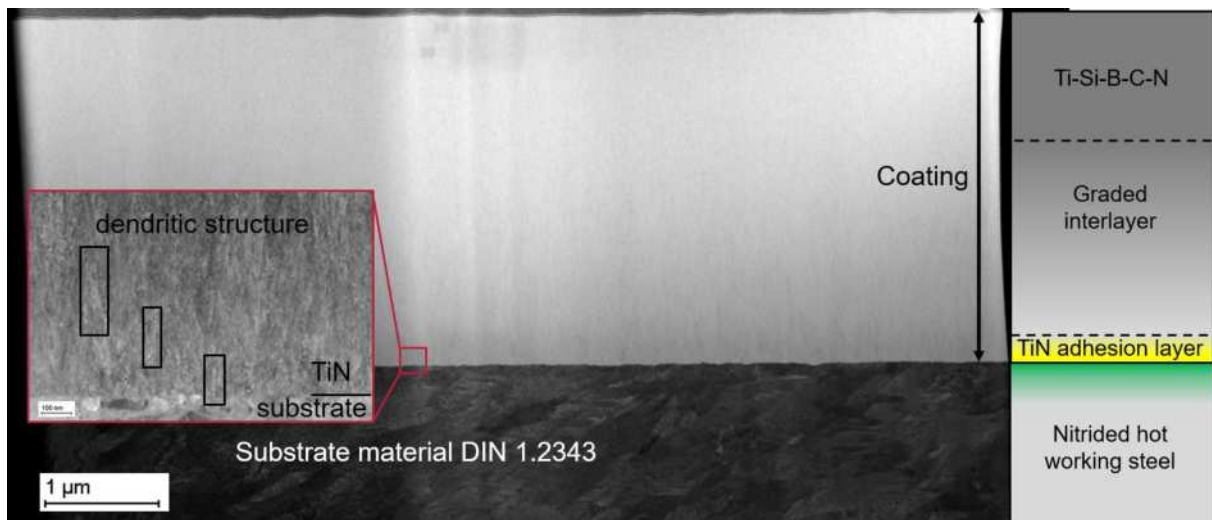
Fig. 2: STEM pictures with schematic micro build-up on the right hand side and close-up of the nanostructure in the hot working steel - TiN layer interface on the left hand side

Discussion and conclusion

Both X-ray diffraction and STEM analysis indicate that an anisotropic nano- and microstructure is created during coating deposition. Since two different substrates (silicon and hot working steel) were used for the experiments, it can be assumed that the observed layer properties were not caused by a substrate-specific interaction with the layer material. Considering the STEM image, the preferred orientation of crystal lattice can derive from the dendritic structures at the bottom of the coating (see Fig. 2) which change to more random orientations close to the layers' surface.

In conclusion, XRD at BL9 allows investigating the nanostructure of the Ti-Si-B-C-N nanocomposite coating. A preferred orientation of the crystallites with their (00l)-planes parallel to the substrates surface was observed using the MAR345 detector. Calculation of grain size by Scherrer equation

offered an average grain size of 6.2 nm. Observation of nanostructure with STEM confirmed the existence of nc-grains, but limited resolution hindered confirmation of the calculated average grain size.

In future work, High Resolution Transmission Electron Microscopy (HR-TEM) will be carried out to investigate the lattice structure of nc-grains and its orientation.

Literature

[KRY06]   Krywka, C.; Paulus, M.; Sternemann, C; Volmer, M.; Remhof, A.; Nowak, G.; Nefedov, A.; Pöter, B.; Spiegel, M. and Tolan, M. (2006): The new diffractometer for surface x-ray diffraction at beamline BL9 of DELTA. In: J. Synchrotron Rad. (13), p. 8.

[MOR20]   Moritz, Y.; Saringer, C.; Tkadletz, M. (2020): Oxidation behavior of arc evaporated TiSiN coatings investigated by in-situ synchrotron X-ray diffraction and HR-STEM. In: Surface & Coatings Technology (404).

[PIL08]   Pilloud, D.; Pierson, J. F.; Marco de Lucas, M. C.; Cavaleiro, A. (2008): Study of the structural changes induced by air oxidation in Ti–Si–N hard coatings. In: Surface and Coatings Technology 202 (11), p. 2413–2417.

[THA13]   Thangavel, E.; Lee, S.; Nam, K.-S-; Kim, J.-K.; Kim, D.G. (2013): Synthesis and characterization of Ti-Si-C-N nanocomposite coatings prepared by a filtered vacuum arc method. In: Applied Surface Science (265), p. 60-65.

The responsive behavior of zeolitic-imidazolate-framework-based porous liquids

Athanasios Koutsianos, Louis Frentzel-Beyme, Roman Pallach, Chinmoy Das, Sebastian Henke*

Anorganische Chemie – TU Dortmund, Otto-Hahn-Str. 6, 44227 Dortmund

Scientific Context

Owing to their unusual combination of permanent porosity and fluidity, porous liquids (PLs) have emerged as promising materials for catalytic and molecular separation applications.[1] Porous liquids are typically classified into three categories, namely type 1, type 2 and type 3. Neat liquid substances with empty molecular "hosts" are defined as type 1 PLs. Type 2 PLs are 2-component substances, comprising empty molecular hosts and size excluded solvents. Solid porous particles dispersed in sterically hindered solvents constitute multiphase type 3 PLs.[2]

Metal-organic frameworks (MOFs) and their subclass of zeolitic imidazolate frameworks (ZIFs) have been mainly employed as the microporous hosts in the Type 3 PLs.[3] Advancements in their field have also facilitated the evolution of "flexible" nanocrystals. The quintessential flexible MOFs $Zn(bim)_2$ and $Co(bim)_2$ (ZIF-7 and ZIF-9; bim^- = benzimidazolate) display a responsive behaviour undergoing structural transitions between a narrow pore (*np*) phase and a large pore (*lp*) phase upon adsorption of specific gas molecules (e.g. CO_2, propane and propene; see Figure 1a).[4] Correspondingly, they exhibit sigmoidal adsorption profiles characterized by minimal guest uptake below a temperature-dependent threshold pressure, followed by a sharp rise in adsorption.

Our recent efforts to incorporate such flexible nanoparticles in a size-excluded solvent to generate responsive PLs with unprecedented sorption properties have been successful. Nanocrystals of ZIF-7 and ZIF-9 have been dispersed in a low vapour pressure silicone oil and generated stable liquid systems that feature isotherms with a sigmoidal shape during adsorption of CO_2, propane and propene at room temperature (Figure 1b,1c and 1d).

At BL 9 at DELTA, we were able to collect X-ray diffraction (XRD) data of the ZIF-included PLs *in situ* during gas uptake/release, and accordingly visualize the structural changes of the MOF nanoparticles upon gas sorption in fluid suspension.

Experimental procedure

ZIF-based PLs were prepared by dispersing ZIF-7 or ZIF-9 nanoparticles (size about 100 nm) in silicon oil 704 to generate nanoparticle suspensions containing 10 wt% ZIF. An aliquot of the activated PLs (ca. 1.5 mL) was loaded in a Schlenk finger tube (diameter approx. 1 cm) and a PTFE stirring bar was added. The sample was mounted over a magnetic stirring plate in the centre of the goniometer of BL 9. The stirring rate was set at 300 rpm. The Schlenk tube was connected to a three-way ball valve to switch between sorption gas and vacuum (membrane pump). The PLs remained initially under vacuum and subsequently the gas (CO_2, propene) was dosed at a pressure of 1 bar at room temperature. XRD data were collected of the stirred PLs during gas uptake/release by PLs with a monochromatic X-ray beam (λ = 0.459 Å) using a MAR345 image plate detector.

Results

At first, we collected an XRD pattern for the activated ZIF-7-based PL under vacuum. Despite the strong contributions of the solvent and the glass tube to the pattern, broad peaks assignable

to the *np* phase of the ZIF nanoparticles are clearly visible.[5, 6] Exposure of the PL to CO_2 followed by gas uptake, results in the structural transformation of the ZIF-7 particles to their more crystalline *lp* phase, as manifested by the alterations in the obtained pattern (Figure 1e). The respective peaks at 0.51 and 0.54 Å^{-1} became much more intense, while the peaks at 0.49, 0.61 and 0.68 Å^{-1} lost intensity. These changes in the XRD pattern are in total agreement previous literature reports on the *np*-to-*lp* phase transformation of ZIF-7 bulk powder.

We also conducted an analogous XRD study on propene sorption by a related ZIF-9-based PL. The changes in the diffraction pattern after application of 1 bar propene are almost identical to the ones observed in the ZIF-7-based PL system under CO_2 sorption (Figure 1f), thus also corresponding to the *np*-to-*lp* transformation of ZIF-9 upon propene uptake. It should be noted, however, that the rather small interfacial area of gas-liquid contact (directly correlated with the experimental setup used) and the slow kinetics of gas diffusion in the silicone oil resulted in a very long equilibration time, so that the *np*-to-*lp* phase transition of the ZIF-7 particles could just be observed after more than 12 hours equilibration under 1 bar of CO_2.
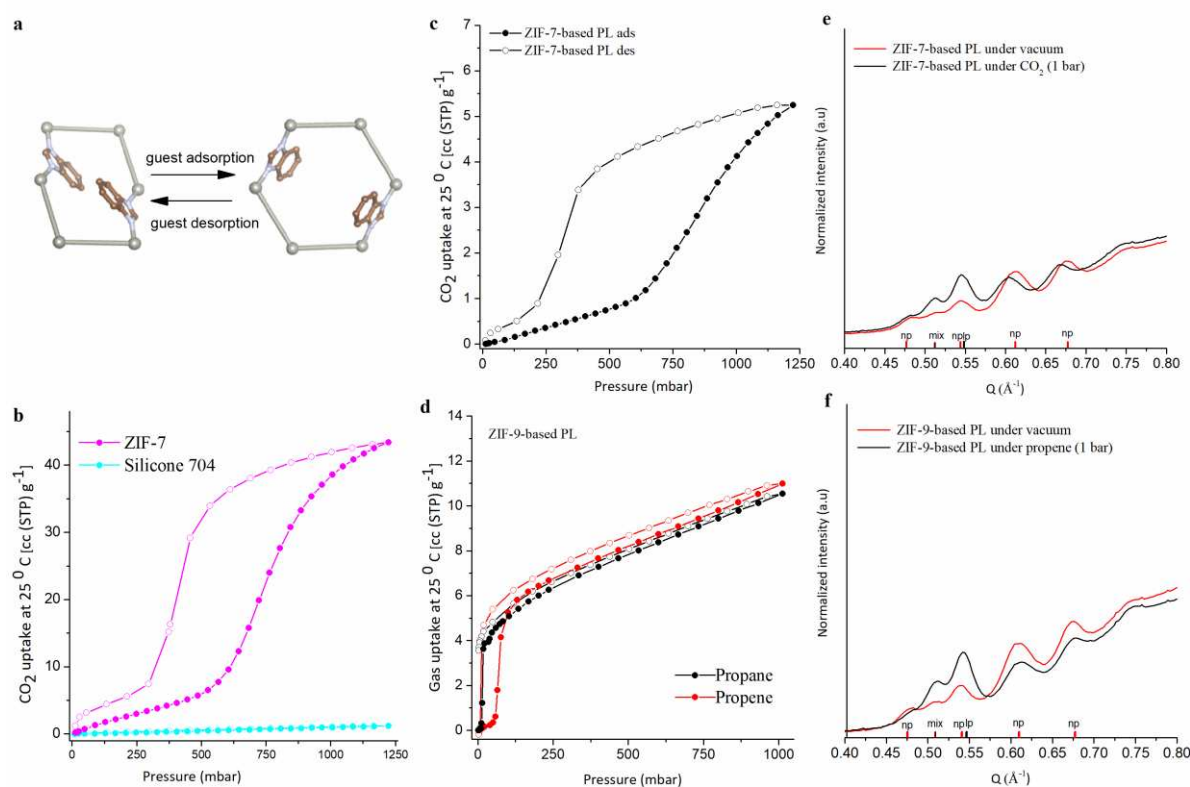
Figure 1: **a,** Schematic of the reversible guest-induced narrow pore (*np*) to large pore (*lp*) transition of ZIF-7 and ZIF-9 materials. **b,** CO_2 adsorption (filled symbols) and desorption (empty symbols) isotherms of pure ZIF-7 powder (magenta) and pure silicone oil (cyan) at 25 ^{0}C. **c,** CO_2 adsorption (filled symbols) and desorption (empty symbols) isotherms of the ZIF-7-based PL at 25 ^{0}C. **d,** Propane (black) and propene (red) adsorption (filled symbols) and desorption (empty symbols) isotherms of the ZIF-9-based PL. **e,** XRD patterns of the ZIF-7-based PL under vacuum (red) and conditioned at 1 bar CO_2 (black). **f,** XRD patterns of the activated ZIF-9-based PL under vacuum (red) and conditioned at 1 bar propene (black). Tick marks represent characteristic positions of the *np* and *lp* reflections of ZIF-7.

The specific experiment conducted at BL9 allowed us to verify that the observed step in the gas sorption isotherm is driven by the structural transition of the porous ZIF constituent, as it was conceived during the conceptualization of the responsive PLs. ZIF frameworks retain their flexible nature while being dispersed in the silicone oil and the developed PLs accordingly display distinct step-shaped isotherms. This result set the stage for the development of a new

type of synthetic fluid and responsive adsorbents with gas binding properties akin to complex biological fluids (i.e. blood).

References

1. Bavykina A, Cadiau A, Gascon J. Porous liquids based on porous cages, metal organic frameworks and metal organic polyhedra. *Coordination Chemistry Reviews* 2019, **386:** 85-95.

2. O'Reilly N, Giri N, James SL. Porous Liquids. *Chemistry – A European Journal* 2007, **13**(11)**:** 3020-3025.

3. Cahir J, Tsang MY, Lai B, Hughes D, Alam MA, Jacquemin J*, et al.* Type 3 porous liquids based on non-ionic liquid phases – a broad and tailorable platform of selective, fluid gas sorbents. *Chemical Science* 2020, **11**(8)**:** 2077-2084.

4. Schneemann A, Bon V, Schwedler I, Senkovska I, Kaskel S, Fischer RA. Flexible metal–organic frameworks. *Chemical Society Reviews* 2014, **43**(16)**:** 6062-6096.

5. Park KS, Ni Z, Côté AP, Choi JY, Huang R, Uribe-Romo FJ*, et al.* Exceptional chemical and thermal stability of zeolitic imidazolate frameworks. *Proceedings of the National Academy of Sciences* 2006, **103**(27)**:** 10186-10191.

6. McGuirk CM, Runčevski T, Oktawiec J, Turkiewicz A, Taylor MK, Long JR. Influence of Metal Substitution on the Pressure-Induced Phase Change in Flexible Zeolitic Imidazolate Frameworks. *Journal of the American Chemical Society* 2018, **140**(46)**:** 15924-15933.

On the crystalline structure of TiB$_2$ thin films deposited by different PVD technologies and bias voltages

Wolfgang Tillmann[1], Jiabin Gu[1,2], Dominic Stangier[1*], Nelson Filipe Lopes Dias[1],
David Kokalj[1], Christian Sternemann[3], Michael Paulus[3]

[1]Institute of Materials Engineering, TU Dortmund University, Germany

44227 Dortmund, Leonhard-Euler-Straße 2

[2]School of Mechanical Engineering and Automation, Beihang University, P.R. China

Beijing 100191, No. 37 Xueyuan Road

[3]Fakultät Physik / DELTA, TU Dortmund University, Germany

44227 Dortmund, Maria-Goeppert-Mayer-Straße 2

* corresponding author: dominic.stangier@tu-dortmund.de

The deposition of transition metal diborides has gained enormous interest in recent years and was intensively studied due to their unique properties [1]. Especially, the synthesis of titanium diboride (TiB$_2$) coatings by means of physical vapor deposition (PVD) technology was reported by several studies due to the high hardness, the increased thermal and chemical stability, as well as the outstanding tribological properties [2,3] being an excellent choice for highly stressed cutting tools [4]. Nevertheless, the deposition of such coatings by means of magnetron sputtering is highly challenging and strongly influenced by the plasma discharge, the ionization, and energy of the sputtered species, thermal growth effects as well as the base pressure [5,6]. All these parameters directly influence the crystalline growth and orientation of the TiB$_2$ coating which in turn, affect the mechanical and tribological properties of the coating system [7–9]. Additionally, the growth of the thin films can be controlled by the applied bias potential on the substrate material leading to densification and variation of the crystalline structure [10–12]. Recently, the combination of conventional DC magnetron sputtering with short high energetic discharges induced by high-power impulse magnetron sputtering (HiPIMS) within the same deposition process combines the advantages of both technologies as it is presented by Greczynski et al. for TiAlN coatings [13–15]. The high deposition rate of DC processes can be used in synergy with the increased ionization rate leading to an improved coating performance. However, this approach has so far not been investigated for TiB$_2$ coatings although presenting a promising approach for the deposition of hard wear-resistant coatings.

The high-speed steel AISI M2 (German material number 1.3343) with a hardness of 62 + 1 HRC was used as substrate material with metallographically polished surfaces and mounted on the two-folded handling system of the PVD device. For the deposition of the thin films an industrial coating machine CC800/9 Custom (*CemeCon AG, Germany*) was used. Prior to the deposition of the PVD coating, a sequence of heating and plasma etching processes

was conducted to ensure an oxide and contamination-free surface. The architecture of the thin films consists of a 200 nm thin Ti adhesion layer with an interlayer of 1.8 µm TiN. The top layer of TiB_2 which was deposited by different ways of applying the power in the cathodes (DC, HiPIMS, DC/HiPIMS hybrid process) was adjusted in the deposition time to reach a thickness of 1 µm. Additionally, the applied bias voltage on the handling system was varied from U_B = -70 V up to U_B = -130 V for each process variety to control the kinetic energy of the sputtered species [16]. The interlayer of TiN was selected to compensate the differences in the mechanical properties of the TiB_2 coating and the tool steel substrate material to improve the adhesion [17]. The investigation of the crystalline structure of the deposited coatings was conducted with a photon energy of E = 20 keV (λ = 0.6199 Å) using an image plate detector MAR345 (*marXperts GmbH, Germany*) enabling the possibility of 2D grazing incidence X-ray diffraction (XRD) at beamline BL9 of DELTA synchrotron radiation soruce. The measurements were conducted with an angle of incidence of ω = 0.5° with a measuring time of t = 300 s to ensure a surface-sensitive analysis of the coating systems. As reference material, Si powder was used and the evaluation of the patterns was conducted using Fit2d program package calibrating the sample to detector distance, detector tilt, and the beam center [18]. In order to determine the residual stresses of the second kind in the system, measurements were carried out with a higher resolution. Here, consistent with the phase analysis a photon energy of E = 20 keV and a beam height of 0.1 mm was used, while the angle of incidence was increased to ω = 4° to reduce the illuminated area on the sample. The diffractogran patterns were acquired with a PILATUS100k (*Dectris, Switzerland*) in 2Θ steps, and the individual images were added pixel by pixel. To determine the full width at half maximum (FWHM), the Bragg reflections were fitted by a Gaussian function. The FWHM was then evaluated using the method suggested by Williamson and Hall [19]. Here, only Bragg reflections were considered whose corresponding lattice planes were parallel to the sample surface (TiB_2: (001) and (002); TiN: (111) and (222)).

The results of the 2D diffractogran patterns, which are exemplarily presented for a bias voltage of U_B = -100 V for the three different variants of the plasma discharge, are illustrated in Figure 1. All patterns prove the before mentioned architecture of the coating which is composed of the Ti-interlayer indicated by the faint hexagonal Ti reflection in (110)-orientation at 2Θ = 16°. Furthermore, the fcc crystalline structure of the TiN interlayer in (111)- and (200)-growth direction can be determined, which is characteristic for the deposition of binary nitrides by PVD technology trying to minimize the surface energy [20]. A strong texturing can be observed, which shifts from the (111)-reflection from the in-plane orientation for an azimuth of χ = 90° to higher and lower values for the (200)-growth direction. These results can be ascribed to the increased kinetic energy of the ions, which favor a (200)-orientation due to an increased surface mobility of the adatom [21]. Additionally, the α-Fe Bragg reflections for (110)- and (200)-orientation from the high-speed steel are observed. So far, no differences with respect to the interlayer design and the substrate material can be noticed.

In accordance to these findings the TiB_2 functional top layer, which was deposited by the different PVD technologies, shows no significant changes in the phase composition. For all coating systems the (001)-, (100)- and (110)-growth direction of the TiB_2 phase are observed, which are characteristic for the hexagonal crystalline structure of PVD thin films. These systems favor a direction of the planes which are oriented perpendicular to the film growth [12], leading to the lower surface free energy parallel to the film surface [17]. Therefore, it can

be assumed that sufficient energy input during the film growth for all three PVD processes was provided [22]. These findings are supported by the results presented by Nedfors et al. revealing that a process temperature of 500°C with an average energy per species above E = 50 eV fosters the change in the preferred orientation from (110) to (001) [7]. For this reason, one may propose, that the phase formation of the high energetic processes is dominated by the kinetic energy and the impulse transfer on the surface of the substrate, whereas the conventional magnetron sputtering processes are controlled by the surface temperature.
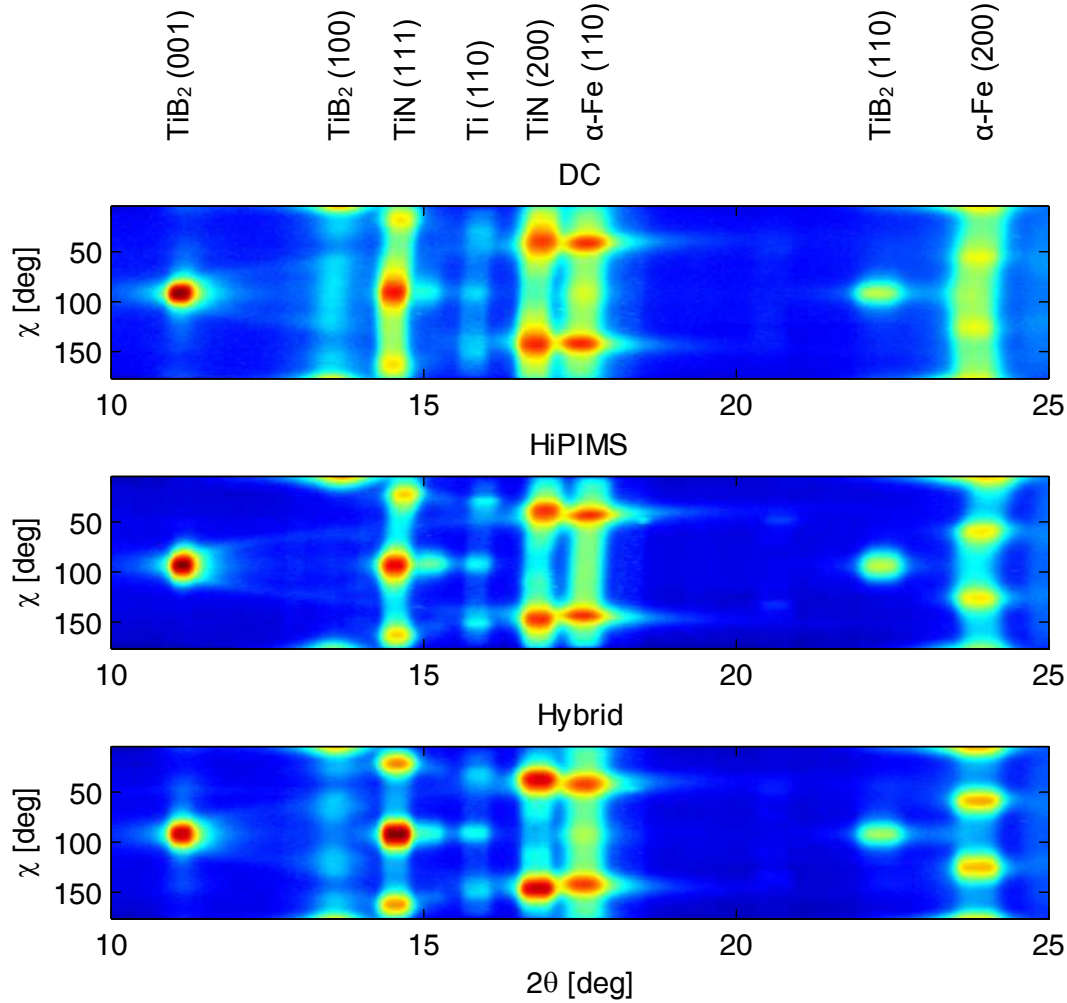
Figure 1: 2D-GIXRD measurements of TiB$_2$ coatings (λ = 0.6199 Å; E = 20 keV) with an angle of incidence of ω = 0.5° plotted as a function of the azimuth angle in dependency of the scattering angle 2Θ for a bias voltage of U$_B$ = -100 V

For a more detailed understanding of the evolution of the crystalline structure in dependency of the applied bias voltage and the used sputtering technology, the lattice parameter, and the strain values were calculated, as presented in Figure 2. For all TiB$_2$ coatings smaller values for the lattice parameters are observed in comparison to the standard reference value of c = 3.228 Å (JCPDS, 85-2083). Additionally, smaller differences in the lattice parameter between the deposited and the theoretical value can be correlated to the decrease of the measured strain in the coating systems, whereas no clear conclusions for the influence of the used PVD technology can be drawn. In contrast to these findings the applied bias voltage plays a decisive role for the crystalline structure and the considered parameters. Zhang et al. reported

a threshold for the bias voltage of U_B = -100 V which leads to a change of the crystalline growth mechanism [10]. For a low surface adatom energy, the dominant diffusion takes place along the planes but for a higher mobility of the species, the diffusion occurs among grains. This transition can be induced by the applied bias voltage but was not observed within this study due to the differences in the deposition temperature and the selected energy level of the sputtered species, which result in different strain levels.
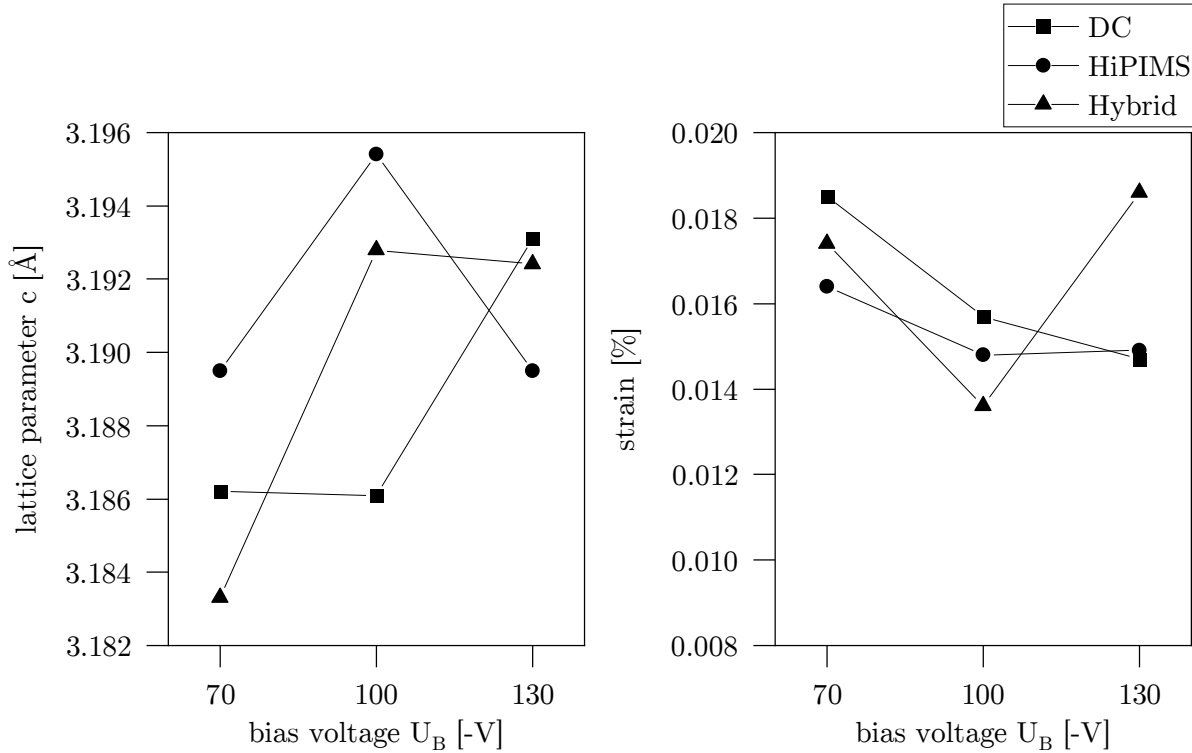
Figure 2: Calculated lattice parameter and strain of the TiB$_2$ thin films in dependency of the bias voltage and used power supply

The presented results prove the benefits of using DC/HiPIMS processes for the synthesis of TiB$_2$ coatings to influence the crystalline structure during the film growth. Further investigations have to be carried out to adjust the residual stresses and the crystalline growth by a time-resolved selective biasing of the metal ion flux avoiding the undesired Ar$^+$ afterglow of the HiPIMS discharges [6]. The implantation of noble gas leads to high residual stresses and a porous film growth limiting the application field of hybrid coating systems.

References

[1] Magnuson, M., Hultman, L., Högberg, H., Review of transition-metal diboride thin films, Vacuum (2021).

[2] Berger, M., Karlsson, L., Larsson, M., Hogmark, S., Low stress TiB$_2$ coatings with improved tribological properties, Thin Solid Films 401 (2001) 179–186.

[3]   Petrov, I., Hall, A., Mei, A.B., Nedfors, N., Zhirkov, I., Rosen, J., Reed, A., Howe, B., Greczynski, G., Birch, J., Hultman, L., Greene, J.E., Controlling the boron-to-titanium ratio in magnetron-sputter-deposited TiB x thin films, Journal of Vacuum Science & Technology A: Vacuum, Surfaces, and Films 35 (2017) 50601.

[4]   Prengel, H.G., Jindal, P.C., Wendt, K.H., Santhanam, A.T., Hegde, P.L., Penich, R.M., A new class of high performance PVD coatings for carbide cutting tools, Surface and Coatings Technology 139 (2001) 25–34.

[5]   D. Depla, S. Mahieu, J.E. Greene, in: P.M. Martin (Ed.), Handbook of Deposition Technologies for Films and Coatings, 2nd ed., Elsevier, Oxford, 2010, pp. 253–296.

[6]   Greczynski, G., Petrov, I., Greene, J.E., Hultman, L., Paradigm shift in thin-film growth by magnetron sputtering: From gas-ion to metal-ion irradiation of the growing film, Journal of Vacuum Science & Technology A 37 (2019).

[7]   Nedfors, N., Vozniy, O., Rosen, J., Effect of synchronized bias in the deposition of TiB 2 thin films using high power impulse magnetron sputtering, Journal of Vacuum Science & Technology A: Vacuum, Surfaces, and Films 36 (2018) 31510.

[8]   E. Kelesoglu, C. Mitterer, Structure and properties of TiB2 based coatings prepared by unbalanced DC magnetron sputtering, Surface and Coatings Technology 98 (1998) 1483–1489.

[9]   Losbichler, P., Mitterer, C., Non-reactively sputtered TiN and TiB2 films: Influence of Activation energy on film growth, Surface and Coatings Technology 97 (1997) 567–573.

[10] Zhang, T.F., Gan, B., Park, S., Wang, Q.M., Kim, K.H., Influence of negative bias voltage and deposition temperature on microstructure and properties of superhard TiB$_2$ coatings deposited by high power impulse magnetron sputtering, Surface & Coatings Technology 253 (2014) 115–122.

[11] Nedfors, N., Mockute, A., Palisaitis, J., Persson, P.O.Å., Näslund, L.-Å., Rosen, J., Influence of pulse frequency and bias on microstructure and mechanical properties of TiB$_2$ coatings deposited by high power impulse magnetron sputtering, Surface & Coatings Technology 304 (2016) 203–210.

[12] Berger, M., Coronel, E., Olsson, E., Microstructure of d.c. magnetron sputtered TiB$_2$ coatings, Surface & Coatings Technology 185 (2004) 240–244.

[13] Greczynski, G., Lu, J., Jensen, J., Bolz, S., Kölker, W., Schiffers, C., Lemmer, O., Greene, J.E., Hultman, L., A review of metal-ion-flux-controlled growth of metastable TiAlN by HIPIMS/DCMS co-sputtering, Surface & Coatings Technology 257 (2014) 15–25.

[14] Greczynski, G., Lu, J., Jensen, J., Petrov, I., Greene, J.E., Bolz, S., Kölker, W., Schiffers, C., Lemmer, O., Hultman, L., Strain-free, single-phase metastable Ti$_{0.38}$Al$_{0.62}$N alloys with high hardness: metal-ion energy vs. momentum effects during film growth by hybrid high-power pulsed/dc magnetron cosputtering, Thin Solid Films 556 (2014) 87–98.

[15] Greczynski, G., Lu, J., Johansson, M.P., Jensen, J., Petrov, I., Greene, J.E., Hultman, L., Role of Ti^{n+} and Al^{n+} ion irradiation (n=1, 2) during Ti$_{1-x}$Al$_x$N alloy film growth in a hybrid HIPIMS/magnetron mode, Surface & Coatings Technology 206 (2012) 4202–4211.

[16] Tillmann, W., Lopes Dias, N.F., Stangier, D., Tolan, M., Paulus, M., Structure and mechanical properties of hafnium nitride films deposited by direct current, mid-frequency, and high-power impulse magnetron sputtering, Thin Solid Films 669 (2019) 65–71.

[17] Xia, M., Ding, H., Zhou, G., Zhang, Y., Improvement of adhesion properties of TiB2 films on 316L stainless steel by Ti interlayer films, Transactions of Nonferrous Metals Society of China 23 (2013) 2957–2961.

[18] Hammersley, A.P., Svensson, S.O., Thompson, A., Calibration and correction of spatial distortions in 2D detector systems, Nuclear Instruments and Methods in Physics Research 346 (1994) 312–321.

[19] Williamson, G.K., Hall, W.H., X-ray line broadening from filed aluminium and wolfram, Acta Metallurgica 1 (1953) 22–31.

[20] Quaeyhaegens, C., Knuyt, G., D'Haen, J., Stals, M., Experimental study of the growth evolution from random towards a (111) preferential orientation of PVD TiN coatings, Thin Solid Films 258 (1995) 170–173.

[21] Abadias, G., Stress and preferred orientation in nitride-based PVD coatings, Surface & Coatings Technology 202 (2008) 2223–2235.

[22] Pelleg, J., Sade, G., Sinder, M., Mogilyanski, D., Compositional and structural changes in TiB2 films induced by bias, in situ and post-deposition annealing, respectively, Physica B: Condensed Matter 381 (2006) 118–127.

Oxidation formation in thermally treated and recycled steel feedstock powders

A. Röttger,[1] Felix Großwendt,[2] J.T. Sehrt,[3] N. Hantke,[3] M. Paulus,[4] and C. Sternemann[4]

[1]Neue Fertigungstechnologien und Werkstoffe, Bergische Universität Wuppertal, Bahnhofstraße 15, D-42651 Solingen,

[2]Lehrstuhl Werkstofftechnik, Ruhr-Universität Bochum, Universitätsstraße 150, D-44801 Bochum

[3]Lehrstuhl für Hybrid Additive Manufacturing, Ruhr-Universität Bochum, Universitätsstraße 150, D-44801 Bochum,

[4]Fakultät Physik/DELTA, Technische Universität Dortmund, Maria-Goeppert-Mayer-Str. 2, D-44227 Dortmund

Additive manufacturing using powder bed fusion-laser beam/metal (PBF-LB/M) has reached market maturity within the last decade. In the PBF-LB/M process, a loose powder layer is applied, and then the cross-sectional areas of the parts are locally melted by laser radiation, taking into account optimized exposure parameters and CAD-data. Because of this layer upon layer built up process, complex-shaped and individualized parts with internal cavities can be processed, which are currently used in medical technology, avionic and mechanical engineering. During the remelting process of the powder material, the generated melt pool reacts with the residual oxygen of the surrounding atmosphere. Simultaneously, heat is introduced into the powder particles lying next to the melt pool, resulting in powder oxidation [1]. The oxidation kinetics and the formed phases are determined by the chemical composition, the particles' specific surface area, and the time-temperature characteristic during PBF-LB/M processing. According to Yan et al. [2], the oxide films on the powder surfaces are melted during PBF processing due to the high temperatures and metastable oxides (in the case of the steel AISI 316L, e.g., $MnSiO_3$) with a spherical shape being formed during the solidification process. These nano-inclusions can form at grain boundaries and act as Zener-pinning particles, improving the material's strength [3]. Otherwise, Powel et al. state that the decrease in the necessary powder properties (flowability, amount of contamination) resulting from repeated reuse is a common problem. Parts made from highly recycled powders tend to be of poorer quality, which ultimately makes the powder unusable in additive manufacturing [4]. The literature also reported that oxidized metal surfaces are characterized by improved laser absorption [5]. Because the heated but not yet remelted powders oxidize and the laser couples more intensely into these oxidized powders, the exposure parameters have to be adapted to the degree of oxidation of the powder in order to produce defect-free parts. In other words, because of powder oxidation, the reuse of the powder is only possible to a limited extent. Hence, understanding the oxidation behavior of this material is of high relevance to optimize recycling strategies and to adapt the exposure parameters on the oxidation state; thus defect-free parts can be produced.

For this purpose, we studied the oxide formation by X-ray diffraction of recycled AISI 316L steel powders, i.e., ranging from the native powder up to 39 cycles, and investigated the directed oxidation of powders exposed to a temperature of 650 °C in an inert helium atmosphere and air. All samples were measured at beamline BL9 of the DELTA synchrotron radiation source exploiting the wide-angle X-ray diffraction setup at an incident energy of 20 keV and a beam size of 1x1 mm². The powder samples were filled into glass capillaries which were rotated during the measurements while the diffraction data were collected using a MAR345 image plate detector. However, due to the large grain size, an adequate powder average was not obtained, which complicated the phase analysis using the Match! software package.

The integrated diffraction patterns of the native and annealed powders are presented in figure 1. Austenite (γ-Fe) is the dominating phase in all samples with a contribution larger than 98 weight percent. This is assigned to the fast solidification of the small particles during the gas atomization process so that the thermodynamically stable ferrite (α-Fe) formation is suppressed. Annealing in an inert gas atmosphere induces the formation of magnetite/chromite-type oxides while the ferrite contribution persists. The occurrence of oxides after annealing in helium indicates the presence of X-ray amorphous oxide surface layers in the native and recycled powders. In contrast, hematite is formed during annealing in air. This is accompanied by the vanishing phase contribution of ferrite and infers a predominant oxidation of ferrite particles. Figure 2 shows the ferrite content of the reused powders after different
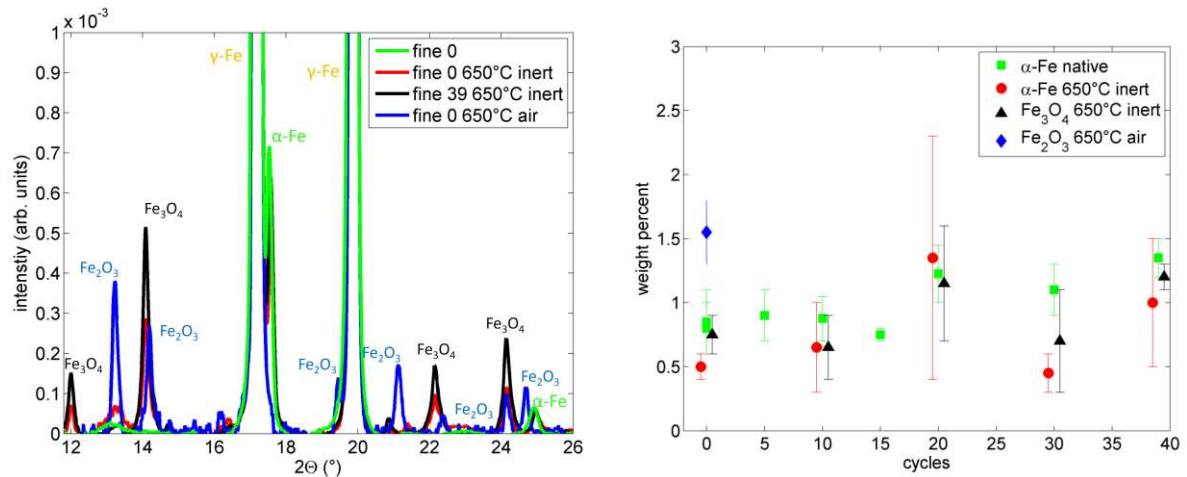
Figure 2: Typical diffraction patterns – here zoomed to highlight the minority phases - of native and recycled ASIS 316L powder annealed in inert helium atmosphere and in air at 650°C (left). The diffraction peaks are assigned to the identified phases hematite, magnetite/chromite, ferrite, and austenite (Fe_2O_3, Fe_3O_4/Cr_2FeO_4, α-Fe and γ-Fe). All samples contained dominant contribution of γ-Fe (> 98 weight percent). Phase composition determined via Rietveld-refinement (right).

reuse cycles in the case of coarse and fine powders. Crystalline oxide phases were not observed. While the data of the coarse powder is challenging to interpret due to strong single-crystalline Bragg reflections in the diffraction patterns, the fine powders show an increase in ferrite content with the number of reuses. Although at the limit of the accuracy of the experiment and precision of the data analysis, this increase might be traced back to the small emergence of larger particles with the reuse of the AISI 316L powders. This will be the subject of further investigation. It is striking that the formation of oxides significantly, as observed in the study, affects the reflectivity of the powders in the order of 10 %. This is sufficient to influence the laser-powder interaction during PBF-LB/M and thus strongly affects their processability or, at least, their processing parameters.
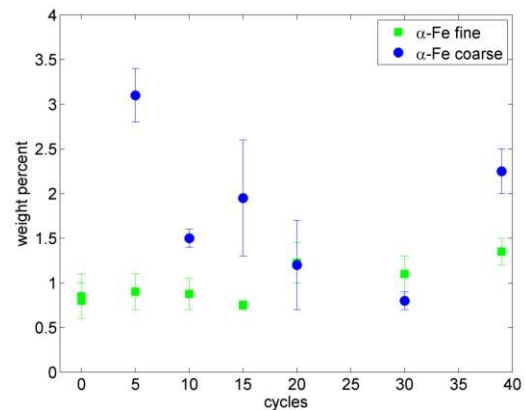
Figure 1: Results of the phase analysis of coarse and fine ASIS 316L powders after different reuse cycles.

References

[1]   P. Deng, M. Karadge, R. B. Rebak, et al.: The origin and formation of oxygen inclusion in austenitic stainless steels manufactured by laser powder bed fusion, Additive Manufacturing, 35 (2020), pp. 101334

[2]   F. Yan, W. Xiong, E. Faierson, et al.: Characterization of nano-scale oxides in austenitic stainless steel processed by powder bed fusion, Scripta Materialia, 155 (2018) pp. 104-108

[3]   X. Lou, P. L. Andresen, R. B. Rebak: Oxide inclusion in laser additive manufactured stainless steel and their effects on impact toughness and stress corrosion cracking behavior, J. of Nucl. Mat., 499 (2018), pp. 182-190

[4]   D. Powell, A. E. W. Rennie, L- Geekie, et al.: Understanding powder degeneration in metal additive manufacturing to allow the upcycling of recycled powders, J. of Cleaner Prod., 268 (2020), pp. 122077

[5]   J. Xie: Laser welding of sheet metals, Dissertation, University of Central Florida (1998)

Acknowledgments

An X-ray diffraction study on AlCrVY(O)N thin films

Eric Schneider[1], David Kokalj[2], Steffen Bieder[1], Gordon Scholz[1], Mike Moron[1], Dominik Birkwald[1], Nicola Thiering[1], Christian Sternemann[1], Michael Paulus[1], Dominic Stangier[2], Wolfgang Tillmann[2]

[1]Fakultät Physik/DELTA, TU Dortmund University, 44221 Dortmund, Germany; [2]Fakultät Maschinenbau, Institute of Materials Engineering, TU Dortmund University, 44221 Dortmund, Germany

In materials science, major efforts are made to optimize tool coatings for use at elevated process temperatures. The reason for this is a focus on dry machining or machining with minimum quantity lubrication. Thus, depending on the material and tool design such as the shape of the cutting edge, temperatures between 300°C and 1000°C can occur during turning operations [1]. In order to enable machining of high-strength materials with such tools, the high-temperature properties of the tool coatings must be optimized. AlCrVY(O)N thin films are potential candidates for such an application. The primary goal of this project is to gain a fundamental understanding of the dependence between deposition parameters, coating structure, and oxidation behaviour.

For the X-ray diffraction (XRD) studies, AlCrVY(O)N thin films were deposited on WC-Co substrates using a DC magnetron sputtering device with the application of different deposition parameters such as bias voltage, heating power, and coating architecture. Furthermore, a graded yttrium content was used to analyse the influence of yttrium on the oxidation behaviour of the coating. During the measurements, the coated WC-Co substrate was heated stepwise in an Anton-Paar heating cell. The temperature range covered was between 25°C and 1050°C. Figure 1 shows the setup used at beamline BL9 at DELTA. The X-ray beam had an energy of 27 keV and a size of 1.5 x 0.1 mm^2 (v x h). The scattered radiation was detected by a MAR345 image plate detector.
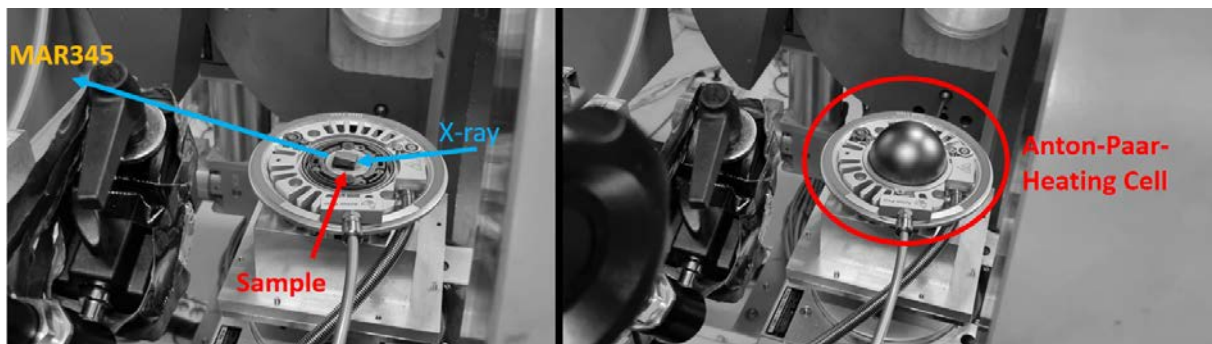

Figure 1: Anton-Paar heating-setup at beamline BL9. Left: Without graphite dome with installed sample. Right: After installation of the graphite dome for heating above 300 °C.

An initial evaluation of the data shows clear dependency on the manufacturing parameters of both the thermal stability of the samples and the occurrence of residual stresses in the layer. As an example, the comparison between samples produced with different bias voltages (-120 V and -200 V) is presented in Figure 2. We observe less textured Bragg reflections of the WC in contrast to highly textured reflections of the layer. Furthermore, the relatively weak and azimuthally inhomogeneous signal of the Co matrix in which the WC is embedded can be seen. The layer prepared at a bias voltage of -200 V has a stronger texture while the widths of the Bragg reflections is significantly increased, most prominent for larger scattering angles, indicating larger residual stresses within the layer. Latter is even more evident when the scattering intensity of both samples is plotted as a function of 2θ as shown in Figure 3. In this case, the diffraction images were integrated either in the horizontal or in the vertical scattering plane. The shift of the CrN (222) reflection clearly shows the presence of residual stress. A comparison of samples that have been heated to a temperature of 1050 °C is shown in Figure 3 (right). One sample was deposited using an alloyed AlCrV target and a bias voltage of -200 V. In

contrast, the other thin film was deposited using individual AlCr, V, and Y targets resulting in a nanolayerd structure. Both samples show the formation of oxides most prominent at small scattering angles. However, these appear to have different crystalline structures depending on the sample preparation. The evaluation of the whole data set is still in progress.
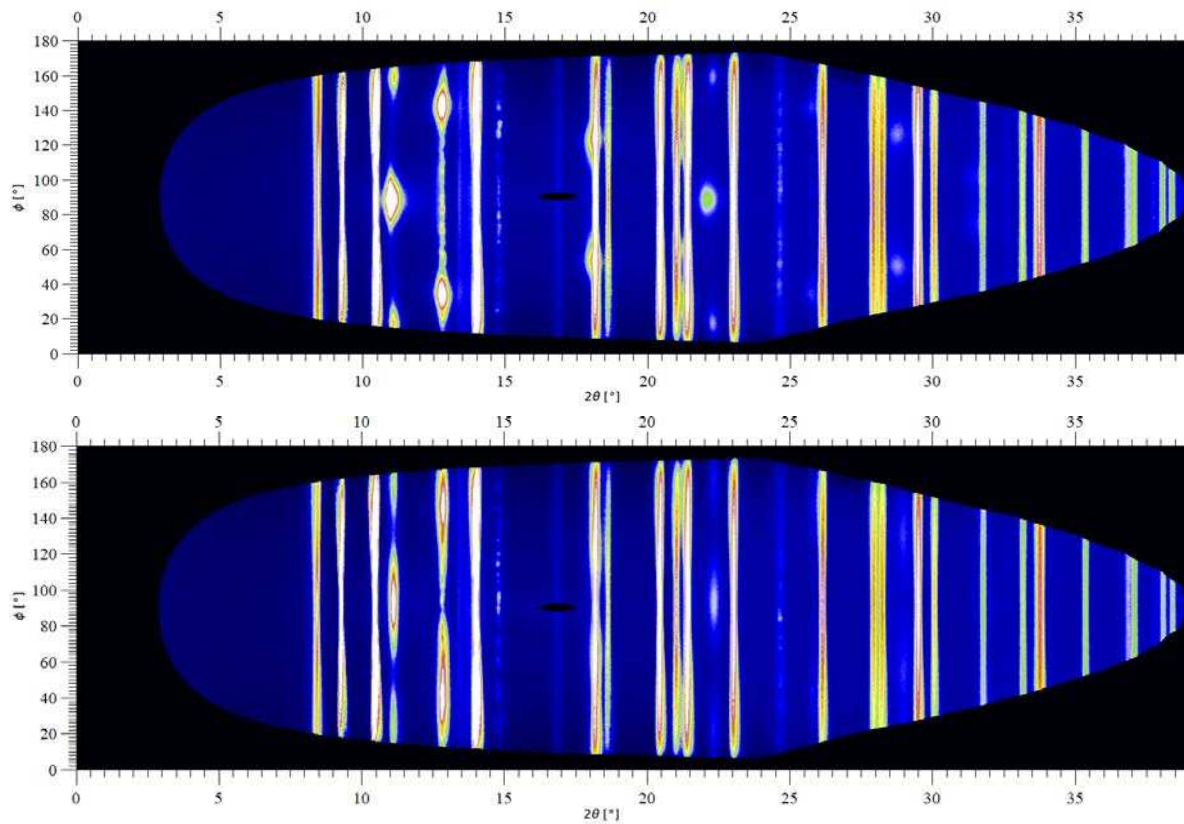
Figure 2: Diffractograms of the two samples prepared with different bias voltage. Top U=200 V, bottom U=120 V. The scattering intensity is plotted as a function of the azimuth angle φ and the scattering angle 2θ.
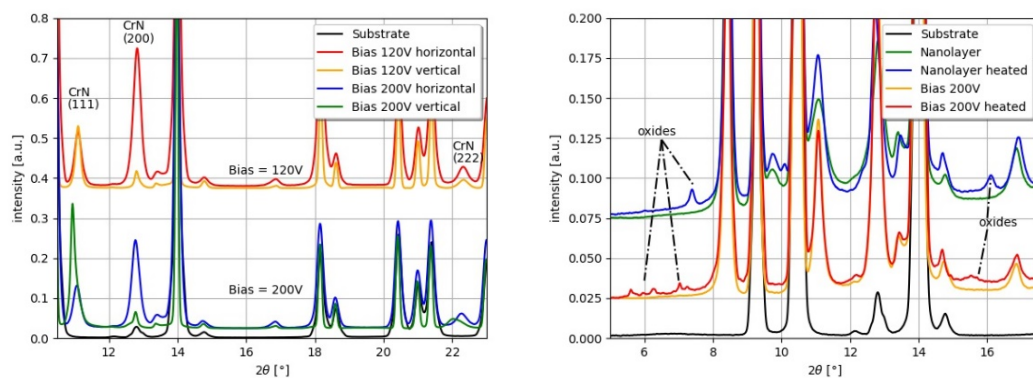
Figure 3: Left: Comparison of two samples produced with different bias voltage. Right: Comparison of a sample produced at bias voltage of 200 V and a sample that exhibits an internal layer structure before and after annealing.

References

[1]   K.-M. Li, S.Y. Liang, Modeling of Cutting Temperature in Near Dry Machining, J. Manuf. Sci. Eng. 128 (2006) 416–424. https://doi.org/10.1115/1.2162907.

Acknowledgments

Investigating the thermo-responsive breathing behaviour of ZIF-7 and ZIF-9

Athanasios Koutsianos, Roman Pallach, Sebastian Henke*

Anorganische Chemie – TU Dortmund, Otto-Hahn-Str. 6, 44227 Dortmund

Scientific Context

Porous metal imidazolate frameworks, also known as zeolitic imidazolate frameworks (ZIFs), constitute a major class of metal-organic frameworks (MOFs).[1, 2, 3] Distinct from their zeolite analogues, some ZIFs exhibit extraordinary framework flexibility in the presence of external stimuli. The archetypal flexible ZIF-7 (Zn(benzimidazolate)$_2$, **sod** topology) undergoes a phase transition from a nearly nonporous (narrow pore, *np*) to a porous phase (large pore, *lp*) upon adsorption of guest molecules.[4] For its cobalt analogue ZIF-9 (Co(benzimidazolate)$_2$) a similar *np*-to-*lp* phase transition has been reported upon adsorption of CO_2 and CH_4, as opposed to N_2.[5, 6] Besides guest adsorption, heating can also induce the structural transformation of ZIF materials in the absence of any guest molecules.[7] For ZIF-7, a *np*-to-*lp* phase transformation has been reported at a temperature close to 500°C under 1 bar N_2.[7]

In contrast, the structural evolution of the isoreticular ZIF-9 material regarding temperature has not been investigated to date. Initially, calorimetric studies have been performed by means of differential scanning calorimetry (DSC) and displayed endothermic signals for both materials at temperatures around 500 °C (Figure 1). Specifically, the DSC curve of ZIF-7 during a dynamic heating program (+10 °C min^{-1}, N_2 atmosphere) presents an endothermic peak with an onset temperature of ca. 430 °C. In the case of ZIF-9 a deflection from the baseline is observed at an elevated temperature of ca. 500 °C. This

Figure 1: DSC data for the activated ZIF-7 and ZIF-9 materials.

endothermic signal in the DSC of ZIF-9 suggests a *np*-to-*lp* phase transition similar to ZIF-7 is triggered.

Thus, variable temperature powder X-ray diffraction (VT-PXRD) was used to study ZIF-9 *in situ* and to compare its behaviour with its congener ZIF-7.

Experimental procedure

VT-PXRD was performed at Beamline 9 of DELTA (Dortmund, Germany) with a monochromatic X-ray beam (λ= 0.6199 Å) using a MAR345 image plate detector. The investigated temperature ranged from 25 °C to 464 °C and 475 °C, for ZIF-7 and ZIF-9; respectively. Finely ground samples were sealed in quartz glass capillaries under N_2 atmosphere, placed on an Anton Paar DHS1100 hot stage and heated under a polyether ether ketone (PEEK) dome. Temperature calibration of the hot stage was performed by reference VT-PXRD measurements of a silicon standard.

Results

Figure 2: **Left,** VT-PXRD patterns at selected temperatures for the activated ZIF-7 and ZIF-9 materials. **Right,** contour plots displaying data from the whole temperature range from 25 to 464 °C (ZIF-7) and from 25 to 475 °C (ZIF-9).

VT-PXRD data indeed shows a structural transformation of ZIF-9 upon heating (Figure 2). In agreement with the DSC data, the transformation occurs at a slightly higher temperature compared to its Zn 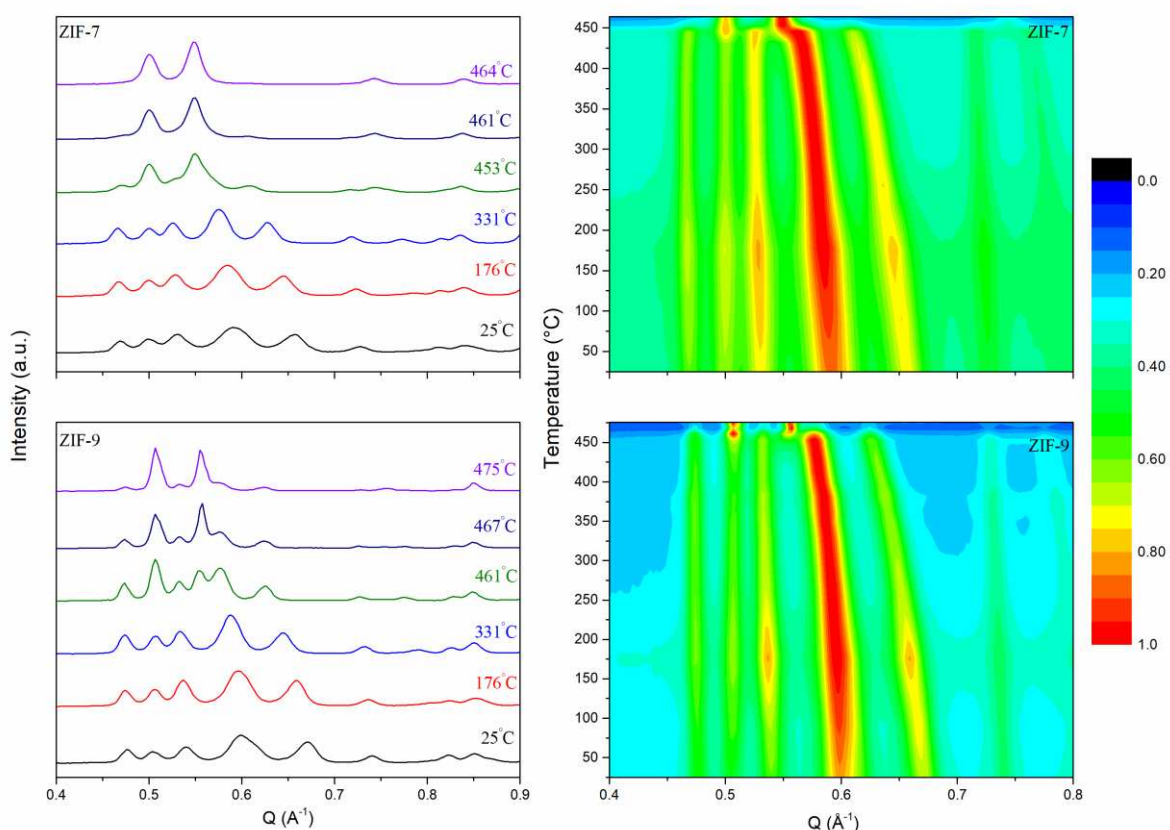analogue ZIF-7. For ZIF-9, the transition starts at about 461 °C and is almost completed at 475 °C. ZIF-7, meanwhile, starts to transform from 453 °C, with the transition being completed at 464 °C. The observed changes for both materials match well with the reported changes ascribed to the thermal *np*-to-*lp* phase transition of ZIF-7.[7, 8] The full dataset of the collected in situ PXRD data for ZIF-7 and ZIF-9 are also displayed in contour plots (Figure 2). A zoom into the region between $Q = 0.4$ and 0.8 Å^{-1} is plotted to highlight the dominant diffraction lines and their evolution. In the case of ZIF-9, the first three *np* diffraction lines remain at their position, whereas the two diffraction lines at $Q = 0.6$ and and 0.66 Å^{-1} show larger shifts to lower angles demonstrating the strong thermal expansion of the *np* phase towards the *lp* phase of ZIF-9. At a temperature around 450 °C the phase transition to the *lp* phase takes place with the diffraction lines being initially observed at 0.47, 0.53 and 0.67 Å^{-1} disappearing.[7] As expected, ZIF-7 exhibits a similar behaviour with the transition being noticed at a slightly lower temperature.

In summary, BL9 enabled us to monitor the phase transformation of structurally flexible ZIF-9 and ZIF-7 materials, which helps with the interpretation of the calorimetric measurements and will allow us to extract information on the thermal expansion behaviour of both phases involved.

References

1. Iacomi P, Maurin G. ResponZIF Structures: Zeolitic Imidazolate Frameworks as Stimuli-Responsive Materials. *ACS Applied Materials & Interfaces* 2021, **13**(43)**:** 50602-50642.

2. Huang X, Zhang J, Chen X. [Zn(bim)2] · (H2O)1.67: A metal-organic open-framework with sodalite topology. *Chinese Science Bulletin* 2003, **48**(15)**:** 1531-1534.

3. Park KS, Ni Z, Côté AP, Choi JY, Huang R, Uribe-Romo FJ*, et al.* Exceptional chemical and thermal stability of zeolitic imidazolate frameworks. *Proceedings of the National Academy of Sciences* 2006, **103**(27)**:** 10186-10191.

4. Aguado S, Bergeret G, Titus MP, Moizan V, Nieto-Draghi C, Bats N*, et al.* Guest-induced gate-opening of a zeolite imidazolate framework. *New Journal of Chemistry* 2011, **35**(3)**:** 546-550.

5. McGuirk CM, Runčevski T, Oktawiec J, Turkiewicz A, Taylor MK, Long JR. Influence of Metal Substitution on the Pressure-Induced Phase Change in Flexible Zeolitic Imidazolate Frameworks. *Journal of the American Chemical Society* 2018, **140**(46)**:** 15924-15933.

6. Noguera-Díaz A, Villarroel-Rocha J, Ting VP, Bimbo N, Sapag K, Mays TJ. Flexible ZIFs: probing guest-induced flexibility with CO2, N2 and Ar adsorption. *Journal of Chemical Technology & Biotechnology* 2019, **94**(12)**:** 3787-3792.

7. Du Y, Wooler B, Nines M, Kortunov P, Paur CS, Zengel J*, et al.* New High- and Low-Temperature Phase Changes of ZIF-7: Elucidation and Prediction of the Thermodynamics of Transitions. *Journal of the American Chemical Society* 2015, **137**(42)**:** 13603-13611.

8. Cai W, Lee T, Lee M, Cho W, Han D-Y, Choi N*, et al.* Thermal Structural Transitions and Carbon Dioxide Adsorption Properties of Zeolitic Imidazolate Framework-7 (ZIF-7). *Journal of the American Chemical Society* 2014, **136**(22)**:** 7961-7971.

Hard X-ray spectroscopy

In-Situ observation of ZnO nanoparticle growth by a combination of time-resolved EXAFS and XRD

F. Eckelt[a], R. Wagner[a], D. Lützenkirchen-Hecht[a], A. Šarić[b], M. Vrankić[b], R. Frahm[a]

[a] Department of Physics, Bergische Universität Wuppertal, Gaußstraße 20, 42097 Wuppertal, Germany
[b] Division of Materials Physics, Ruđer Bošković Institute, Bijenička 54, 10002 Zagreb, Croatia

Due to their photo-, thermal- and chemical stability, low toxicity, biocompatibility and low cost, zinc oxide nanoparticles are widely used materials with applications in quite different fields such as catalysis, electronics, energy harvesting, cosmetics and biomedicals. Several experimental works have shown that all the details of the different available synthesis routes have a strong impact on the resulting morphology and the physico-chemical properties of the prepared ZnO nanomaterials, indicating that many details of the ZnO growth processes are not yet understood. We have therefore conducted simultaneous time-resolved in-situ EXAFS and XRD studies during the hydrothermal preparation of ZnO nanoparticles in the liquid phase.

For the synthesis we have employed Zinc acetylacetonate monohydrate ($Zn(C_5H_7O_2)_2H_2O$), sodium hydroxide (NaOH), 1-octanol ($CH_2(Ch_2)_7OH$) and distilled water as starting materials for the synthesis, which were headed under continous stirring. In a typical synthetic procedure zinc acetylacetonate monohydrate in desired amounts were mixed with water, aqueous NaOH solution or 1-octanol following the procedure described by Šarić et al. [1].
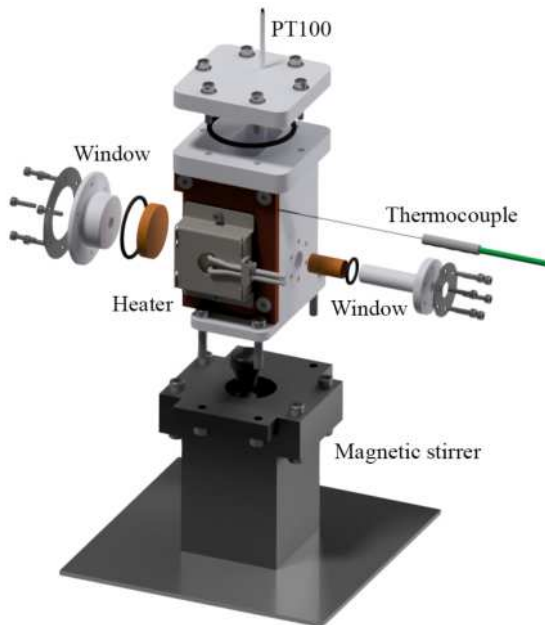

Figure 1: Explosive isometry of the cell with the essential components.

The cell developed by us, in which the measurements were carried out, is shown with its essential components in Figure 1. The cell consists of a PTFE container in which the liquid is filled. A heater attached to the side can heat the sample to more than 200 °C. A PT100 encased in PTFE measures the sample temperature. The X-ray beam passes through the sample through two Kapton windows. These consist of two inserts, which are covered with Kapton foil and screwed to the cell with Viton seals. The Kapton film is $25\,\mu m$ thick and has a special, temperature and chemical resistant adhesive. The effective sample thickness can be varied by using inserts of different lengths. The insert for the beam exit conically opens outwards so as not to cut off the X-ray diffraction signals. In order to guarantee a homogenous temperature distribution within the cell and to avoid precipitation on the walls and windows, a magnetic stirrer controlled via a brushless motor in the cell holder was employed. The stirrer as well as the control of the heater and the temperature readouts are remote-controlled via a Raspberry Pi with Ethernet connection. The presented data has been measured using a Si(111) channel-cut monochromator together with N2- and Ar-filled ionization chambers for incident an transmitted intensities.
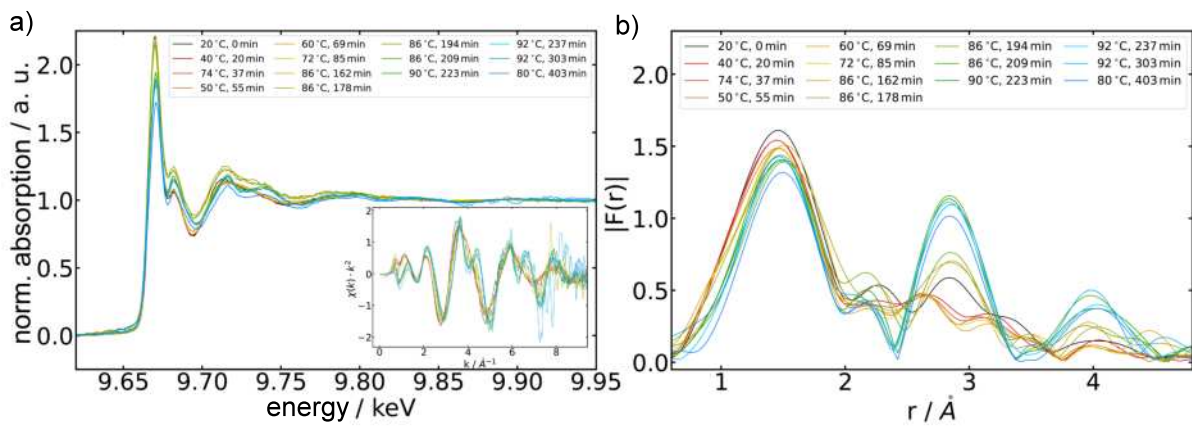
Figure 2: a) Normalized absorption spectra and EXAFS of sample 17. b) Fourier transform of the k^2-weighted EXAFS of sample 17.

Figure 2a shows the normalized absorption spectra and EXAFS of sample 17 (NaOH) at different sample temperatures in the course of the reaction. The change in the spectra with increasing sample temperature and time can be clearly seen. A clear change can also be seen in the Fourier-transformed EXAFS (Figure 2b). The first peak represents the Zn-O-shell and changes only slightly when the sample temperature is increased. The second peak can be assigned to the Zn-Zn-coordination shell. The increase in intensity is a clear indication for the formation of ZnO in the sample. All samples generated were extracted after the synthesis and measured ex-situ. The data generated in this way were fitted with a hexagonal ZnO structure using the Artemis software [2]. With the aid of the fit carried out in the ex situ measurement and the measured spectrum of the Zn(acac)$_2$ powder sample, linear combination fits (LCF) of the measured spectra were then carried out. This allows the phase proportion of the respective component in the measured sample volume to be determined. The phase proportions of the Zn(acac)$_2$ and ZnO phases in sample 17 are shown in Figure 3. It can be clearly seen that the ZnO phase proportion increases significantly from a temperature of about 70 °C and the Zn (acac) phase is correspondingly reduced.
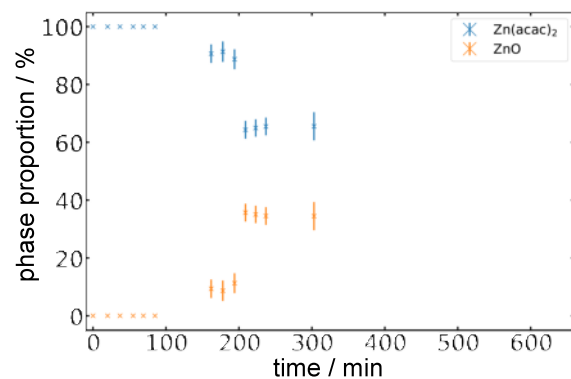
Figure 3: Results of the LCFs of sample 17.

All the different sample systems show a similar course, with the ZnO phase proportion in the 1-octanol samples being significantly higher at up to 90 %. A significant proportion of ZnO could be detected in the 1-octanol samples even without temperature treatment. In addition, in-situ XRD measurements carried out at DESY in Hamburg have also shown that many and small ZnO-particles arise in the 1-octanol samples compared to the NaOH samples. Moreover, no further phases can be identified in the XRD measurements, which is why the LCF was only carried out with the initial and final product. The data obtained suggest growth according to the LaMer model with subsequent diffusion [3].

References

[1] S. Musić, A. Šarić, „Formation of hollow ZnO particles by simple hydrolysis of zinc acetonate", Ceram. Int. (2012) 38, 6047-6052

[2] B. Ravel and M. Newville. ATHENA and ARTEMIS interactive graphical data analysisusing IFEF-FIT. Physica Scripta, page 1007, 2005.

[3] V. K. LaMer and R. H. Dinegar. Theory, production and mechanism of formation of monodispersed hydrosols. Journal of the American Chemical Society, 72(11):4847–4854, 1950.

On the relationship between structure and oxidation behavior of magnetron sputtered cubic and hexagonal MoN$_x$ thin films

Wolfgang Tillmann[1], David Kokalj[1*], Dominic Stangier[1],

Christian Sternemann[2], Michael Paulus[2]

Ralph Wagner[3], Dirk Lützenkirchen-Hecht[3]

[1]Institute of Materials Engineering, TU Dortmund University, Germany

44227 Dortmund, Leonhard-Euler-Straße 2

[2]Experimental Physics 1 / DELTA, TU Dortmund University, Germany

44227 Dortmund, Maria-Goeppert-Mayer-Straße 2

[3]FK4-Condensed Matter, Wuppertal University, Germany

42119 Wuppertal, Gaußstraße 20

* corresponding author: david.kokalj@tu-dortmund.de

For highly stressed surfaces, especially for forming or cutting tools enhanced service times and lower frictional forces are required, which can be met by means of thin-film technology. Tools being used in current machining strategies, like dry or high-speed machining, suffer from the high coefficient of friction of conventional coatings leading to fatigue as well as tribo-oxidation processes and in turn lower service times [1,2]. Aside from a high hardness, a sufficient level of ductility is required for thin films used in tribological applications [3]. In general, materials showing a high valence electron concentration can provide an increased toughness [4] and hence, group VI nitrides (Cr-N, Mo-N, W-N) should be more suitable for such applications compared to group IV (Ti-N, Zr-N, Hf-N) and group V (V-N, Nb-N, Ta-N) nitrides [5].

Molybdenum nitride is particularly promising in this regard, as it belongs to the group VI nitrides and can additionally crystallize in a variety of different crystal structures, such as cubic γ-Mo$_2$N, tetragonal β-Mo$_2$N, and hexagonal δ-MoN [6,7]. MoN$_x$ thin films are used as catalysts [8,9], tribological coatings [10–12], diffusion barriers [13], and superconductors [14,15] in dependence of the structure. Regarding tribological properties, MoN$_x$ thin films offer low wear rates and friction coefficients, compared to other nitride thin films [12,16,17].

Especially the low friction coefficient can be ascribed to the formation of lubricous oxides, so-called Magnéli phases, when exposed to elevated temperatures [18]. The Magnéli phases can emerge in the series of Mo$_n$O$_{3n-1}$ [19], showing oxidation states ranging from +2 to +6. In case of molybdenum, MoO$_2$ and MoO$_3$ are the most investigated molybdenum oxides [20].

However, investigations concerning the oxidation resistance of MoN$_x$ thin films can be hardly found [21,22]. It is stated the oxide formation is a complex mechanism, revealing a layered structure of MoO$_3$ on the surface and several other molybdenum oxides between MoO$_3$ and the MoN$_x$ thin film. Summarized, there is still a lack concerning the dependence of the formation of molybdenum oxides on the structure of the molybdenum nitride thin film. Therefore, this investigation covers the influence of the deposition parameters on the structural, mechanical, as well as the oxidation behavior of cubic and hexagonal MoN$_x$ thin films.

The MoN$_x$ thin films were synthesized by means of DC magnetron sputtering, while varying the bias-voltage U$_B$ and substrate temperature T$_S$ in order to control the physical structure of the thin films (S1: U$_B$ = -55 V, T$_S$ = 450 °C; S2: U$_B$ = -75 V, T$_S$ = 450 °C; S3: U$_B$ = -125 V, T$_S$ = 450 °C; S4: U$_B$ = -55 V, T$_S$ = 320 °C; S5:U$_B$ = -125 V, T$_S$ = 320 °C).

The phase analysis was performed at the beamline BL9 by means of GI-XRD (Grazing Incidence X-ray Diffraction) using a photon energy of 13 keV (λ = 95.370 pm) at an angle of incidence of 1.0 degree. The samples were in-situ heated to 250 °C, 400 °C, 550 °C and 700 °C in air atmosphere using a DHS1100 heating-table (Anton Paar, Austria). For photon detection a Pilatus

100K detector (Dectris, Switzerland) was used. The plotted diffraction pattern were converted to a wavelength of $\lambda = 154.1$ pm (Cu-Kα_1).

At BL8, XANES (X-ray absorption near edge structure) and EXAFS (extended X-ray absorption fine structure) experiments were performed at the molybdenum K-edge (20,000 eV) at an angle of incidence of 3°, to determine the oxidation state of the thin films in dependence of the temperature. A Forward Fourier transform of $\chi(k)$ was performed on the k-range from 5 Å^{-1} to 12 Å^{-1} with a Hanning window function using a tapering parameter of dk = 0.8.A more detailed explanation of the deposition parameters, the magnetron-sputtering device, the substrate material and the characterization methods is presented in [23].

The XRD experiments prove the metastable cubic MoN phase for lower bias-voltages (Fig. 1a-e). For a high bias-voltage of -125 V, the thin films S3 and S5 are crystallized in a two-phase structure composed of the over stoichiometric cubic B1-NaCl and hexagonal MoN$_x$ phases. The ratio of the δ-MoN phase is increased for the lower substrate temperature. Summarized, the orientation and phase composition of the thin films in the as-deposited state can be controlled by the bias-voltage and substrate temperature.
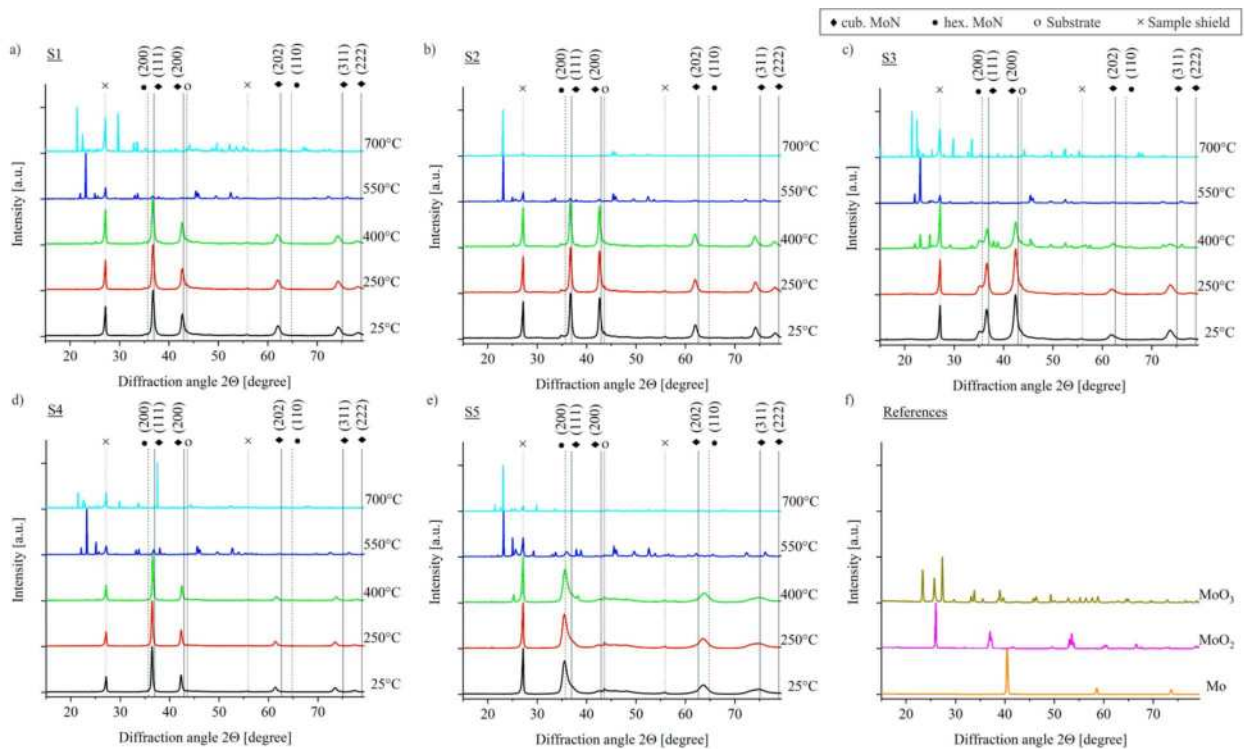

Fig. 1: GI-XRD pattern of the in-situ experiments of a)-e) the MoN$_x$ thin films in dependence of the temperature and f) the references [23]

In the next step, the impact of the phase composition on the oxidation behavior was investigated by means of in-situ XRD (Fig. 1a-e). Below 400 °C, no distinct oxide phases were formed for all thin films. At 400 °C first oxide phases were detected for the two-phase structured thin films S3 and S5. However, the intensity of the reflections of the oxides is higher for the thin film S3, which contains a higher amount of the cubic MoN$_x$ phase. The reflections can be assigned to MoO$_3$ in orthorhombic (symbol ∇) and monoclinic (symbol $\blacktriangledown$) structure, as well as to hexagonal MoO$_2$ (symbol Δ). An increase of the temperature to 550 °C leads to the formation of the Magnéli-phases Mo$_9$O$_{26}$/Mo$_8$O$_{23}$ respectively Mo$_4$O$_{11}$ at 700 °C (Fig. 2).

For a deeper insight into the Mo oxidation state of the thin films, XANES was performed in dependence of the temperature. It was proven, that the thin films deposited with a low bias-voltage reveal a higher oxidation state in the initial state compared to the thin films deposited with a bias-voltage of -125 V (Fig. 3a). At 400 °C all thin films reveal an increased oxidation state (Fig. 3b). Combining the results of XRD and XANES, it can be stated the molybdenum oxides are

mainly in amorphous state. For a higher temperature of 550°C, the lowest oxidation state was confirmed for the thin film S5, which contains the highest proportion of the δ-MoN phase (Fig. 3c). At 700 °C, the MoN_x thin films show similar oxidation states between 5.7 and 6.0 (Fig. 3d), covering the range between the Mo Magnéli-phases and MoO_3. The corresponding Fourier transforms visualize the change of the Mo local environment by variations in the Mo-N, Mo-Mo, and Mo O single and multiple scatterings paths (Fig. 4). Further and more detailed information is published in [23].

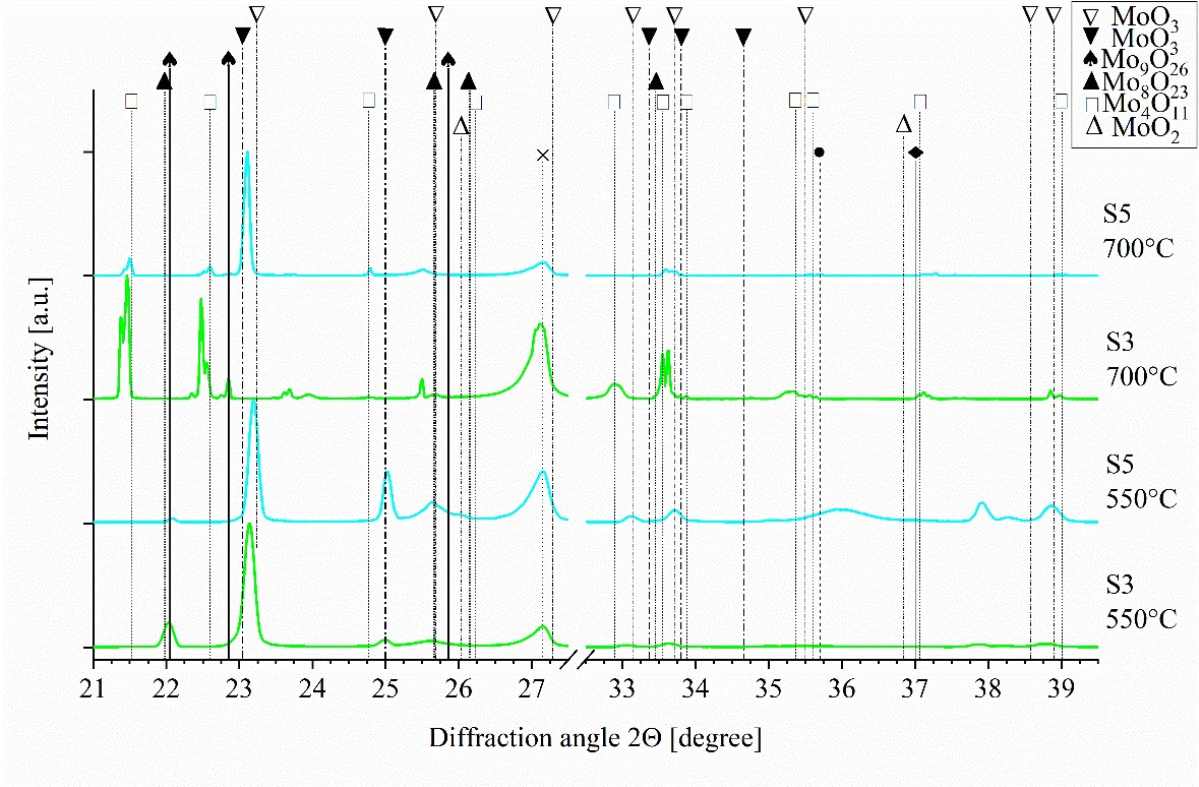Fig. 2: Detailed GI-XRD pattern of the MoN_x thin films S3 and S5 at 550 °C and 700 °C [23]
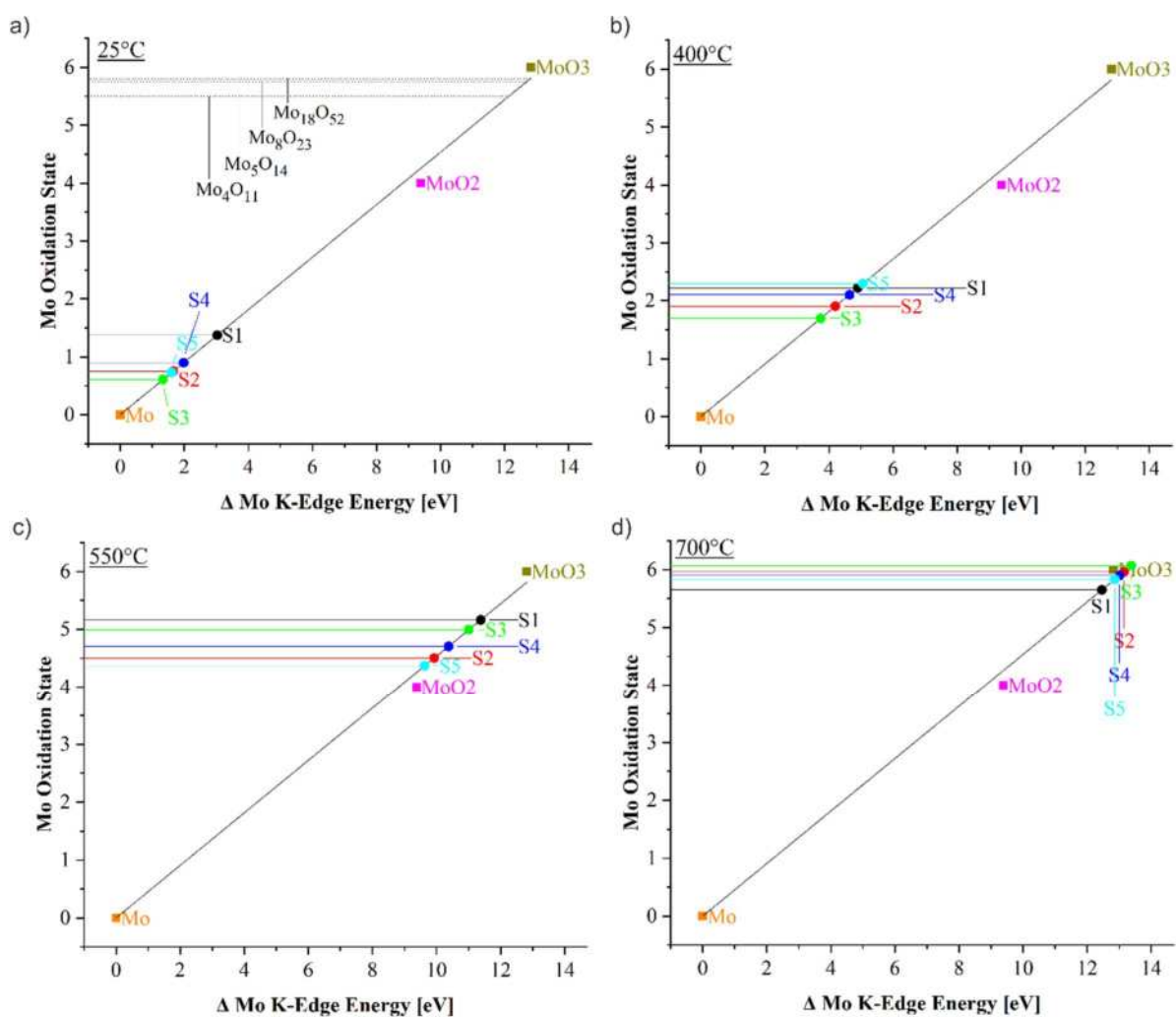
Fig. 3: Mo oxidation state of MoN$_x$ thin films at 25 °C, 400 °C, 550 °C, and 700 °C obtained from XANES using Mo, MoO$_2$, and MoO$_3$ references [23]
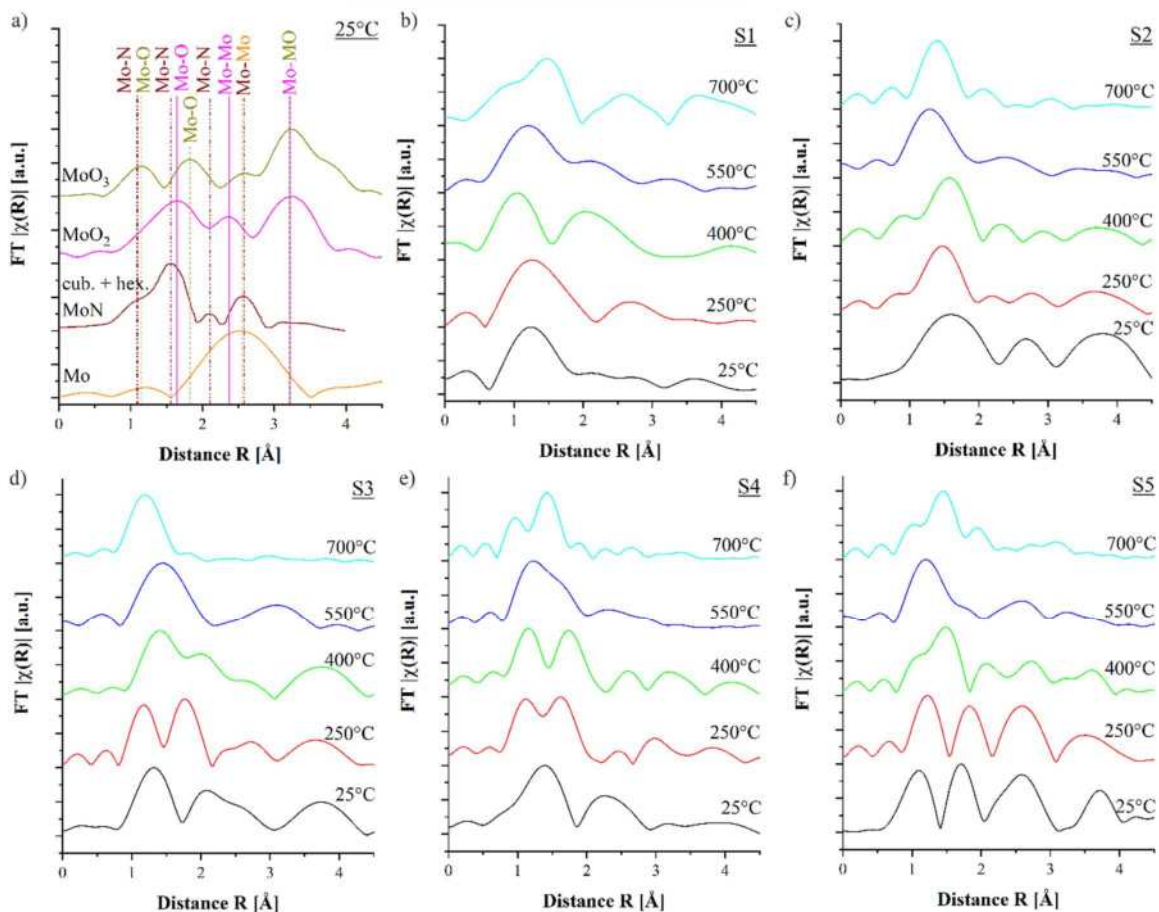
Fig. 4: Fourier transforms of the k^3-weighted EXAFS data of the in-situ experiments of the a) references and b)-f) MoN_x thin films in dependence of the temperature [23]

References

[1] U. Schleinkofer, C. Czettl, C. Michotte, 1.16 - Coating Applications for Cutting Tools, in: C.E. Nebel, D. Mari, L. LLanes, V.K. Sarin (Eds.), Comprehensive hard materials: Volume 1-3: Hardmetals, ceramics, super hard materials, Elsevier, Amsterdam, Waltham, Heidelberg, 2014, pp. 453–469.

[2] A.A. Voevodin, C. Muratore, S.M. Aouadi, Hard coatings with high temperature adaptive lubrication and contact thermal management: review, Surf Coat Technol 257 (2014) 247–265. https://doi.org/10.1016/j.surfcoat.2014.04.046.

[3] P.M. Martin, Handbook of deposition technologies for films and coatings: Science, applications and technology, 3rd ed. ed., William Andrew, 2009.

[4] D.G. Sangiovanni, V. Chirita, L. Hultman, Toughness enhancement in TiAlN-based quarternary alloys, Thin Solid Films 520 (2012) 4080–4088. https://doi.org/10.1016/j.tsf.2012.01.030.

[5] H. Kindlund, D.G. Sangiovanni, L. Martínez-de-Olcoz, J. Lu, J. Jensen, J. Birch, I. Petrov, J.E. Greene, V. Chirita, L. Hultman, Toughness enhancement in hard ceramic thin films by alloy design, APL Materials 1 (2013) 42104. https://doi.org/10.1063/1.4822440.

[6] K. Balasubramanian, L. Huang, D. Gall, Phase stability and mechanical properties of Mo1-xNx with $0 \leq x \leq 1$, J Appl Phys 122 (2017) 195101. https://doi.org/10.1063/1.4998686.

[7] F.F. Klimashin, N. Koutná, H. Euchner, D. Holec, P.H. Mayrhofer, The impact of nitrogen content and vacancies on structure and mechanical properties of Mo–N thin films, J Appl Phys 120 (2016) 185301. https://doi.org/10.1063/1.4966664.

[8] M. Altarawneh, Z. Jaf, H. Oskierski, Z.-T. Jiang, J. Gore, B.Z. Dlugogorski, Conversion of NO into N 2 over γ-Mo 2 N, J. Phys. Chem. C 120 (2016) 22270–22280. https://doi.org/10.1021/acs.jpcc.6b04107.

[9]   S.F. Zaman, N. Pasupulety, A.A. Al-Zahrani, M.A. Daous, S.S. Al-Shahrani, H. Driss, L.A. Petrov, K.J. Smith, Carbon monoxide hydrogenation on potassium promoted Mo 2 N catalysts, Appl Catal A 532 (2017) 133–145. https://doi.org/10.1016/j.apcata.2016.12.015.

[10]   V.P. Anitha, S. Vitta, S. Major, Structure and properties of reactivity sputtered γ-Mo2N hard coatings, Thin Solid Films 245 (1994) 1–3. https://doi.org/10.1016/0040-6090(94)90867-2.

[11]   J. Valli, U. Mäkelä, H.T.G. Hentzell, Tribological properties of MoN x coatings in contact with copper, J Vac Sci Technol A 4 (1986) 2850–2854. https://doi.org/10.1116/1.573689.

[12]   A. Gilewicz, B. Warcholinski, D. Murzynski, The properties of molybdenum nitride coatings obtained by cathodic arc evaporation, Surf Coat Technol 236 (2013) 149–158. https://doi.org/10.1016/j.surfcoat.2013.09.005.

[13]   V.P. Anitha, A. Bhattacharya, N.G. Patil, S. Major, Study of sputtered molybdenum nitride as a diffusion barrier, Thin Solid Films 236 (1993) 306–310. https://doi.org/10.1016/0040-6090(93)90687-K.

[14]   F. Fujimoto, Y. Nakane, M. Satou, F. Komori, K. Ogata, Y. Andoh, Formation of molybdenum nitride films by ion beam and vapor deposition method, Nucl Instrum Meth B 19-20 (1987) 791–796. https://doi.org/10.1016/S0168-583X(87)80159-3.

[15]   H. Luo, G. Zou, H. Wang, J.H. Lee, Y. Lin, H. Peng, Q. Lin, S. Deng, E. Bauer, T.M. McCleskey, A.K. Burrell, Q. Jia, Controlling Crystal Structure and Oxidation State in Molybdenum Nitrides through Epitaxial Stabilization, J Phys Chem C 115 (2011) 17880–17883. https://doi.org/10.1021/jp2048376.

[16]   V. Zin, E. Miorin, S.M. Deambrosis, F. Montagner, M. Fabrizio, Mechanical properties and tribological behaviour of Mo-N coatings deposited via high power impulse magnetron sputtering on temperature sensitive substrates, Tribol Int 119 (2018) 372–380. https://doi.org/10.1016/j.triboint.2017.11.007.

[17]   T. Suszko, W. Gulbiński, J. Jagielski, The role of surface oxidation in friction processes on molybdenum nitride thin films, Surf Coat Technol 194 (2005) 319–324. https://doi.org/10.1016/j.surfcoat.2004.07.119.

[18]   V.S. Sergevnin, I.V. Blinkov, A.O. Volkhonskii, D.S. Belov, D.V. Kuznetsov, M.V. Gorshenkov, E.A. Skryleva, Wear behaviour of wear-resistant adaptive nano-multilayered Ti-Al-Mo-N coatings, Appl Surf Sci 388 (2016) 13–23. https://doi.org/10.1016/j.apsusc.2016.06.102.

[19]   A. Magnéli, Structures of the ReO 3 -type with recurrent dislocations of atoms: `homologous series' of molybdenum and tungsten oxides, Acta Cryst 6 (1953) 495–500. https://doi.org/10.1107/S0365110X53001381.

[20]   J. Baltrusaitis, B. Mendoza-Sanchez, V. Fernandez, R. Veenstra, N. Dukstiene, A. Roberts, N. Fairley, Generalized molybdenum oxide surface chemical state XPS determination via informed amorphous sample model, Appl Surf Sci 326 (2015) 151–161. https://doi.org/10.1016/j.apsusc.2014.11.077.

[21]   C. Liu, H. Ju, L. Yu, J. Xu, Y. Geng, W. He, J. Jiao, Tribological Properties of Mo2N Films at Elevated Temperature, Coatings 9 (2019) 734. https://doi.org/10.3390/coatings9110734.

[22]   N. Solak, F. Ustel, M. Urgen, S. Aydin, A.F. Cakir, Oxidation behavior of molybdenum nitride coatings, Surf Coat Technol 174-175 (2003) 713–719. https://doi.org/10.1016/S0257-8972(03)00702-3.

[23]   W. Tillmann, D. Kokalj, D. Stangier, Impact of structure on mechanical properties and oxidation behavior of magnetron sputtered cubic and hexagonal MoNx thin films, Applied Surface Science Advances 5 (2021) 100119. https://doi.org/10.1016/j.apsadv.2021.100119.

ReflEXAFS investigation of in-situ sputtered CoN thin films

F. Braun, D. Lützenkirchen-Hecht, R.Wagner

Fakultät 4 - Mathematik und Naturwissenschaften, Bergische Universität Wuppertal, Gaußstraße 20, 42119 Wuppertal

Recent studies have shown that Cobalt mononitride (CoN) can be useful in several applications. Examples are high capacity anodes in Li-ion batteries [1, 2], non-aquenous supercapacitors [3] and inexpensive catalysts for oxygen and hydrogen evolution reactions which are needed for electrocatalysis and water splitting [4–9]. Furthermore CoN can be used for mesoscopic and perovskite solar cells [10]. Research to deepen the structural and magnetic understanding of CoN and other major Co-N phases do already exist [11–13]. This experiment tests the in-situ sample preparation and analysis of CoN thin films. The samples were prepared in a miniaturized DC-sputtering chamber which was integrated into the Beamline 10 as shown in figure 1.

Figure 1: *Integration of the DC-sputtering chamber into the Beamline 10.*

Several samples were sputtered for one hour with $5\,\mathrm{mA}$ or $10\,\mathrm{mA}$ sputtering current under pressures ranging from $0.18\,\mathrm{mbar}$ to $0.22\,\mathrm{mbar}$ in a 100% nitrogen atmosphere. Studies show that CoN is only stable up to a temperature of $150\,°\mathrm{C}$ [11]. However these temperatures where never reached in this experiment. Sample temperatures peak at $55\,°\mathrm{C}$ for sputtering with a current of $5\,\mathrm{mA}$ and at $81\,°\mathrm{C}$ for $10\,\mathrm{mA}$ as measured with a PT100 thermometer at the sample surfaces. For each sample ReflEXAFS at different incident angles around the critical angle of total reflection were measured with an acquisition time of $\approx 40\,\mathrm{min}$.

Figure 2 shows a fitted exemplary data file. The sample was sputtered with $10\,\mathrm{mA}$ for one hour under $0.19\,\mathrm{mbar}$ pure nitrogen atmosphere. The calculation fitted to the experimental data employed the dispersion and absorption coefficient of a CoN reference measurement which originates from a previous study of CoN [12]. The reference resembles the zinc-blende (ZB) type structure of CoN which has a pre-edge feature unlike the rock-salt (RS) type structure. Geometrical corrections were made to compensate the relatively large vertical slit of $0.1\,\mathrm{mm}$ in front of the sample.

As can be seen, the fit is able to model the experimental data over the entire energy range, and thus, the fits verifies that we sputtered CoN in ZB-type structure which is consistent through different incident angles of the beam.
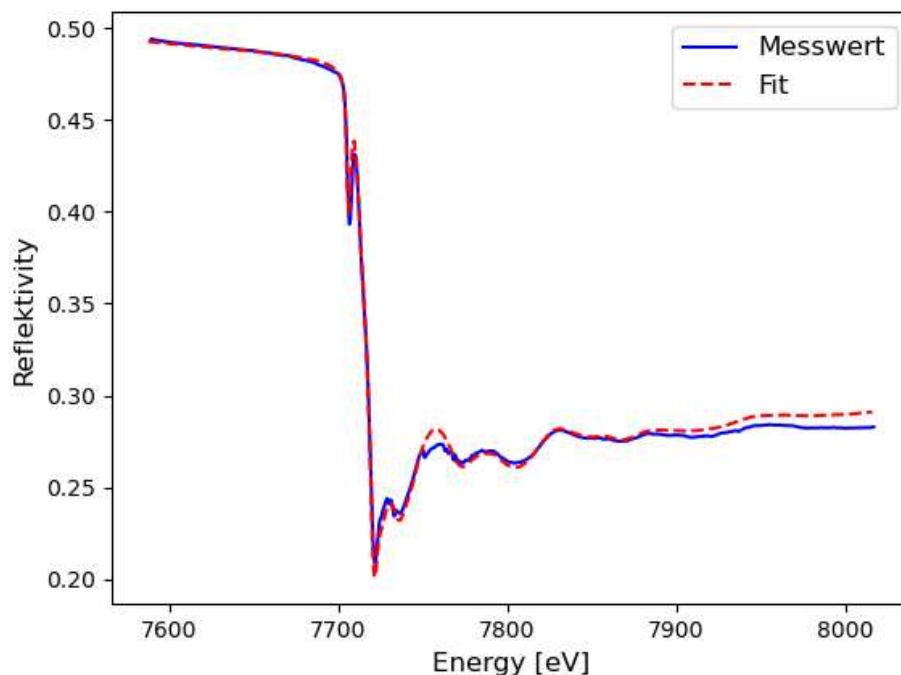
Figure 2: *Fitted in-situ ReflEXAFS at 0.20° of a 30 nm thick CoN thin film with 5.3 nm surface roughness. The sample was sputtered with 10 mA under 0,19 mbar for 60 min.*

References

[1] B.Das, M.V. Reddy, G.V.S: Rao, B.V.R Chowdari: *Synthesis of porous-CoN nanoparticles and their application as a high capacity anode for lithium–ion batteries*, J. Mater. Chem., 2012, 22, 17505, https://doi.org/10.1039/C2JM31969A.

[2] B.Das, M.V.Reddy, B.V.R.Chowdari: *X-ray absorption spectroscopy and energy storage of Ni-doped cobalt nitride, (*$Ni_{0\ 33}Co_{0\ 67}$*)N, prepared by a simple synthesis route*, Nanoscale, 2013, 5, 1961, https://doi.org/10.1039/c2nr33675h.

[3] B.Das, M.Behm, G.Lindbergh, M.V.Reddy, B.V.R.Chowdari: *High performance metal nitrides, MN (M = Cr, Co) nanoparticles for nonaqueous hybrid supercapacitors*, Advanced Powder Technology (2015), http://dx.doi.org/10.1016/j.apt.2015.02.001.

[4] Yueqing Wang, Baohua Zhang, Wei Pan, Houyi Ma, Jintao Zhang: *3D Porous Nickel–Cobalt Nitrides Supported on Nickel Foam as Efficient Electrocatalysts for Overall Water Splitting*, ChemSusChem 2017, 10, 4170 − 4177, https://doi.org/10.1002/cssc.201701456.

[5] Yongqi Zhang, Bo Ouyang, Jing Xu, Guichong Jia, Shi Chen, Rajdeep Singh Rawat, Hong Jin Fan: *Rapid Synthesis of Cobalt Nitride Nanowires: Highly Efficient and Low-Cost Catalysts for Oxygen Evolution*, Angew. Chem. Int. Ed. 2016, 55, 1 − 6, http://dx.doi.org/10.1002/anie.201604372.

[6] Xiang Peng, Chaoran Pi, Xuming Zhang, Shuai Li, Kaifu Huo, Paul K. Chu: *Recent progress of transition metal nitrides for efficient electrocatalytic water splitting*, Sustain Energy Fuels 3:366–381, DOI: 10.1039/c8se00525g.

[7] Zhijie Chen, Xiaoguang Duan, Wei Wei, Shaobin Wang, Bing-Jie Ni:*Recent advances in transition metal-based electrocatalysts for alkaline hydrogen evolution*, J. Mater. Chem. A, 2019, 7, 14971, https://doi.org/10.1039/C9TA03220G.

[8] Z.Chen, X.Duan, W.Wei, S.Wang, B.J.Ni:*Recent advances in transition metal-based electrocatalysts for alkaline hydrogen evolution* J Mater Chem A 7:14971–15005, 2019, https://doi. org/10.1039/C9TA03220G.

[9] Z.Wu, D.Nie, M.Song, T.Jiao, G.Fu, X.Liu: *Facile synthesis of Co–Fe–B-P nanochains as an efcient bifunctional electrocatalyst for overall water-splitting*, Nanoscale 11:7506–7512, 2019, https://doi.org/10.1039/C9NR01794A.

[10] J.S.Kang, J.Y.Kim, J.Yoon, et al.: *Room-temperature vapor deposition of cobalt nitride nanoflms for mesoscopic and perovskite solar cells*, Adv Energy Mater 8:1703114, 2018, https://doi.org/10.1002/aenm.201703114.

[11] R. Gupta, N. Pandey, A. Tayal, M. Gupta: *Phase formation, thermal stability and magnetic moment of cobalt nitride thin films*, AIP Advances 5, 097131, 2015.

[12] N. Pandey, M. Gupta, R. Gupta, S. Chakravarty, N. Shukla, A. Devishvili: *Structural and magnetic properties of Co-N thin films deposited using magnetron sputtering at 523 K*, Journal of Alloys and Compounds 694, S. 1209-1213, 2017.

[13] M. Gupta, Y. Kumar, A. Tayal, N. Pandey, W. Caliebe, J. Stahn: *X-ray absorption spectroscopy study of cobalt mononitride thin films*, SN Applied Sciences 2:41, 2020.

EXAFS investigations of atomically dispersed Co/N-doped porous carbon networks

K. Yuan[a], B. Huang[a], L. Li[a], X. Tang[a], X. Zhuang[b], Y. Chen[a,c],
F. Braun[d], F. Eckelt[d], L. Voss[d], D. Lützenkirchen-Hecht[d]

[a]*College of Chemistry/Institute of Polymers, Nanchang University, 999 Xuefu Avenue, Nanchang 330031, China.*
[b]*School of Chemistry and Chemical Engineering, Shanghai Jiao Tong University, Dongchuan Road 800, 200240 Shanghai, China*
[c]*Institute of Advanced Scientific Research (iASR), Key Laboratory of Functional Small Molecules for Ministry of Education, Jiangxi Normal University, 99 Ziyang Avenue, Nanchang 330022, China*
[d]*Faculty of Mathematics and Natural Sciences-Physics Department, Bergische Universität Wuppertal, Gauss-Str. 20, D-42119 Wuppertal, Germany*

Catalysts, in particular electrocatalysts based on noble metals such as gold, platinum and their alloys exhibit a prominent activity for the oxygen reduction reaction (ORR). Due to the extreme costs of the noble metals, however, cheap, eco-friendly and earth-abundant surrogates are needed for practical applications on large scales. In this context, both transition metal- as well as carbon-based materials have gained increasing interested in the past years (see, e.g. [1-5]). In particular nitrogen-doped graphene and carbon nanotubes have shown to be an efficient, low-cost alternative to Pt for the ORR [6, 7], and co-doping those materials with a second heteroatom such as boron, phosphorus or sulphur can further boost the ORR activity [8, 9]. An additional improvement of the ORR-performance results by the addition of Fe or Co into the nitrogen doped carbon materials, which may form highly catalytic metal-N-C sites [10, 11]. While we have considered iron insertion into nitrogen and boron doped carbon catalysts previously [12, 13], we want to elucidate the structures of cobalt-doped carbon materials here.

For the synthesis of HBY-1, we firstly chelated tetrakis(4-aminophenyl) porphyrin with Co to obtain cobalt tetrakis(4-aminophenyl) porphyrin compound. Then, the as-prepared cobalt porphyrin compound was anchored on pyridine-functionalized graphene through Co-N coordination effect. Finally, the adjacent cobalt porphyrin compounds were linked with each other by amino groups through azo-coupling reaction to obtain cobalt porphyrin-based polymer with axial coordination. For the synthesis of HBY-2, similarly, tetrakis(4-aminophenyl) porphyrin was primarily chelated with Co to obtain cobalt tetrakis(4-aminophenyl) porphyrin compound. However, the as-prepared cobalt porphyrin compound was directly combined with pristine graphene through π-π stacking. Finally, also by connecting adjacent amino groups through azo-coupling reaction, the cobalt porphyrin-based polymer without axial coordination was prepared. The samples typically contained a total trace amount of cobalt of about 0.3 at. %.

X-ray absorption spectroscopy (XAS) experiments were carried out at the wiggler beamline BL10 at the DELTA storage ring (Dortmund, Germany) operated with 80-130 mA of 1.5 GeV electrons [14]. Co K-edge spectra were collected using a Si(111)-channel cut monochromator and gas-filled ionization chambers as detectors for the incoming and the transmitted intensities, and a large area photodiode for the fluorescence photons. The powder samples were filled in 3 mm thick frames with Kapton windows on both sides without any additional treatment. Due to the low concentration of the absorbing Co, a typical edge jump of about 0.03 to 0.05 results. For comparison, a Co-metal foil as well as several Co-reference compounds such as Co_2O_3, CoO, Co_3O_4 and Cobalt mononitride (CoN) were measured.

In Fig. 1, the magnitude of the Fourier-transforms of both Co-containing samples are shown together with a first-shell fit assuming the presence of a Co-N nearest neighbor coordination. As can be seen, the intensity of the first shell is substantially enhanced for sample HBY-1, with an amplitude close to 1.5, in comparison to HBY-2, with an amplitude of about 1.2 only, suggesting a larger number of nearest nitrogen neighbors. Both samples do not display any distinct coordination shells at larger radial distances, in particular in comparison to crystalline Co-mononitride (see, e.g. [15]). The quantitative fits suggest a square planar coordination with four nitrogen in a distance of $R_1 = 1.94 \pm 0.02$ Å and a mean disorder of $\sigma_1^2 = 0.0031 \pm 0.0029$ Å^2 for sample HBY-2. In contrast, for HBY-1, $R_1 = 1.95 \pm 0.03$ Å and a mean disorder of $\sigma_1^2 = 0.0052 \pm 0.0039$ Å^2 resulted, however with five nearest neighbors. Taking into account that the disorder parameter and the coordination number are strongly correlated in the fit, one may argue that the fit results are not meaningful. However, taking into account that the structural disorder is generally larger for a three-dimensional arrangement of the atoms

within the investigated cluster, with a shorter in-plane and a more extended out-of-plane bond length, the calculated difference in the coordination number appear meaningful, suggesting a local environment as depicted in the structural motives accompanying the figures.
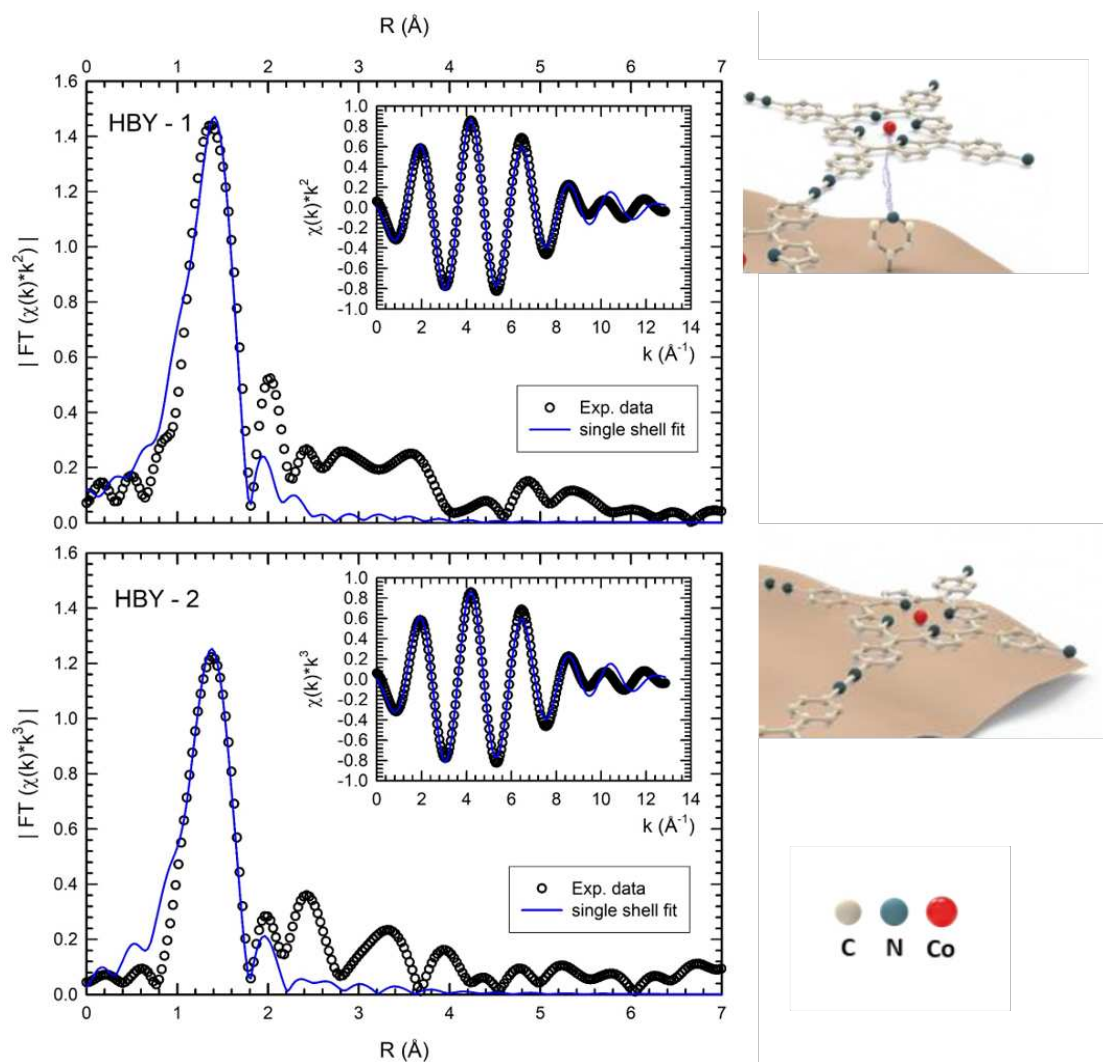

Fig. 1: Magnitude of the Fourier transforms of the k^2-weighted EXAFS fine structure oscillations $|FT (\chi(k)*k^2)|$ measured above the Co K-edge of samples HBY-1 and HBY-2. The range of the first coordination was extracted by means of a filter function, back-transformed into k-space, and fitted with a single Co-N shell for both samples, as depicted in the inserts. The proposed structural motives are sketched to the respective figures.

Acknowledgement

References

[1] X. Liu, L. Dai, Nat. Rev. Mater. 1 (2016) 16064.
[2] Y. Zhao, J. Wan, H. Yao, et al., Nat. Chem. 10 (2018) 924.
[3] L. Yang, J. Shui, L. Du, et al., Adv. Mater. 31 (2019) 1804799.
[4] J. Zhang, Z. Zhao, Z. Xia, et al., Nat. Nanotechnol. 10 (2015) 444.
[5] K. Yuan, C. Lu, S. Sfaelou, et al., Nano Energy 59 (2019) 207.
[6] Y. Li, W. Zhou, H. Wang, et al., Nat. Nano 7 (2012) 394.
[7] H. Cui, Z. Zhou, D. Jia, Mater. Horiz. 4 (2017) 7.
[8] Y. Meng, D. Voiry, A. Goswami, et al., J. Am. Chem. Soc. 136 (2014) 13554.
[9] Z.X. Pei, H.F. Li, Y. Huang, et al., Energy Environ. Sci. 10 (2017) 742.
[10] A. Zitolo, V. Goellner, V. Armel, et al., Nature Mater. 14 (2015) 937.
[11] U.I. Kramm, I. Herrmann-Geppert, J. Behrends, et al., J. Am. Chem. Soc. 138 (2016) 635.
[12] K. Yuan, S. Sfaelou, M. Qiu, et al., ACS Energy Lett. 3 (2018) 252.
[13] K. Yuan, D. Lützenkirchen-Hecht, L. Li, et al., J. Am. Chem. Soc. 142 (2020) 2404.
[14] D. Lützenkirchen-Hecht, R. Wagner, S. Szillat, et al., J. Synchrotron Rad. 21 (2014) 819.
[15] M. Gupta, Y. Kumar, A. Tayal, et al., SN Applied Sciences 2 (2020) 41.

EXAFS investigations of ZnO nanoparticles at liquid nitrogen temperature

A. Šarić[a], F. Eckelt[b], M. Vrankić[a], R. Wagner[b], D. Lützenkirchen-Hecht[b],

a) Division of Materials Physics, Centre of Excellence for Advanced Materials and Sensing Devices, Ruđer Bošković Institute,Bijenička 54, 10000 Zagreb, Croatia.

b) Bergische Universität Wuppertal – Fakultät für Mathematik und Naturwissenschaften, Gauß-Str. 20, 42097 Wuppertal, Germany.

Zinc oxide (ZnO) crystallizes in the hexagonal (wurtzite) space group No. 186 (P63mc) with unit cell metrics $a = b = 3.289$ Å, $c = 5.307$ Å and $\alpha = \beta = 90°$, and $\gamma = 120°$ at room temperature (RT), respectively [1]. Previous experiments have shown, that ZnO nanoparticles prepared by hydrolysis of zinc acetylacetonate monohydrate ($Zn(acac)_2 \cdot H_2O$) also reveal such a structure, however with subtle differences of the unit cell parameters depending on the details of the preparation, such as additives, reaction time, temperature and pH of the solutions, etc. [2-5]. Here we want to investigate the structure of zinc oxide nanoparticles prepared by the hydrolysis of zinc acetylacetonate monohydrate in the presence of trisodium citrate as additive [2]. Zn K-edge EXAFS experiments were performed at DELTA beamline 10 [6], making use of the (111) channel-cut monochromator, and gas-filled ionization chambers as detectors. In order to enhance the significance of the experiments and the data evaluation, the samples were cooled down to liquid nitrogen temperatures employing a bath cryostat to reduce thermal disorder substantially and thereby enhance the amplitudes of the EXAFS fine structure oscillations $\chi(k)$, in particular at large photoelectron wave numbers (k). The effect of this procedure can clearly be seen in Fig. 1(a), where the magnitude of the Fourier-transforms of the k^3-weighted EXAFS fine structures $\chi(k)*k^3$ are displayed for both, a RT measurement (300 K) as well as for the same sample cooled to liquid nitrogen temperature (77 K).
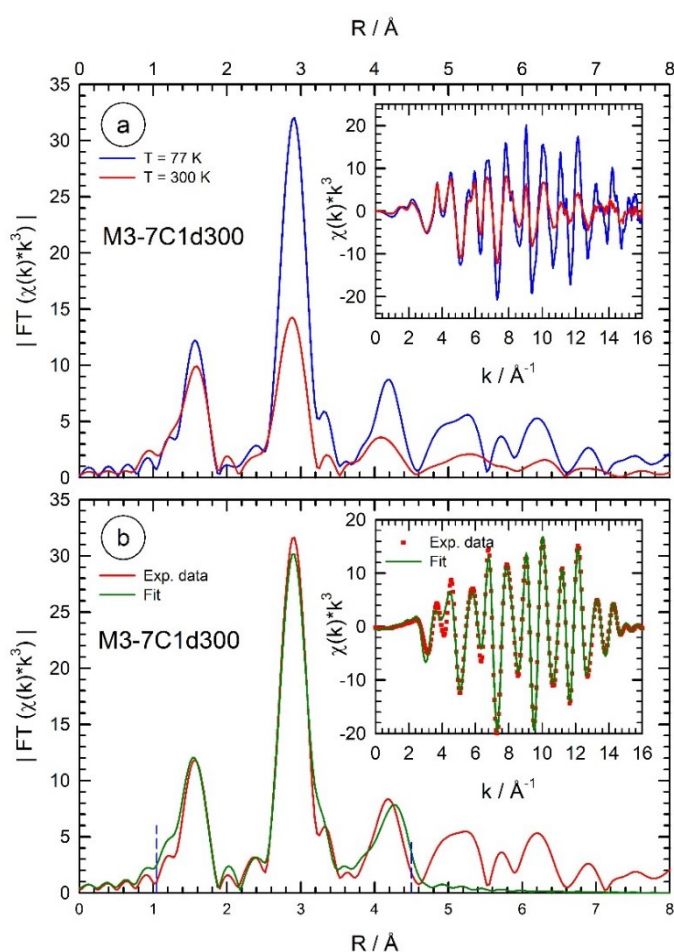

Figure 1: (a) Comparison of the magnitudes of the Fourier-transforms of the k^3-weighted EXAFS fine structure oscillations $\chi(k)*k^3$ for a ZnO nanoparticle sample (M3-7C1d300) at RT (——) and 77 k (——). In the insert, $\chi(k)*k^3$ is displayed for both temperatures. (b) EXAFS fit of the ZnO nanoparticle sample in R- and k-space. The k-range from $k_{min} = 2.540$ Å^{-1} to $k_{max} = 14.581$ Å^{-1} was used for the Fourier-transform, and the R-range from $R_{min} = 1.05$ Å to $R_{max} = 4.5$ Å (vertical dashed lines) was optimized in the fitting procedure. All atoms up to a radius of 4.7 Å in real space were considered for the fit here, resulting in 14 different single and multiple scattering paths in a cluster of 39 atoms in total.

Each of the coordination shells (i) within the considered cluster with a radius of 4.7 Å is characterized by its distance R_i, the number of atoms in this selected shell (N_i), the mean square displacement (σ_i^2), an amplitude reduction factor ($S_{0,i}^2$) and an inner potential shift (ΔE_{0i}). If all shells would be treated individually, a huge number of fit parameters would be generated, i.e., here at least 56. Thus, any fit using such a set of variables would be statistically insignificant, as a limit for the used number of fit variables (N_{idp}) can be estimated from the energy range covered by the experiment and the R-range in the FT [7]. For the modelling we have used a rather simple model employing only seven variables: A global expansion parameter α, so that all the fitted distances are $R_{eff}*\alpha$, R_{eff} being the distance calculated from the original crystal structure. In order to include different oscillation amplitudes, we have used identical values for σ_O^2 for all Zn-O coordinations, and σ_{Zn}^2 for all Zn-Zn bonds, respectively. For multiple scattering pathways, averaged values of all involved atoms were used. A unique amplitude reduction factor, $S_{0,i}^2$, and inner potential shift (ΔE_{0i}) were used for all shells, here $\Delta E_0 = 2.68 \pm 0.85$ eV. In order to detect small changes of the first Zn-O and second Zn-Zn neighbor bonds more sensitively, we have introduced individual variables for both paths R_1 and R_2. Such a rather simple structural model imparts a substantial statistical significance of the fits, as N_{idp} amounts to values of 25 and more, compared to only 7 used parameters here. A typical fit is shown in Fig. 1(b), with an $\mathcal{R}$ - factor of 0.025, thereby proving the opportunity to model the data successfully with a high precision. In particular, R_1 and R_2 were determined with an uncertainty of well below 0.01 Å, and values of 1.960 Å and 3.227 Å, respectively. The σ_O^2 and σ_{Zn}^2 were determined to 4.16×10^{-3} Å$^2 \pm 0.89 \times 10^{-3}$ Å^2 and 5.05×10^{-3} Å$^2 \pm 0.45 \times 10^{-3}$ Å^2. The value of the lattice expansion factor is -0.0180 with respect to the crystallographic values at RT that are stored in the materials project data base [1]. Ongoing work is dedicated to the systematic fitting of EXAFS data obtained at liquid nitrogen temperature from differently prepared ZnO nanomaterials and a correlation of the derived structural details to physico-chemical properties, in particular on the photocatalytic efficiency of the ZnO particles which was monitored using degradation over organic dyes pollutant solution.

References:

[1] https://materialsproject.org/materials/mp-2133/
[2] A. Šarić, S. Musić, M. Ivanda , J. Mol. Struct. 993 (2011) 219.
[3] A. Šarić, I. Despotović,G. Štefanić, J. Phys. Chem. C 123 (2019) 29393.
[4] A. Šarić, F. Eckelt, M. Vrankić, et al., DELTA annual report (2020) 105.
[5] A. Šarić, M. Vrankić, D. Lützenkirchen-Hecht, et al., J. Alloys Compounds (2021), in preparation.
[6] D. Lützenkirchen-Hecht, R. Wagner, S. Szillat, et al., J. Synchrotron Rad. 21 (2014) 819.
[7] E.A. Stern, Phys. Rev. B 48 (1993) 9825.

Notes

Notes